USING CLUMPED ISOTOPES AND RADIOCARBON TO CHARACTERIZE RAPID CLIMATE CHANGE DURING THE LAST GLACIAL CYCLE

Thesis by

Nivedita Thiagarajan

In Partial Fulfillment of the Requirements for the degree

of

Doctor of Philosophy

CALIFORNIA INSTITUTE OF TECHNOLOGY

Pasadena, California

2012

(Defended May 18, 2012)

ACKNOWLEDGEMENTS

This thesis is the result of the guidance of my two advisors, Jess Adkins and John Eiler. Their insights and knowledge have always been inspiring for me and they have patiently taught me how to become a scientist.

My scientific discovery was greatly helped by many individuals. John Anderson and Cin-ty Lee at Rice University got me interested in Geology. Aradhna Tripati, Nele Meckler, and Sarah Feakins all guided me at key points early at the start of my graduate career. Ben Passey greatly improved my life (and data) quality by automating the process of making clumped isotope measurements.

I would like to thank the members of NOSAMS at WHOI for teaching me how to make radiocarbon measurements. They are a friendly group and I'll fondly remember my time there.

I also would like to thank Nathan Dalleska for patiently helping me isolate hydroxyproline from La brea bones. I could always count on him for support, advice, and good humor.

I'd like to thank the past and present members of the Adkins and Eiler lab for helpful conversations. Alex Gagnon, Weifu Guo, Madeline Miller, Seth Finnegan, Andrea Burke, and James Rae helped me several times dig myself out of whatever deep scientific hole, I'd managed to put myself into. (I'd still be digging it, if it weren't for y'all). I'd also like to acknowledge Daniel Stolper. His enthusiasm for science is infectious and I have enjoyed being contaminated. I'm also grateful to Nami Kitchen for helping me in fiery situations.

Life would not have been the same at Caltech without the good friends I met there. Anne, Anna and I have spent many enjoyable days (without mentioning evenings or nights) at Caltech and away. I'm lucky to have met you. Adam, Guillaume and Katie, y'all have made the time I spent in lab fun.

I'd like to thank Rick Ueda, my photography teacher at the Art Center. I was lucky to take advantage of the photography classes offered at the Art Center, and Rick's kind words helped me at stressful times at work.

I'd like to thank Michael Long for keeping me supplied with fresh eggs, dinners and good spirits when I needed them.

I'd also like to thank my family for always helping me keep my perspective on life.

In memory of Sacrebleu, Le Poisson, and Arraintxu.

ABSTRACT

We generated records of carbonate clumped isotopes and radiocarbon in deep-sea corals to investigate the role of the deep ocean during rapid climate change events. First we calibrated the carbonate clumped isotope thermometer in modern deep-sea corals. We examined 11 specimens of three species of deep-sea corals and one species of a surface coral spanning a total range in growth temperature of 2–25°C. We find that skeletal carbonate from deep-sea corals shows the same relationship of Δ_{47} to temperature as does inorganic calcite. We explore several reasons why the clumped isotope compositions of deep-sea coral skeletons exhibit no evidence of a vital effect despite having large conventional isotopic vital effects.

We also used a new dating technique, called the reconnaissance dating method to investigate the ecological response of deep-sea coral communities in the North Atlantic and Southern Ocean to both glaciation and rapid climate change. We find that the deep-sea coral populations of *D. dianthus* in both the North Atlantic and the Southern Ocean expand at times of rapid climate change. The most important factors for controlling deep-sea coral distributions are likely climatically driven changes in productivity, $[O_2]$ and $[CO_3^{2-}]$.

We take 14 deep-sea corals that we had dated to the Younger Dryas (YD) and Heinrich 1 (H1), two rapid climate change events during the last deglaciation and make U-series dates and measure clumped isotopes in them. We find that temperatures during the YD and H1 are cooler than modern and that H1 exhibits warming with depth. We place our record in the context of atmospheric and marine benthic $\Delta^{14}C$, $\delta^{13}C$, and $\delta^{18}O$ records during the deglaciation to understand the role of the deep North Atlantic during the deglaciation.

We also investigated the role of climate change in the distribution of terrestrial megafauna. To help with this, we also developed a method for compound-specific radiocarbon dating of hydroxyproline extracted from bones in the La Brea Tar Pits. We find that the radiocarbon chronologies of megafauna from several locations around the world, including the La Brea Tar Pits, exhibit an increase in abundance of megafauna during Heinrich events

TABLE OF CONTENTS

List of Figures:

List of Tables

Chapter 1

Introduction

The ocean is considered a key parameter during glacial-interglacial transitions and rapid climate change events, as it is one of the largest reservoirs of CO_2 and heat in the atmosphere-climate system. The most common and successful approach to reconstructing past ocean conditions take advantage of isotopic and elemental substitution into foraminiferal $CaCO_3$ in sediment cores to determine a variety of parameters, including temperature, nutrient ratios, and carbon systematics. Here we develop the use of deep-sea corals as a paleoclimate archive.

Deep-sea corals are a relatively new archive in paleoceanography. Their banded skeletons can be used to generate 100 year high-resolution records without bioturbation. They also have a high concentration of uranium, allowing for accurate independent calendar ages using U–Th systematics. These characteristics make them particularly suited for studying the deep ocean, especially on timescales relevant to rapid climate change. In this work we are interested in understanding the capacity of the ocean to influence rapid climate change. We approach this issue by monitoring and developing new tools to determine deep ocean chemistry recorded in the deep-sea corals.

In Chapter 2 , we calibrate the carbonate clumped isotope thermometer in modern deep-sea corals. We examined 11 specimens of three species of deep-sea corals and one species of a surface coral spanning a total range in growth temperature of 2–25°C. Internal standard errors for individual measurements ranged from 0.005‰ to 0.011‰ (average: 0.0074‰) which corresponds to 1–2°C. External standard errors for replicate measurements of Δ_{47} in corals ranged from 0.002‰ to 0.014‰ (average: 0.0072‰) which corresponds to 0.4–2.8°C. This result indicates that deep sea corals can be used for paleothermometry, with precisions as good as 0.4°C. We also observe no vital effects in Δ_{47} for samples that display large vital effects in $\delta^{18}O$ and $\delta^{13}C$. We explore several reasons for why the clumped isotope

composition of deep-sea corals exhibit no evidence of a vital effect and conclude that pH effects could explain the observed variations in Δ_{47} and $\delta^{18}O$.

In chapter 3, we use a new dating technique, called the reconnaissance dating method to investigate the ecological response of deep-sea coral communities in the North Atlantic and Southern Ocean to both glaciation and rapid climate change. We find that the deep-sea coral populations of *D. dianthus* in both the North Atlantic and the Southern Ocean expand at times of rapid climate change. However, during the more stable Last Glacial Maximum the coral population globally retreats to a more restricted depth range. Holocene populations show regional patterns that provide some insight into what causes these dramatic changes in population structure. The most important factors are likely responses to climatically driven changes in productivity, $[O_2]$ and $[CO_3^{2-}]$.

In chapter 4, we take advantage of the results of the previous two chapters. We analyze 14 deep-sea corals that we had dated to the Younger Dryas (YD) and Heinrich 1 (H1), using the reconnaissance dating technique and make high-precision radiocarbon dates, U-series dates and clumped isotope measurements. We find that temperatures during the YD and H1 are cooler than modern and that H1 exhibits warming with depth. This warming at depth supports the "Thermobaric Capacitor" hypothesis for causing deep ocean mixing. We place our record in the context of atmospheric and marine benthic $\Delta^{14}C$, $\delta^{13}C$ and $\delta^{18}O$ records during the deglaciation to understand the role of the deep North Atlantic during the deglaciation.

In chapter 5, we investigate the effects of rapid climate change on the terrestrial biosphere, particularly the distribution of terrestrial megafauna. Current hypotheses for the extinction of megafauna focus on human interactions or environmental change. Most of the climate change hypotheses emphasize either changes in habitat or the fast rate of climate change. To further explore the relationship of megafauna to rapid climate change, we examine the abundance of megafauna in the La Brea Tar Pits during the YD and H1.

The La Brea Tar Pits are an exceptionally well preserved archive that has trapped

over three million fossil skeletons including 3400 large mammals. The deposits are a series of open asphalt seeps that have acted as animal traps for at least the past 50,000 years. Previous studies have been limited by weak chronological control, as stratigraphic position is known to be an unreliable indicator of relative age within the asphalt deposits and the asphalt itself has been a large source of carbon contamination. To help with this, we have developed an HPLC method for compound-specific radiocarbon dating of hydroxyproline extracted from bones in the La Brea Tar Pits. We find that in La Brea and other locations around the world, the megafauna abundance actually increases. Therefore megafauna extinctions were either primarily caused by humans, a climatic variable that did not adversely affect megafauna during rapid climate change events, or some combination of the two.

Chapter 2

Carbonate Clumped Isotope Thermometry of Deep-Sea Corals and Implications for Vital Effects

2.1 ABSTRACT

We examined 11 specimens of three species of deep-sea corals and one species of a surface coral spanning a total range in growth temperature of 2–25°C. Analytical precision for individual measurements ranged from 0.005 to 0.011‰ (average: 0.0074‰) which corresponds to ~ 1 to 2°C. Analytical precision for replicate measurements of Δ_{47} in corals ranged from 0.002 to 0.014‰ (average: 0.0072‰) which corresponds to 0.4 to 2.8°C. We find that skeletal carbonate from deep-sea corals shows the same relationship of Δ_{47} (the measure of ^{13}C-^{18}O ordering) to temperature as does inorganic calcite. In contrast, the $\delta^{18}O$ values of these carbonates (measured simultaneously with Δ_{47} for every sample) differ markedly from equilibrium with seawater; i.e., these samples exhibit pronounced 'vital effects' in their bulk isotopic compositions. We explore several reasons why the clumped isotope compositions of deep-sea coral skeletons exhibit no evidence of a vital effect despite having large conventional isotopic vital effects.

2.2 INTRODUCTION

Oxygen isotope measurements of biogenic marine carbonates are a long established and important tool for determining past ocean temperatures (Epstein et al., 1953; McCrea, 1950; Urey, 1947). In the decades following its initial development, the $\delta^{18}O$ thermometer was applied to planktonic foraminifera to reconstruct ocean temperature shifts on glacial/interglacial time scales (Emiliani, 1955). However it was later recognized that the planktonic record reconstructed from foraminifera $\delta^{18}O$ reflects a combination of the temperature from which the carbonate grew, and global changes in ice volume (Shackleton, 1967).

Deconvolving these two effects on the marine-carbonate oxygen isotope record remains a central problem in paleoclimatology. Chappell and Shackleton (1986) addressed this problem by examining dated coral terraces and benthic $\delta^{18}O$ records. Previously, the benthic $\delta^{18}O$ records had been interpreted assuming a constant temperature in the abyssal ocean. However, the resulting ice volume estimates derived from benthic $\delta^{18}O$ records could not be reconciled with ice volume records derived from the altitudes of dated coral terraces. Chappell and Shackleton (1986) made a detailed comparison of a coral terrace record in the Huon Peninsula with a benthic $\delta^{18}O$ record from the Pacific Ocean and concluded that during the last interglaciation, abyssal temperatures changed only during the transition from Marine Isotope Stage (MIS) 5e to 5d, and during the last glacial termination.

Subsequent efforts have reconstructed the $\delta^{18}O$ of the water of the deep ocean during the Last Glacial Maximum based on isotopic analyses of marine pore fluids (Schrag and DePaolo, 1993). Cutler et al. (2003) reconstructed a sea level curve based on fossilized surface corals from the Huon Peninsula and Barbados and combined this new sea level curve with the $\delta^{18}O$ of the water of the deep ocean reconstruction determined from pore fluids (Adkins et al., 2002). This work established that deep-sea temperatures have warmed by 4^{o}C in the Atlantic and 2^{o}C in the Pacific since the Last Glacial Maximum. In all of these studies, independent estimates of the change in sea level or of the $\delta^{18}O$ of the water of the deep ocean were necessary to extract deep ocean temperatures from benthic $\delta^{18}O$ data.

Carbonate clumped isotope thermometry is a new temperature proxy based on the ordering of ^{13}C and ^{18}O atoms into bonds with each other in the same carbonate molecule. The proportion of ^{13}C and ^{18}O atoms that form bonds with each other in a carbonate mineral has an inverse relationship with growth temperature. This isotopic ‘clumping’ phenomenon exists due to a

thermodynamically controlled homogeneous isotope exchange equilibrium in the carbonate mineral (or, perhaps, in the dissolved carbonate-ion population from which the mineral grows). This exchange reaction is independent of the $\delta^{18}O$ of water and $\delta^{13}C$ of DIC from which the carbonate grew; therefore it can be applied to settings where these quantities are not known (Eiler et al., 2003; Eiler and Schauble, 2004; Ghosh et al., 2006).

Here we calibrate carbonate clumped isotope thermometry in modern deep-sea corals. Deep-sea corals are a relatively new archive in paleoceanography. Their banded skeletons can be used to generate ~ 100-year high-resolution records without bioturbation. They also have a high concentration of uranium, allowing for accurate independent calendar ages using U-Th systematics. A thermometer in deep-sea corals could address the phasing of the offset between Northern and Southern Hemisphere in rapid climate events. The Greenland and Antarctic ice cores both show that temperature and CO_2 are tightly coupled over the last several glacial interglacial events. However, the synchronization of the ice cores from the two regions using atmospheric methane concentration trapped in the ice layers revealed that Antarctica warms several thousand years before the abrupt warmings in the Northern Hemisphere (Blunier and Brook, 2001). The deep ocean is a massive heat and carbon reservoir with an appropriate time constant that could be used to explain the several thousand year offset between the hemispheres. A temperature record of the deep ocean that spans the time period of these rapid climate events would help explain the role of the deep ocean in rapid climate change events.

Deep-sea corals are also an important resource to study vital effects because they grow without photosymbionts and grow in a relatively homogeneous environment with minimal variations in temperature and the composition of co-existing water. Therefore, offsets from equilibrium that we observe in any chemical proxies can be attributed to biological processes associated

with calcification. Previous work in surface and deep-sea corals has found evidence of isotopic disequilibrium in $\delta^{13}C$ and $\delta^{18}O$ (Adkins et al., 2003; Emiliani et al., 1978; McConnaughey, 1989; Weber and Woodhead, 1970; Weber, 1973). McConnaughey attributes these offsets in surface corals to kinetic and metabolic effects. However light-induced metabolic effects cannot be invoked to explain offsets in deep-sea corals because they do not have any photosymbionts. Radiocarbon dating of modern corals and their surrounding dissolved inorganic carbon (DIC) also indicate that the skeletal material of deep-sea coral is drawn almost entirely from the ambient inorganic carbon pool and not from respired CO_2 (Adkins et al., 2003). Due to the correlation between growth banding and stable isotopes within individual corals, Adkins et al. (2003) proposed that vital effects in deep-sea corals involve a thermodynamic response to a biologically induced pH gradient in the calcifying region. Watson (2004) proposed a surface entrapment model in which growth rate, diffusivity, and the surface layer thickness all control crystal composition. In this model, the trace element or isotope composition of the crystal is determined by the concentration of that element in the near-surface region and the outcome of the competition between crystal growth and ion migration in the near-surface region.

More recently, Ghosh et al. (2006) found evidence of an anomalous enrichment in $\Delta 47$ values in winter growth bands in a *Porites* sample from the Red Sea, suggesting that surface corals may have a vital effect in this parameter. Here we look at a variety of deep-sea corals grown from different locations, and analyze their Δ_{47} values to develop a modern calibration for carbonate clumped isotope thermometry and to investigate the mechanisms of vital effects.

2.3 METHODS

Samples examined in this study were obtained from the Smithsonian collection (National Museum of Natural History). We focused on *Desmophyllum sp*., *Caryophyllia sp*., and

Ennalopsammia sp. collected from a variety of locations and depths. One *Porities sp.* coral from the Red Sea was also analyzed. Isotopic measurements were made on pieces from the septal region of the coral that were cut using a dremel tool. For each clumped isotope measurement, eight to fifteen mg from each coral was analyzed. The outsides of the coral were scraped with a Dremel tool to remove any organic crusts. The sample was then digested in 103% anyhydrous phosphoric acid at 25°C overnight. The product CO_2 was extracted and purified using methods described previously (Ghosh et al., 2006).

Evolved CO_2 was analyzed in a dual inlet Finnigan MAT-253 mass spectrometer with the simultaneous collection of ion beams corresponding to masses 44-49 to obtain Δ_{47}, Δ_{48}, Δ_{49}, $\delta^{13}C$ and $\delta^{18}O$ values. The mass 47 beam is composed of $^{17}O^{13}C^{17}O$, $^{17}O^{12}C^{18}O$ and predominantly $^{18}O^{13}C^{16}O$ and we define R^{47} as the abundance of mass 47 isotopologues divided by the mass 44 isotopologue. ($R^{47}=[^{17}O^{13}C^{17}O+ {}^{17}O^{12}C^{18}O+{}^{18}O^{13}C^{16}O]/[^{16}O^{12}C^{16}O]$.) Δ_{47} is reported relative to a stochastic distribution of isotopologues for the same bulk isotopic composition. ($\Delta_{47}=(((R^{47}_{measured}/R^{47}_{stochastic})-1)- ((R^{46}_{measured}/R^{46}_{stochastic})-1)- ((R^{45}_{measured}/R^{45}_{stochastic})-1))*1000.$) Masses 48 and 49 were monitored to detect any hydrocarbon contamination. Measurements of each gas consisted of 8−26 acquisitions, each of which involved 10 cycles of sample-standard comparison with an ion integration time of 20 s per cycle. Internal standard errors of this population of acquisition to acquisition for Δ_{47} ranged from 0.005−0.01‰, (1−2°C) while external standard error ranged from 0.002−0.014‰ (0.4−2.7°C). The internal standard error for $\delta^{13}C$ ranged from 0.5−1 ppm and the internal standard error for $\delta^{18}O$ ranged from 1−3 ppm.

2.4 RESULTS

Table 2.1 summarizes results of isotopic analyses of all coral samples investigated in this study. A 0.16‰ range in Δ_{47} was observed among coral samples having an estimated range in

growth temperature of 2−25°C (Table 2.1; Fig. 2.1). Table 2.1 also reports the $\delta^{18}O_{PDB}$ values of corals analyzed in this study, along with growth temperatures, and the $\delta^{18}O$ values of the water from which the corals grew. The $\delta^{18}O$ of the water from which the coral grew was reconstructed through a combination of the LEVITUS salinity database (http://ingrid.ldeo.columbia.edu/SOURCES/.LEVITUS94/.ANNUAL/.sal/) and the NASA $\delta^{18}O$ of seawater database (http://data.giss.nasa.gov/cgi-bin/o18data/geto18.cgi). The LEVITUS database is more finely gridded for salinity than the NASA database. So we determined the relationship between $\delta^{18}O$ of the seawater and salinity near the sample site and used the salinity as determined by LEVITUS to calculate the $\delta^{18}O$ of the seawater from the $\delta^{18}O$ of the seawater vs. salinity relationship. The total error on the calculated $\delta^{18}O_{sw}$ calculated ranged from 0.1−0.2‰.

Figure 1 plots the Δ_{47} values of deep-sea corals vs. their nominal growth temperatures. The *Porites* surface coral BIR-1 has significant error bars in the temperature axis, unlike the deep-sea coral samples (where growth temperatures do not vary significantly seasonally), because it was collected in the Red Sea and sea surface temperatures range from 22−28°C through the year (Ghosh et al., 2006). Ghosh et al. (2006) found vital effects in the winter band of BIR-1. Our analyses are of one annual band that was crushed and homogenized, and we do not observe any offsets from equilibrium. This inconsistency could be because winter bands do not contribute a significant portion of the annual cycle.

The relationship of Δ_{47} to temperature is similar to that of inorganic precipitates. In a plot of Δ_{47} vs. $1/T^2$ the two species of solitary corals, Desmophyllum (slope: 0.0495 ± 0.012; intercept: 0.1052 ± 0.1557) and Caryophyllia (slope: 0.05545 ± 0.008; intercept: 0.0302 ± 0.1116) are indistinguishable in slope and intercept from the inorganic calibration line (slope: 0.0597 ± 0.004; intercept:-0.03112 ± 0.0475). Note, however, that these equations are not suitable for

Table 1

Name	Genus	$\delta^{13}C$	$\delta^{18}O$mineral	Growth Temperature (^{o}C)	Δ_{47}	error in Δ_{47}	$\delta^{18}O_w$
47413	Desmophyllum	-5.009	0.723	7.9	0.733	0.007	-0.439
47413	Desmophyllum	-6.274	0.343	7.9	0.736	0.006	-0.439
47413	Desmophyllum	-4.877	0.686	7.9	0.732	0.009	-0.439
47413	Desmophyllum	-4.720	0.764	7.9	0.736	0.008	-0.439
47413	Desmophyllum	-6.285	-0.006	7.9	0.722	0.005	-0.439
47413	Desmophyllum	-4.544	0.833	7.9	0.726	0.007	-0.439
47413	Desmophyllum	-6.286	0.032	7.9	0.697	0.006	-0.439
80404	Desmophyllum	-1.230	1.535	13.1	0.707	0.009	0.25
80404	Desmophyllum	-1.826	1.764	13.1	0.695	0.008	0.25
80404	Desmophyllum	-1.185	1.611	13.1	0.717	0.010	0.25
47407	Desmophyllum	-5.640	0.768	4.2	0.749	0.006	-0.047
48738	Desmophyllum	-1.478	2.987	9.8	0.762	0.010	0.624
48738	Desmophyllum	-1.567	2.968	9.8	0.715	0.005	0.624
48738	Desmophyllum	-4.897	1.537	9.8	0.727	0.008	0.624
47409	Desmophyllum	-3.640	1.171	2.3	0.772	0.008	-0.088
62308	Desmophyllum	-4.725	1.147	3.7	0.744	0.010	0.5
77019	Ennallapsammia	-0.212	3.670	14.3	0.675	0.004	0.95
47531	Ennallapsammia	-1.603	0.982	7.5	0.738	0.009	-0.14
49020	Caryophyllia	0.708	1.548	17.4	0.688	0.011	0.907
45923	Caryophyllia	0.289	3.139	4.6	0.744	0.008	0.68
1010252	Caryophyllia	-0.115	2.818	6.1	0.744	0.008	0.222
BIR-1	Porites	-1.092	-3.720	25.2	0.650	0.006	1.91
BIR-2	Porites	-1.183	-3.670	25.2	0.639	0.006	1.91
BIR-3	Porites	-1.186	-3.659	25.2	0.648	0.005	1.91
BIR-4	Porites	-1.195	-3.664	25.2	0.615	0.007	1.91

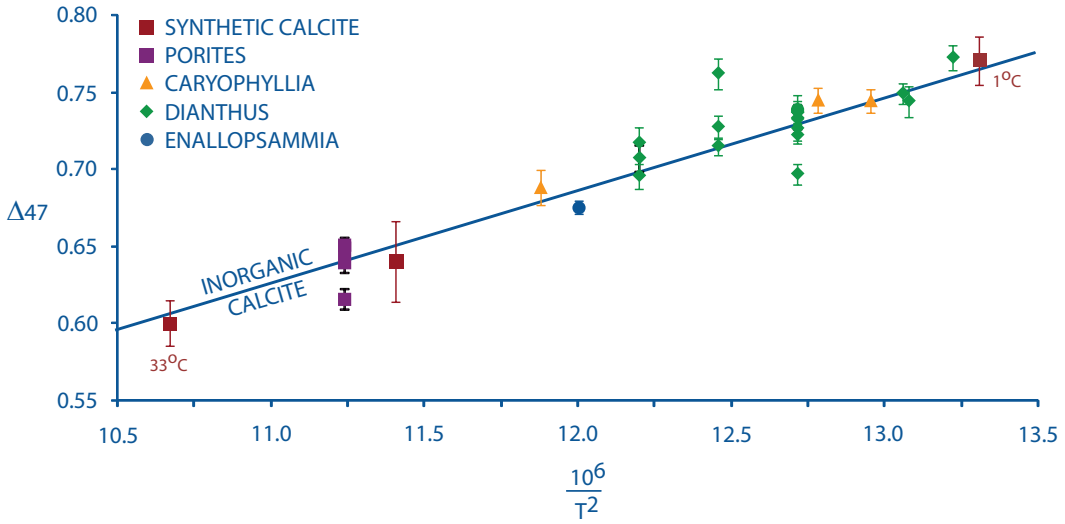

Figure 2.1: Clumped isotope calibratino of deep-sea corals and *Porites*, a surface coral. The dashed line is the inorganic calibration line as determined by measuring CO2 produced from synthetic carbonates grown in the laboratory at known and controlled temperatures (Ghosh et al. 2006).

extrapolation beyond the range of observations (0−50°C).

2.4.i Internal and External Standard Errors

The average standard error for our Δ_{47} measurements are in agreement with the shot noise limit predicted for the analyses (Fig 2.2). Samples that were run for several hours have the lowest standard error, on the order of 0.005‰, which corresponds to a 1°C temperature change for low temperatures on the Ghosh et al. (2006) temperature scale. Several of the corals examined in this study were analyzed multiple times each, permitting us to estimate the external reproducibility for individual measurements of a given sample. This external standard error (i.e., the standard error of the average of multiple extractions) ranges from 0.005 to 0.014‰ (1−2.8°C), and decreases with the number of measurements (Fig 2.3). If one extraction of sample 47413 (a measurement we suspect was compromised by exchange of water) is excluded from these statistical calculations, the external standard error ranges from 0.002−0.014‰ (0.4−2.8°C). This external standard error is still larger than the expected shot noise errors for the same samples (~ 0.0025−0.0040‰).. The difference in external standard error from expected shot noise limits may be due to sample heterogeneity, unaccounted for analytical fractionations, or contaminants in the sample.

The reproducibility we document has implications for future analyses of deep-sea corals. If sample size is limited, the best precision attainable is 0.005‰ (±1°C). However if sample size is not the limiting factor, the coral is homogenous, and not contaminated or otherwise analytically fractionated, precision is demonstrably as good as 0.002‰ (±0.4°C).

2.5. DISCUSSION

2.5.i Relationship of Δ47 to Temperature

For two of the solitary coral genera analyzed in this study, each exhibit slopes and in-

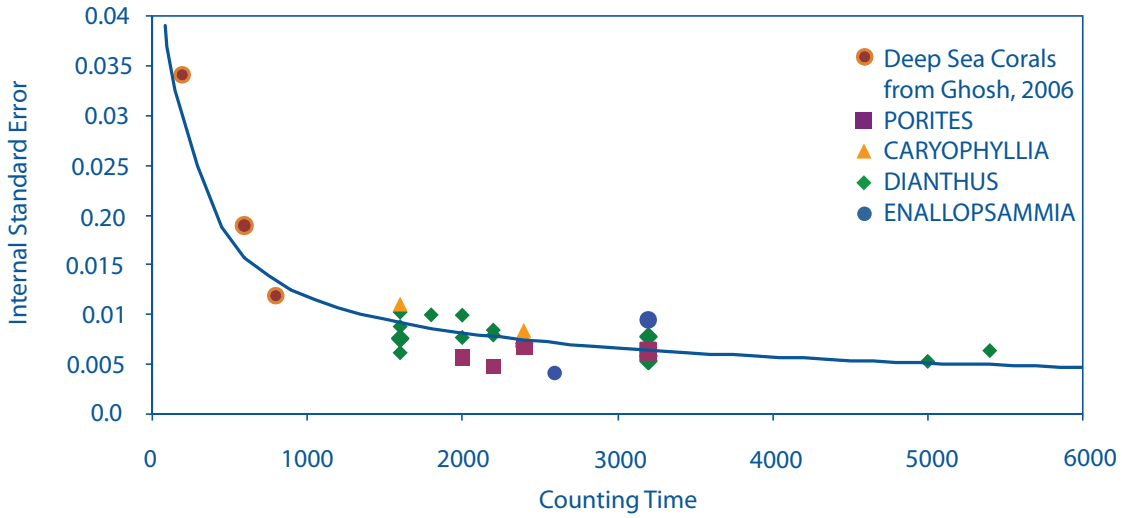

Figure 2.2: Internal standard error of our measurements with counting time. The dark line is the shot noise calculation. The error in our measurements is dominated by shot noise errors and decreases with increasing counting time.

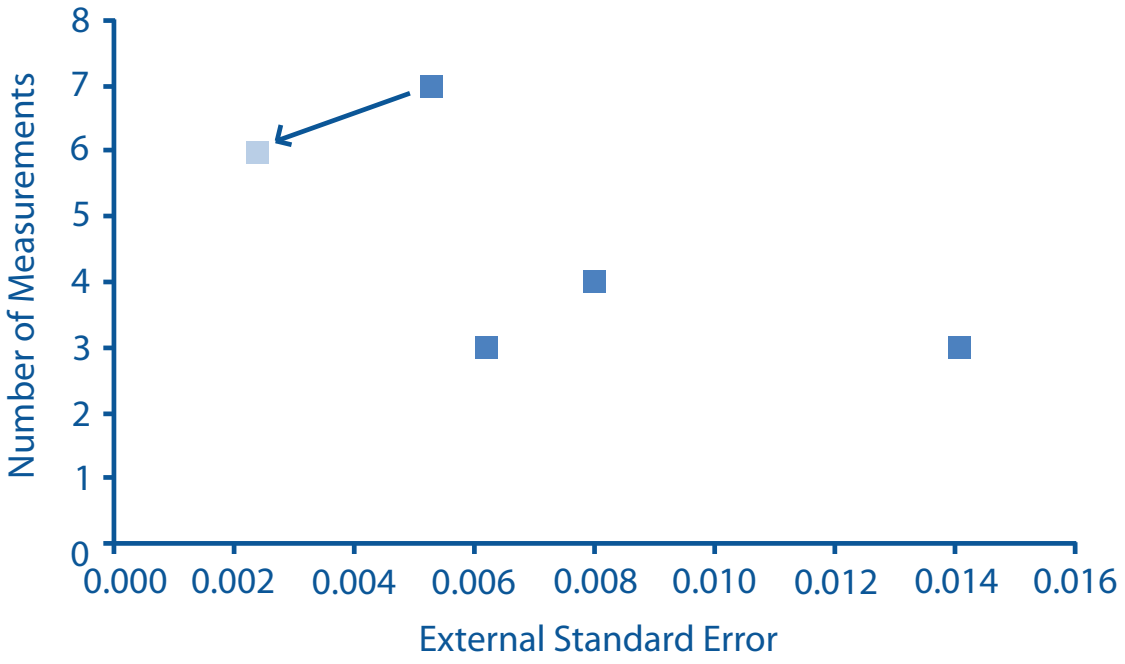

Figure 2.3: A figure of the external standard error of our measurements. Multiple replicates decreases the standard error of our measurements. The arrow indicates how coral 47413 changes if one extraction (suspected of having exchanged with water) is removed.

tercepts in a plot of Δ_{47} vs. $1/T^2$ that are within error of the inorganic calibration line (Fig 2.1). Since the publication of the Ghosh et al. (2006) calibration, several more measurements have been made of inorganic calcite, foraminifera, mollusks, and soil carbonates having independently known growth temperatures. Most of these previous measurements are indistinguishable from the inorganic calibration line (Came et al., 2007; Daeron, 2007; Tripati, 2007). There have however been nonequilibrium results obtained for speleothems and some synthetic carbonates (Affek et al., 2008; Guo, 2009). A recently published calibration for inorganic synthetic calcite (Dennis and Schrag, 2010) also disagrees with the Ghosh et al. (2006) result at low temperatures (< ~ 15˚C). The source of this discrepancy is unclear; it could reflect some combination of analytical artifacts (including intralaboratory calibration discrepancies) and/or kinetic isotope effects in carbonate synthesis reactions in either or both studies. We simply note here that this study presents data for 15 samples analyzed in this low temperature range, and they follow a temperature-dependence closely similar to that proposed by Ghosh et al. (2006), but steeper than that presented by Dennis and Schrag (2010). We suggest two straightforward explanations for this result: either the Ghosh et al. (2006) data reflect a kinetic isotope effect at low temperature that is mimicked by a vital effect in deep-sea corals (and, similarly, other classes of organisms previously observed to conform to the Ghosh et al. (2006) trend), yet independent of the vital effect on $\delta^{18}O$ and $\delta^{13}C$ in those corals (see below); or the Dennis and Schrag (2010), calibration is influenced by a kinetic isotope effect in low-temperature experiments. In the absence of any additional constraints, the second of these seems to us to be the more plausible explanation, and we will presume this for the rest of this discussion. But, we emphasize that inorganic calibrations will likely remain a subject of ongoing research and this interpretation should be revisited as new data come to light.

Three individual analyses made as part of this study are inconsistent with the inorganic

calcite calibration trend (i.e., differ from it by more than 2 sigma external error). Two of the outliers are an extraction from each of the samples 47413 and 48738. These outliers were extractions from corals that have been analyzed several times, and in both cases all other extractions from that sample exhibited no offset in Δ_{47} from the inorganic calibration line. Sample 47413 is unusual because, although the outlier was free of recognized contaminants, it did have a higher Δ_{47} and lower $\delta^{18}O$ than all the other replicates of that sample. This combination indicates that it could have exchanged with water (Pasadena tap water: 25°C, $\delta^{18}O$ =-8‰) at some point during sample processing. Sample 48738 has an orange organic crust coating it, implying that perhaps it is not modern or that the organic coating was not completely removed prior to sample processing and affected the measurement. In any event, these two measurements are irreproducible exceptions to the otherwise straightforward trend produced by all other analyses, and thus we do not believe they indicate any systematic discrepancy between corals and inorganic calcite in Δ_{47} systematics. The third outlier is 77019, an Enallopsammia from 30°N, 76°W at 494 m of water depth in the core of the Gulf Stream, a region known for seasonal and interannual variations in salinity. This coral is also peculiarly enriched in $\delta^{18}O$ indicating possible uncertainties in the $\delta^{18}O_w$ reconstructed at this site.

The accuracy of deep-sea coral temperature estimates based on the calibration in Figure 2.1 will depend on uncertainties in both the Δ_{47} of the sample and uncertainties in the calibration line, whereas the precision of sample-to sample differences will depend only on the Δ_{47} measurements of samples. If one considers all previous measurements of published and unpublished inorganic and biogenic calibration materials (egg shells, teeth, otoliths, mollusks, brachiopods, corals and foraminifera; we exclude here the recent inorganic data of Dennis and Schrag (2010), discussed above) to be part of a single trend (i.e., because trends defined by each material are

statistically indistinguishable), then they make up a calibration line of slope in Δ_{47} vs. $1/T^2$ space of 0.0548+/-0.0019 and intercept of -0.0303+/-0.0221. The standard error of the calibration is 0.0018‰. If one excludes otoliths, which differ most from the other trends (perhaps due to a small vital effect, or due to inaccuracies in estimated body temperatures, or some other factor) and planktic foraminifera (where the variation in temperature with water depth and season is large and therefore a mean hard to estimate with confidence), the calibration line has a slope and intercept of 0.0562 +/- 0.0020 and 0.0167 +/- 0.0226. The standard error in the calibration is then 0.0019‰. The formal errors in slope and intercept of the overall calibration are trivially small; though one should not extrapolate the fitted trend outside of its range in calibration temperatures (particularly at higher temperatures, where the slope flattens considerably; (Dennis and Schrag 2010, Eiler, 2009). Thus, barring some unrecognized systematic error in all of the calibration data sets, the accuracy of temperature estimates of samples is dominated by error in the Δ_{47} measurement of the sample, which is generally dominated by shot noise error. The shot noise error for Δ_{47} analyses under normal analytical conditions generally levels off (ceases to improve with increased counting time) at ~ 0.005‰ (or ~ 1^{o}C) after 4500 seconds or ~ 20 acquisitions. Current analytical methods require 11 mg of $CaCO_3$ for 4500 seconds (i.e., to achieve 0.005‰ precision). If large amounts of homogeneous sample are available, precision could be improved further by combining data from multiple measurements of 11 mg sample aliquots. Sub degree precisions should be possible in this case. For example, if 11 mg of coral analyzed for 4500+ seconds resulted in a measurement of 2^{o} C with a standard error of 0.005‰, or 1^{o} C, then six 11 mg measurements of the same homogeneous coral could result in a precision as low as 0.002‰ or 0.4^{o}C (plus the small error in the accuracy of the calibration). Or, if three replicate measurements were made for the top of a deep-sea coral and six of the bottom of the same deep-sea coral

(i.e., if one were searching for evidence of temperature change over the course of its growth), the error in the temperature estimate at the top would be ± 0.4°C, the error in the temperature at the bottom would be ± 0.7°C, and the temperature difference (ΔT=top temperature-bottom temperature) would have an error of ± 0.8 (because the two errors would be added in quadrature).

2.5.ii Vital Effects Mechanisms

2.5.ii.a Vital Effects in Corals

Use of deep-sea corals (and other biogenic carbonates) as a paleoceanographic archive is complicated by a set of biological processes commonly referred to as vital effects. Vital effects have been observed in aragonitic corals as offsets from equilibrium in stable isotope and metal/calcium ratios for a given temperature and other equilibrium conditions. Vital effects in corals and other organisms have also been noted to be dependent on growth rate, kinetics, pH, light and to the presence or absences of photosymbionts (Cohen et al., 2002; McConnaughey, 1989; Reynaud et al., 2007; Rollion-Bard et al., 2003; Weber and Woodhead, 1970).

The range of vital effects in conventional, or 'bulk' stable isotope compositions seen in deep-sea corals is 7‰ in $\delta^{18}O$ and 12‰ in $\delta^{13}C$. In contrast, Δ_{47} values do not appear to exhibit any vital effects (i.e., they remain indistinguishable from the inorganic calibration across the full studied temperature range). The analytical method used to determine Δ_{47} values simultaneously generates $\delta^{13}C$ and $\delta^{18}O$ values for the sample; therefore, it is possible for us to evaluate the extent to which each analyzed sample expressed 'vital effects' in their O and C isotope compositions. A plot of $\Delta_{47measured}$- $\Delta_{47expected}$ vs $\delta^{18}O_{measured}$- $\delta^{18}O_{expected}$ does not show any correlated trends, and there are no systematic deviations in $\Delta_{47measured}$ from $\Delta_{47expected}$ even when there are clearly offsets in $\delta^{18}O$ (Fig 2.4). While our study was not designed to examine the mechanisms of vital effects, our results offer new constraints on this problem.

The following sections compare our results with the predictions one would make based on various previously proposed vital effect mechanisms.

2.5.ii.b Diffusion

Diffusion of CO_2 through a lipid bilayer or of different carbonate species across a foraminifer shell has been proposed as a part of different vital effect models (Adkins et al., 2003; Zeebe et al., 1999, Erez, 2003). While we do not have a first principle understanding of how this type of diffusion might affect the Δ_{47} value, we can use other types of well-known diffusion to inform this discussion. The kinetic theory of gases predicts that a gas that is diffused through a small aperture ('Knudsen diffusion') will be depleted in heavy isotopes relative to the residual gas it leaves behind. This behavior is described by the equation $R^j_{diffused} = R^j_{residue}(M^i/M^j)^{0.5}$ where R^j is the ratio of the concentration of isotopologue j to i and M is the mass.

Knudsen diffusion predicts that for a CO_2 population that has undergone diffusive fractionation, the diffused gas will be 11.2‰ lower in $\delta^{13}C$, and 22.2‰ lower in $\delta^{18}O$, but only 0.5‰ higher in Δ_{47}. This seemingly counterintuitive behavior is due to the nonlinear dependence of the stochastic abundances of mass-47 CO_2 isotopologues on the bulk isotopic composition (Eiler and Schauble, 2004). For natural isotopic compositions, the stochastic abundance increases more for an incremental change in $\delta^{13}C$ or $\delta^{18}O$ than does the vector that describes diffusive fractionation in $\delta^{13}C$, $\delta^{18}O$ and Δ_{47} space. Therefore, a diffused population of gas would be more depleted in $\delta^{13}C$ and $\delta^{18}O$ but higher than expected in Δ_{47}.

Similarly, gas phase inter diffusion where gas A diffuses through gas B is described by the relation $D_a/D_a' = \{(M_a+M_b)/(M_aM_b) \times (M'_aM_b)/(M'_a+M_b)^{0.5}\}$, where M_a is the mass of the diffusing molecule, M_b is the mass of the gas through which gas A is diffusing and the primes indicate the presence of a heavy isotope. The gas phase diffusion of CO2 through air generates

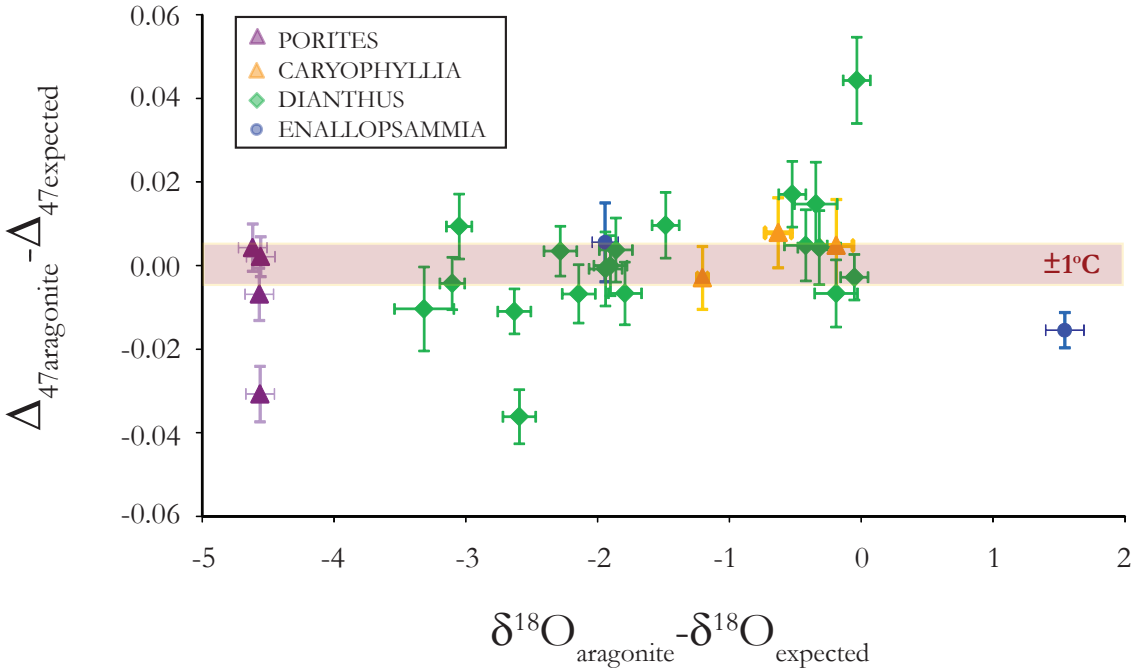

Figure 2.4: Offsets from equilibrium in Δ_{47} and $\delta^{18}O$. The biggest offsets in Δ_{47} are from corals with multiple extractions and every other extraction from those corals have no offset in Δ_{47}.

fractionations of -4.4‰ for $\delta^{13}C$, -8.7‰ for $\delta^{18}O$ and +0.3‰ for Δ_{47}. The enrichment of Δ_{47} in the diffused phase is again due to the relatively strong dependence of the stochastic abundance of mass-47 CO_2 on the bulk isotopic composition.

Isotopic fractionations caused by diffusion of molecules through a liquid medium are generally smaller than those associated with gas-phase diffusion. For instance, the ratio of diffusion coefficients of $^{12}CO_2$ and $^{13}CO_2$ in water is 1.0007 (O'Leary, 1984), whereas the gas phase interdiffusion equation, taking the medium to be H_2O predicts a fractionation factor of 1.0032. However, these condensed phase diffusive fractionations are generally described through a power-law relationship (i.e., the fractionation factor scales as the ratio of masses to some power, generally less than 0.5) (Bourg and Sposito, 2008). In this case, the mass dependence of the diffusive fractionation remains the same as for Knudsen diffusion, and the slope followed in a plot of Δ_{47} vs. $\delta^{18}O$ or $\delta^{13}C$ will remain the same. If so, then liquid phase diffusion of CO_2 should result in fractionations of -0.7‰ for δ13C (i.e., the experimental constraint), -1.6‰ for $\delta^{18}O$ and +0.036‰ for Δ_{47}. On Figure 2.5 we have also indicated what 10% of the Knudsen and gas phase interdiffusion vector are to emphasize the difference between the scale of the different vectors. If deep-sea coral growth involved nonequilibrium isotopic fractionations that were dominated by diffusion across a lipid bilayer or in an aqueous medium, then a plot of Δ_{47} vs. $\delta^{18}O$ might have the same slope as the vectors that describe the types of diffusion discussed above. However the data is inconsistent with any of these predicted slopes (Fig 2.5). In addition, all of the diffusive processes predict $\delta^{13}C$ variations smaller than $\delta^{18}O$ variations, which is opposite to what is seen in deep-sea corals.

2.5.ii.c Mixing

The stochastic distribution that defines the reference frame for reporting Δ_{47} values has a

subtle saddle-shape curvature in a 3-dimensional plot of $\delta^{13}C$ vs. $\delta^{18}O$ vs. R^{47}. Therefore, conservative mixing of two CO_2 populations with the same Δ_{47} but different $\delta^{13}C$ and $\delta^{18}O$ leads to a mixed population having a different Δ_{47} value than the weighted sum of the Δ_{47} values of the end members (Eiler and Schauble, 2004).

Deep-sea corals have a large variation in $\delta^{13}C$ and $\delta^{18}O$ and could possibly produce Δ_{47} signals solely from this mixing effect. The range of variations seen in a single coral can be as large as 12‰ in $\delta^{13}C$ and 7‰ in $\delta^{18}O$ (Adkins et al., 2003). Two example end members seen in $\delta^{13}C$ and $\delta^{18}O$ are $\delta^{13}C$=-10‰ and $\delta^{18}O$=-2‰, and $\delta^{13}C$=2‰ and $\delta^{18}O$=5‰. If the stable isotopic variation in a deep-sea coral reflects variation in the DIC pool that the coral was using for calcification, we can calculate what magnitude of Δ_{47} offset would result from mixing between the isotopic end members of the DIC pool. However, the carbonate species of interest for calcification is not CO_2 (and its Δ_{47} value) but CO_3 and its corresponding ^{13}C-^{18}O clumped isotopologue. The relevant isotope exchange reaction for CO_3 species is:

$^{12}C^{18}O^{16}O_2^{2-} + {}^{13}C^{16}O_3^{2-} <--> {}^{13}C^{18}O^{16}O_2^{2-} + {}^{12}C^{16}O_3^{2-}$.

So, we calculated the mixing effect on Δ_{63} (i.e., enrichment in mass-63 carbonate ion isotopologues, analogous to the Δ_{47} values of CO_2) and then converted this to a Δ_{47} value that would be measured in a coral skeleton. If both the high- and low- $\delta^{13}C$ and $\delta^{18}O$ share a common "Δ_{63}" value then we predict the amplitude of this mixing effect is as large as 0.02‰ for the case of 50% of each end member (which would generate the largest Δ_{63} offset, and still a relatively large offset in $\delta^{18}O$). Because phosphoric acid is believed to produce CO_2 having a Δ_{47} value that is offset by a constant amount from the Δ_{63} value of reactant carbonate (for a fixed temperature of reaction) this 0.02‰ enrichment due to mixing should be directly inherited by analyzed CO_2 (Guo et al., 2009). It is clear that this mixing model is inconsistent with the data, as there is no curvature to

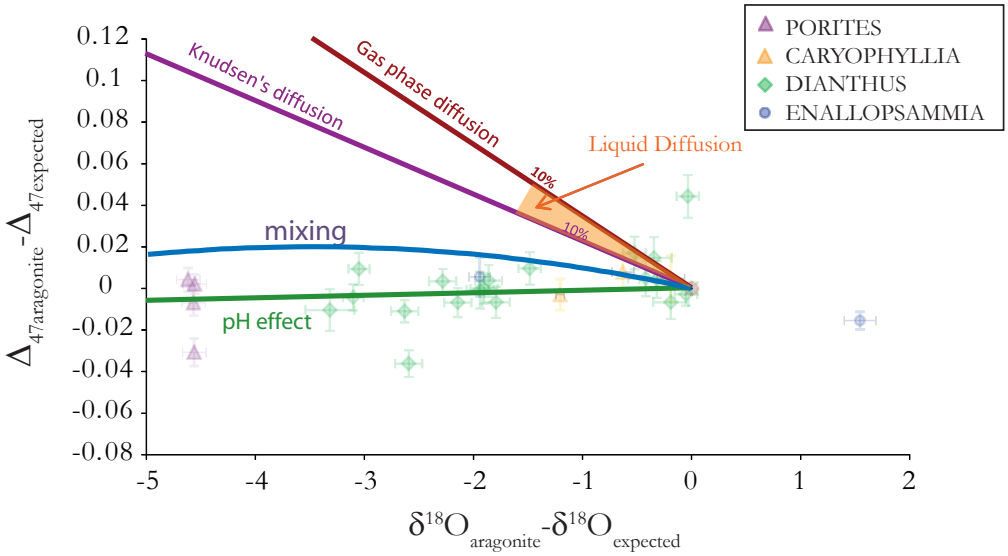

Figure 2.5: Vectors describing how various processes effect Δ_{47} and $\delta^{18}O$. Diffusive and mixing processes cannot explain the coupled variation in Δ_{47} and $\delta^{18}O$; however pH effects can.

the Δ_{47} vs. $\delta^{18}O$ trend unlike the mixing model (Figure 2.5). However, it is possible that mixing accompanied by re-equilibration would generate a horizontal line, and thus be more consistent with the data. Further experiments are needed to determine the rate that carbonate precipitating from DIC incorporates the different clumped carbonate species in DIC and whether mixing and subsequent re-equilibration would be recorded in the precipitating carbonates.

2.5.ii.d. pH

It has been demonstrated for inorganically precipitated carbonates that higher pH values (and thus higher CO_3^{2-} proportions in DIC) result in isotopically lower $\delta^{18}O$ values (McCrea, 1950; Usdowski et al., 1991). This observation has been explained by the pH dependent speciation of the DIC pool from which carbonate precipitates and the different fractionation factors between water and these DIC species. At seawater like pHs HCO_3^- dominates and at high pHs CO_3^{2-} dominates the DIC. McCrea (1950) and Usdowski et al. (1991) demonstrated that if calcium carbonate is quantitatively precipitated from a bicarbonate-carbonate solution, the oxygen isotopic composition of the solid reflects the weighted average of all the fractionation factors with respect to water for all the carbonate species. Zeebe (1999) exploited this observation to explain the variation seen in the inorganic carbonate data in Kim and O'Neil (1991) and existing stable oxygen isotope ratios of foraminiferal calcite.

It would be helpful to understand how the clumped isotope composition of the DIC varied with pH. Guo et al., (2008) theoretically estimated the Δ_{63} values of dissolved carbonate species in water; at 300K, CO_3^{2-} has a predicted value of 0.403‰, whereas HCO_3^- has a value of 0.421‰. While the absolute values of these calculated Δ_{63} estimates vary with the parameterization of the computational model, the offset between CO_3^{2-} and HCO_3^- remains constant at ~ 0.018‰, and thus is likely a robust feature of the calculation (Guo et al., 2008). The equivalent

difference in $\delta^{18}O$ at 19°C is 34.3‰ for HCO3- and 18.4‰ for CO_3^{2-} (Zeebe, 1999).

Given Zeebe's model of precipitation and Guo et al.'s (2008) calculated differences in Δ_{63} between HCO_3- and CO_3^{2-}, we estimate the pH dependence of Δ_{63} of carbonate (which we take to be proportional to the measured Δ_{47} of CO_2 extracted from those carbonates). A change in pH from 7.9 to 9.8 leads to a change in CO_3^{2-} as a proportion of all DIC from 5% to 75% and a predicted change in Δ_{63} of carbonates by 0.0126‰ and in $\delta^{18}O$ of carbonates by 10.92‰. Thus, Zeebe's model predicts a slope of Δ_{47} vs. $\delta^{18}O$ measured in carbonate that closely approaches 0. However since the absolute values of the Δ_{63} estimates of the DIC species (and their relative difference to the calcium carbonate is unknown) the pH vector can only be plotted on Figure 2.5 with certain assumptions. Here we assume that when there is no offset in $\delta^{18}O$ from equilibrium, similarly there is no offset in Δ_{47} from the inorganic calibration line. That is, we are examining the sensitivity to pH not the absolute values of the Δ_{63} of the DIC species implied by different computational models. The resulting pH vector is consistent with our results (Fig 2.5).

2.5.ii.e Other Vital Effect Models

Watson (2004) proposed a model for near-surface kinetic controls on stable isotope compositions in calcite crystals, which also involves a sensitivity to DIC speciation. The model is based on the idea that the concentration of a particular trace-element in a crystal (which we could take to be an isotopologue of carbonate ion for our purposes) is primarily determined by two factors: the concentration of the element in the near-surface region of the crystal and the competition between crystal growth and ion migration in the near-surface region. There are three key regions, the specific growth surface which is a monolayer of atoms, the near-surface region and the bulk crystal lattice. The growth surface of the crystal could (due to its distinct structure) have an equilibrium composition that is different from that of the crystal lattice. Thus if the trace element

is selectively enriched (or depleted) on the growth surface, and if the diffusivity of that element in the near-surface region of the crystal is low, then the anomalous surface composition may be partially or completely preserved within the growth sector formed behind the growth surface. If however the diffusivity of the element in the near-surface region of the crystal is high, the newly formed crystal lattice is in equilibrium with the fluid it is growing from and has a different composition than the growth surface. Watson has explored this growth entrapment effect in various trace elements (Okorokov et al., 1996) and also extended it to oxygen isotopes (Watson, 2004). The Watson model identifies two potential sources of ^{18}O for calcite, CO_3^{2-} species alone or the weighted average of carbonate and bicarbonate ion (i.e., as in Zeebe's model). Carbonate ion is lower in $\delta^{18}O$ than solid carbonate when equilibrated with a common water. So, the Watson model predicts that if carbonate ion alone is added to growing solid carbonate, the solid will be lower than equilibrium for fast growth and approach equilibrium for slow growth. If instead both bicarbonate and carbonate ion contribute to solid, faster growth rates will be associated with higher-than equilibrium $\delta^{18}O$ values in the solid (because the higher $\delta^{18}O$ value of bicarbonate will be 'trapped' in the solid structure). It has been suggested that the $\delta^{18}O$ of aragonite decreases with increased growth rate in deep sea corals, based on textural variations of $\delta^{18}O$ within individual corals (Adkins et al., 2003). This observation is consistent with the Watson model for the case that carbonate ion alone contributes to the solid.

Clumped isotopes cannot yet be applied to the Watson model because there are several unknown factors. The Δ_{63} offset between CO_3^{2-}(aq) and CO_3^{2-}(s) is poorly known. The equilibrium partitioning in clumped isotopes between the fluid and the growth surface and the equilibrium partitioning between the fluid and the bulk crystal lattice is also unknown. The Δ_{63} of the CO_3^{2-} in aragonite is 0.430‰ (Schauble et al., 2006) while the Δ_{63} of HCO_3- and CO_3^{2-} in DIC has

been predicted to be 0.421‰ and 0.403‰, respectively (Guo, 2009); however, because the Δ63 offset between CO_3 in water and CO_3 in aragonite is sensitive to the solvent model used to calculate the fractionation factors of the dissolved species (see above pH discussion), Guo's calculations of Δ63 cannot confidently be used to evaluate Watson's (2004) surface entrapment model. If however all these factors were known, then clumped isotopes could be a test for the Watson model.

McConnaughey (1989) used the difference between symbiont bearing and nonsymbiont bearing aragonitic coral species from the same growth environment to constrain the chemical mechanisms behind vital effects. He determined that there is a kinetic effect and a metabolic effect fractionating oxygen and carbon isotopes in corals. The kinetic effect is due to the kinetic isotope effects (KIE) that occur during CO_2 hydration and hydroxylation. Therefore the linear variations seen in $\delta^{13}C$ and $\delta^{18}O$ are due to the incomplete isotopic equilibration of $CaCO_3$ and H_2O. Clumped isotopes cannot be used yet to evaluate Mcconaughey's kinetic fractionation model of stable isotope vital effects in corals as the KIE of CO_2 hydration and hydroxylation on clumped isotopes is currently unknown. However, if isotopic disequilibrium due to CO_2 hydration and hydroxylation is the dominant control of vital effects in corals then the magnitude of $\Delta_{47}/\delta^{18}O$ from this effect is constrained to be less than the observed variation in Figure 2.5. Rayleigh fractionation has also been proposed as a possible vital effects mechanism for the distribution of metals in corals (Cohen et al., 2006; Gagnon et al., 2007; Holcomb et al., 2009). This model assumes that there is an initial solution that is close to seawater composition which then undergoes closed system precipitation. Again clumped isotopes cannot yet be used to evaluate this vital effect mechanism as the partition coefficient of Δ_{47} for inorganic aragonite (where the partition coefficient is defined as: $D_{arag}\Delta_{47}=(\Delta_{47})_{aragonite}/(\Delta_{47})_{seawater}$) is unknown. The relevant

F, or extent of precipitation, is also unknown.

2.6 CONCLUSIONS

We present the relationship between the abundance of clumped isotopologues in CO_2 produced by phosphoric digestion of deep-sea corals and the coral's relationship to growth temperature. Deep-sea corals exhibit a temperature-dependent trend in Δ_{47} value that is indistinguishable in slope and intercept from inorganic calcite. This result indicates that deep sea corals can be used for paleothermometry, with precisions as good as ~ 0.5°C. We also observe no vital effects in Δ_{47} for samples that display large vital effects in $\delta^{18}O$. This result is inconsistent with the predicted effects of diffusion or mixing for vital effects. However, pH effects could explain the observed variations in Δ_{47} and $\delta^{18}O$. In contrast to the results for Red Sea corals presented in Ghosh et al. (2006), we find no evidence of vital effects in surface corals. One of several possible explanations for this difference is that we analyzed mean annual bands rather than specific seasons (i.e., perhaps vital effects are specific only to relatively thin winter-growth bands in surface corals). Future work would involve a more detailed analysis of surface corals within annual bands to confirm the existence and determine the nature of any vital effect.

The degree-level errors in temperature in clumped isotope thermometry indicate that it is most suitable for thermocline and sea surface temperature studies, where temperature ranges are of order 10°C. However, sub degree precision is possible by averaging multiple replicates of homogeneous samples, making deep sea ocean temperatures studies (where temperature ranges are typically a few degrees) feasible.

Previous estimates of deep-sea temperature change across glacial/interglacial cycles have been made, using a combination of Mg/Ca ratios, or $\delta^{18}O_w$ with sea level curves. It is thought that in the deep Pacific the temperature changed 2°C, and the Atlantic changed by 4°C, between

MIS 5c and by 2°C (Cutler et al., 2003). Given the appropriate samples and sufficient effort at analytical replication, the clumped isotope thermometer should be able to further constrain glacial/interglacial temperature changes in the deep ocean.

References

Adkins, J. F., Boyle, E. A., Curry, W. B., and Lutringer, A., 2003. Stable isotopes in deep-sea corals and a new mechanism for "vital effects". Geochim Cosmochim Ac 67, 1129−1143.

Adkins, J. F., McIntyre, K., and Schrag, D. P., 2002. The salinity, temperature, and d18O of the glacial deep ocean. Science 298, 1769−1773.

Affek, H. P., Bar-Matthews, M., Ayalon, A., Matthews, A., and Eiler, J. M., 2008. Glacial/interglacial temperature variations in Soreq cave speleothems as recorded by [`]clumped isotope' thermometry. Geochimica et Cosmochimica Acta 72, 5351−5360.

Blunier, T. and Brook, E., 2001. Timing of millennial-scale climate change in Antarctica and Greenland during the last glacial period. Science 291, 109−112.

Bourg, I. C. and Sposito, G., 2008. Isotopic fractionation of noble gases by diffusion in liquid water: Molecular dynamics simulations and hydrologic applications. Geochim Cosmochim Ac 72, 2237−2247.

Came, R. E., Eiler, J. M., Veizer, J., Azmy, K., Brand, U., and Weidman, C. R., 2007. Coupling of surface temperatures and atmospheric CO2 concentrations during the Palaeozoic era. Nature 449, 198−201.

Chappell, J. and Shackleton, N. J., 1986. Oxygen isotopes and sea level. Nature 324, 137-140.

Cohen, A., Owens, K. E., Layne, G., and Shimizu, N., 2002. The effect of algal symbionts on the accuracy of Sr/Ca paleotemperatures from coral. Science 296, 331−333.

Cohen, A. L., Gaetani, G. A., Lundalv, T., Corliss, B. H., and George, R. Y., 2006. Compositional variability in a cold-water scleractinian, Lophelia pertusa: new insights into "vital effects". Geochem Geophy Geosy 7, doi:10.1029/2006GC001354.

Cutler, K. B., Edwards, R. L., Taylor, F. W., Cheng, H., Adkins, J., Gallup, C. D., Cutler, P. M.,

Burr, G. S., Chappell, J., and Bloom, A. L., 2003. Rapid sea-level fall and deep-ocean temperature change since the last interglacial. Earth Planet Sc Lett 206, 253−271.

Daeron, M., Quade, J., Eiler, J 2007. Clumped-Isotope thermometry of modern pedogenic carbonates. Agu Fall Meeting Abstracts

Dennis, K. J. and Schrag, D. P., 2010. Clumped isotope thermometry of carbonatites as an indicator of diagenetic alteration. Geochim Cosmochim Ac 74, 4110−4122.

Eiler, J. A., Schauble, E., and Kitchen, N., 2003. (Coo)-C-13-O-18-O-16 in Air. Geochim Cosmochim Ac 67, A86.

Eiler, J. M. and Schauble, E., 2004. 18O13C16O in earth's atmosphere. Geochimica et Cosmochimca Acta 68, 4767−4777.

Eiler, J., Bonifacie, M., and Daeron, M, 2009. 'Clumped Isotope' Thermometry for High-Temperature Problems. Geochimica et Cosmochimica Acta Conference Abstratcs, A322.

Emiliani, C., 1955. Pleistocene temperatures. Journal of Geology 63, 538−578.

Emiliani, C., Hudson, J. H., Shinn, E., and George, R. Y., 1978. Oxygen and carbon isotopic growth record in a reef coral from the Florida Keys and a deep-sea coral from Blake Plateau. Science 202, 627−629.

Epstein, S., Buchsbaum, R., Lowenstam, H. A., and Urey, H. C., 1953. Revised carbonate-water isotopic temperature scale. Geol. Soc. Amer. Bull. 64, 1315−1326.

Gagnon, A. C., Adkins, J. F., Fernandez, D. P., and Robinson, L. F., 2007. Sr/Ca and Mg/Ca vital effects correlated with skeletal architecture in a scleractinian deep-sea coral and the role of Rayleigh fractionation. Earth Planet Sc Lett 261, 280−295.

Ghosh, P., Adkins, J. F., Affek, H., Balta, B., Guo, W., Schauble, E. A., Schrag, D. P., and Eiler, J. M., 2006. 13C-18O bonds in carbonate minerals: A new kind of paleothermometer. Geochimica

et Cosmochimca Acta 70, 1439−1456.

Guo, W., 2009. Carbonate Clumped Isotope Thermometry: Application to Carbonaceous Chondrites & Effects of Kinetic Isotope Fractionation, California Institute of Technology.

Guo, W., Daeron, M., Niles, P., Genty, D., Kim, S. T., Vonhof, H., Affek, H., Wainer, K., Blamart, D., and Eiler, J., 2008. C-13-O-18 bonds in dissolved inorganic carbon: Implications for carbonate clumped isotope thermometry. Geochim Cosmochim Ac 72, A336−A336.

Guo, W., Mosenfelder, J. L., Goddard Iii, W. A., and Eiler, J. M., 2009. Isotopic fractionations associated with phosphoric acid digestion of carbonate minerals: Insights from first-principles theoretical modeling and clumped isotope measurements. Geochim Cosmochim Ac 73, 7203−7225.

Holcomb, M., Cohen, A. L., Gabitov, R. I., and Hutter, J. L., 2009. Compositional and morphological features of aragonite precipitated experimentally from seawater and biogenically by corals. Geochim Cosmochim Ac 73, 4166−4179.

Kim S.-T. and O'Neil J. R. (1997) Equilibrium and nonequilibrium oxygen isotope effects in synthetic carbonates. Geochim. Cosmochim.Acta 61, 3461−3475.

McConnaughey, T., 1989. 13C and 18O isotopic disequilibrium in biological carbonates: I. Patterns. Geochim Cosmochim Ac 53, 151−162.

McCrea, J. M., 1950. On the isotopic chemistry of carbonates and a paleotemperature scale. Journal of Chemical Physics 18, 849−857.

O'Leary, M. H., 1984. Measurement of the isotope fractionation associated with diffusion of carbon dioxide in aqueous solution. The Journal of Physical Chemistry 88, 823−825.

Okorokov, A. L., Panov, K. I., Kolbanovskaya, E. Y., Karpeisky, M. Y., Polyakov, K. M., Wilkinson, A. J., Dodson, G. G., and Watson, E. B., 1996. Surface enrichment and trace-element uptake

during crystal growth. Geochim Cosmochim Ac 60, 5013−5020.

Reynaud, S., Ferrier-Pagès, C., Meibom, A., Mostefaoui, S., Mortlock, R., Fairbanks, R., and Allemand, D., 2007. Light and temperature effects on Sr/Ca and Mg/Ca ratios in the scleractinian coral Acropora sp. Geochim Cosmochim Ac 71, 354−362.

Rollion-Bard, C., Chaussidon, M., and France-Lanord, C., 2003. pH control on oxygen isotopic composition of symbiotic corals. Earth Planet Sc Lett 215, 275−288.

Schauble, E. A., Ghosh, P., and Eiler, J. M., 2006. Preferential formation of 13C-18O bonds in carbonate minerals, estimated using first-principles lattice dynamics. Geochim Cosmochim Ac 70, 2510−2529.

Schrag, D. P. and DePaolo, D. J., 1993. Determination of del18O of seawater in the deep ocean during the Last Glacial Maximum. Paleoceanography 8, 1−6.

Shackleton, N. J., 1967. Oxygen isotope analyses and Pleistocene temperatures re-assessed. Nature 215, 15−17.

Tripati, A. a. T., N. and Eiler, J., 2007. Carbonate `clumped isotope' thermometry in planktonic foraminifera and coccoliths. AGU Fall Meeting Abstracts, B1263.

Urey, H. C., 1947. The thermodynamic properties of isotopic substances. J. Chem. Soc. 1947, 562−581.

Usdowski, E., Michaelis, J., Bottcher, M. E., and Hoefs, J., 1991. Factors for the oxygen isotope equilibrium fractionation between aqueous and gaseous CO2, carbonic acid, bicarbonate, carbonate, and water (19°C). Zeitschrift fur Physikalische Chemie 170, 237−249.

Watson, E. B., 2004. A conceptual model for near-surface kinetic controls on the trace-element and stable isotope composition of abiogenic calcite crystals. Geochimica et Cosmochimca Acta 68, 1473−1488.

Weber, J. N. and Woodhead, P. M. J., 1970. Carbon and oxygen isotope fractionation in the skeletal carbonate of reef-building corals. Chem Geol 6, 93−117.

Weber, J. N., 1973. Deep-sea ahermatypic scleratinian corals: isotopic composition of the skeleton. Deep-Sea Research 20, 901−909.

Zeebe, R., 1999. An explanation of the effect of seawater carbonate concentration on foraminiferal oxygen isotopes. Geochim Cosmochim Ac 63, 2001−2007.

Zeebe, R. E., Bijma, J., and Wolf-Gladrow, D. A., 1999. A diffusion-reaction model of carbon isotope fractionation in foraminifera. Marine Chemistry 64, 199−227.

Chapter 3:
Movement of Deep-Sea Coral Populations on Climatic Timescales

3.1 ABSTRACT

During the past 40,000 years global climate has moved out of a full glacial period, with the deglaciation marked by several millennial scale rapid climate change events. Here we investigate the ecological response of deep-sea coral communities to both glaciation and rapid climate change. We find that the deep-sea coral populations of *D. dianthus* in both the North Atlantic and the Southern Ocean expand at times of rapid climate change. However, during the more stable Last Glacial Maximum the coral population globally retreats to a more-restricted depth range. Holocene populations show regional patterns that provide some insight into what causes these dramatic changes in population structure. The most important factors are likely responses to climatically driven changes in productivity, $[O_2]$ and $[CO_3^{2-}]$.

3.2 INTRODUCTION

The role of the deep ocean in climate change has been a central theme of paleoceanography from the early days of the field. As the locus of nearly all the mass, thermal inertia, and carbon in the ocean-atmosphere system, the deep ocean's overturning rate is a crucial parameter in understanding past climates. Probing the distributions and rates of deep-water mass shifts during times of past climate change has largely been informed by geochemical tracers. For instance, the distribution of $\delta^{13}C$ (Curry and Lohmann 1985; Raymo, Ruddiman et al. 1990) and Cd/Ca (Boyle and Keigwin 1982; Oppo and Horowitz 2000) in the water column during glacial periods shows that the volume of southern source waters in the Atlantic increases at the expense of northern source waters. Recently, one of the most promising of these tracers has been radiocarbon as it has an internal clock intrinsic to the tracer. In the modern ocean the deficit of the $^{14}C/^{12}C$ ratio in the ocean interior, as compared to its production by cosmic rays in the atmosphere, is one measure of the ventilation rate of the deep-sea. In the past ocean combined U-series and ^{14}C ages,

and benthic minus planktonic ^{14}C ages, have been able to constrain the rate of deep ocean overturning.

However, as successful as the geochemical tracers have been, the distribution of benthic foraminifera species was actually one of the first indicators of deep ocean change (Streeter and Shackleton 1979). Streeter and Shackleton noticed that *Uvegerina peregina*, a benthic foraminifera which is correlated with the distribution of Antarctic Bottom Water (AABW), was abundant in LGM sediments that are today bathed by North Atlantic Deep Water (NADW). The authors hypothesized, correctly, that southern sourced waters replaced NADW as the dominant abyssal water mass in the LGM Atlantic and suggested that North Atlantic deep water production was much reduced. Using species distributions in space and time to constrain aspects of the physical climate was epitomized in the CLIMAP program. CLIMAP was a successful effort to map surface populations of foraminifera during the Last Glacial Maximum (LGM) and to attribute the changing populations to variations in sea surface temperature. In this paper we show how the combination of these two types of research, geochemical and faunal constraints on past ocean behavior have come together in the study of deep-sea corals in the North Atlantic and Southern Oceans. We show how coral population changes in space and time are like the deep ocean version of CLIMAP and reveal remarkable correlations with climate.

Deep-sea corals are a relatively new archive in paleoclimate. Our preferred species *Desmophyllum dianthus* is uranium rich, visually banded, and grows for decades to 100 years. Like all scleractinians it can also be precisely U-series (Cheng, Adkins et al. 2000) and radiocarbon dated (Robinson, Adkins et al. 2005) . This combination of precise, independent calendar ages frees ^{14}C from being a chronometer and allows us to measure the past ocean $\Delta^{14}C$ content as recorded in the coral skeleton. Combined with the potential for unbioturbated decadal resolution records of deep ocean change, deep-sea corals are a unique and powerful archive of past geochemical information. Previously, the use of deep-sea corals to solve problems in paleoclimate was chiefly limited by their perceived paucity on

the sea floor. However, recent work has demonstrated that several genera of deep-sea corals have a global distribution (Cairns 2007), making them ideal candidates for constraining the intermediate and deep ocean's role in climate change. A recent census of azooaxanthellar corals revealed that there are at least as many species of 'deep-sea coral' as there are surface corals (Cairns, 2007).

Since 2003 we have made a systematic effort to collect fossil deep-sea corals from two regions each near a site of modern deep-water formation. In several cruises with the deep submergence vehicle Alvin and the remotely operated vehicle (ROV) Hercules, we collected more than 5,000 fossil *D. dianthus* individuals from the New England (34–40°N, 60–68°W) and Corner Rise Seamounts (34–36°N, 47–53°W). We also collected more than 10,000 fossil *D. dianthus* samples from south of Tasmania (43–47°S, 144–152°E) in 2008 and 2009 using the ROV Jason. Collection by ROV and submarine ensures that the depth of each coral is precisely known and that corals are collected near their paleo growth position. At the time of collection we know the latitude, longitude, and depth of the coral's growth, but we have no idea about when it grew.

Unlike sediment cores where an age model can be constructed by extrapolating between dates made on foraminifera, every individual deep-sea coral sample must be dated prior to being used for paleoclimate analysis. In this work, we take advantage of a new development, the reconnaissance dating method at WHOI's accelerator mass spectrometry facility (NOSAMS), to radiocarbon date more than 500 of these *D. dianthus* samples. We construct, for the first time, the history of benthic population movements in space and time since the last glacial period. This effort is similar to an ostracod dataset from the deep North Atlantic that demonstrated that the Pliocene ostracod species diversity is related to changes in solar insolation caused by changes in Earth's obliquity (Cronin and Raymo 1997). However the combination of Reconnaissance radiocarbon dating and deep-sea corals has allowed us to rapidly and inexpensively construct an extensive dataset of a species' habitat preferences. Rather than having to work up many sediment cores across a depth range,

our search for deep-sea coral samples that grew during times of rapid climate change has produced a view into benthic ecology on long timescales. We present the largest record to date of changes in the deep-sea coral distributions in the North Atlantic and Southern Ocean for the last 40,000 years. Our sample set is large enough to capture the temporal resolution necessary to see rapid climate change events in both hemispheres. This record (Figure 3.1) provides an unprecedented view of the deep-sea ecological response to climate change. In addition, this paper's use of radiocarbon dating in an 'age screening' mode demonstrates how recent analytical advances can dramatically change the way ^{14}C dates are used in paleoclimatology and paleoecology.

3.3 METHODS AND MATERIALS

We collected more than 5000 *Desmophyllum dianthus* from the New England (34–40°N, 60–68°W) and Corner Rise Seamounts (34–36°N, 47–53°W) in 2003–2005 using the deep submergence vehicles ALVIN and HERCULES. We also collected more than 10,000 *Desmophyllum dianthus* from south of Tasmania (43–47°S, 144–152°E) in 2008 and 2009 using the deep submergence vehicle JASON. Collection by ROV and submarine ensured that the depth of each coral was precisely known and that corals were collected near growth position.

Ninety-five corals from the New England and Corner Rise Seamounts and two hundred and forty-nine corals from the Southern Ocean were selected randomly from our collection across seamounts and depths for ^{14}C analyses. There is some possibility for a size bias as whole corals rather than fragments were used.

Corals were dated using a reconnaissance dating method involving an elemental analyzer and sealed tube zinc reduction method for preparing graphite (Xu, Trumbore et al. 2007; Burke, Robinson et al. 2010). This method allowed for many more samples to be dated at a much lower cost than traditional hydrolysis methods.

3.3.i. Radiocarbon Method

Samples of 8–15 mg were taken from each coral and physically and chemically cleaned to remove the ferromanganese crust that was coating it (Adkins, Griffin et al. 2002).

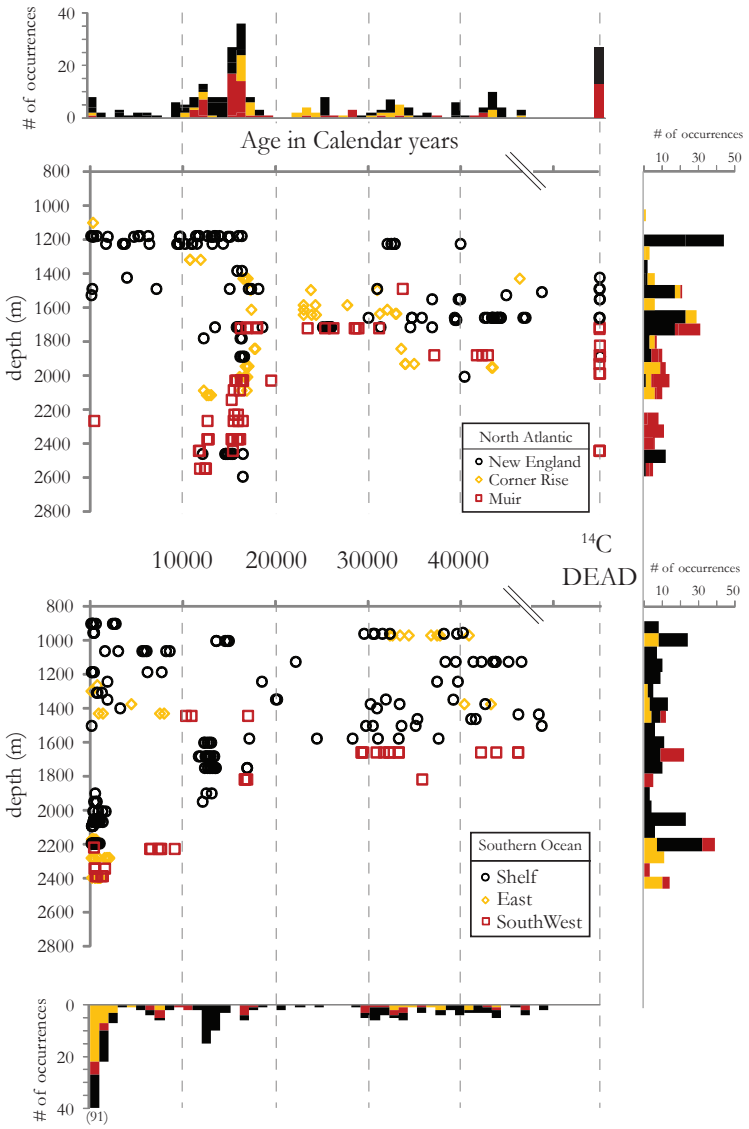

Figure 3.1: The age-depth distributions of deep-sea corals from the North Atlantic and Southern Ocean seamounts for the past 50,000 calendar years. These corals were dated using the reconnaissance dating method (and then converted to calendar age (see SOM for details) and U/Th (22). Each point represents a single age from a single *D. dianthus* coral. The histograms above and below the plots represent the number of corals for each 1000 year age bin. The histograms at the side of the plot represent the number of corals for each 75 m depth bin. Corals were collected from 1098-2740 m (while searching from 900-2800 m) in the North Atlantic and from 898-2395 m (while searching from 898-4000 m) in the Southern Ocean. The break in the age axis demonstrates that there is a population of corals that are 14C-dead in the N. Atlantic but not in the Southern Ocean.

Corals from 2009 were physically cleaned using a Dremel tool and a sandblaster and then chemically washed with MeOH which had been shown to be equivalent to the more labor intensive cleaning done in 2008 (Burke, Robinson et al. 2010). Corals were then combusted in an EA and the resulting CO_2 from combustion was extracted cryogenically on a vacuum line attached to the EA. The CO_2 was frozen into a reaction tube which contained Zinc and Titanium hydride and Fe catalyst. The sample was then graphitized in a furnace for 3 hours at 500°C and 4 hours at 550°C, and analyzed for Fm at The National Ocean Sciences Accelerator Mass Spectrometry Facility at Woods Hole Oceanographic Institute.

Coral standards were run using the traditional hydrolysis method and the reconnaissance dating method to ensure that there was no bias to the reconnaissance dating method (Figure 3.2). Coral standards were also run at regular intervals during sample processing (Figure 3.3).

We converted all radiocarbon dates to calendar ages by applying four different constant offsets during four time periods. We used the modern age of the water column in the North Atlantic (600 years) and Southern Ocean (1250 years) to make a reservoir correction for all Holocene data. We used the ^{14}C age and U/Th age difference (1500 years) as measured in corals from the New England Seamounts during the Younger Dryas to convert Younger Dryas measurements(Robinson, Adkins et al. 2005). For all other corals during the glacial time period in the North Atlantic we used the ^{14}C age and U/Th age difference (1000 years) measured in Heinrich 1 corals to make a reservoir (Robinson, Adkins et al. 2005). For all glacial corals in the Southern Ocean we used the average of the ^{14}C to U/Th age difference (1900 years) measured in the ACR (Table 3.4) to make a reservoir correction. We converted all ^{14}C dates to calendar ages using Intcal09 and the Calib 6.0 software.

After analyzing the 344 ^{14}C Reconnaissance measurements, 80 more corals were randomly selected from 1375–1575 m water depth from the Southern Ocean to improve the population statistics of intermediate water column coral distributions (Figure 3.4).

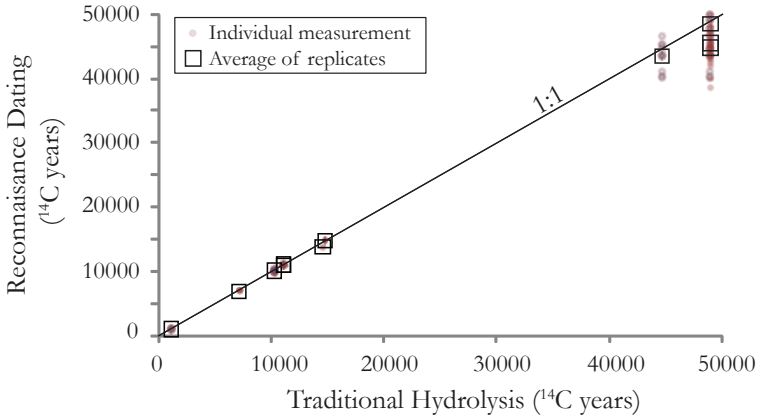

Figure 3.2: Comparison of reconnaissance dating method versus hydrolysis dating.

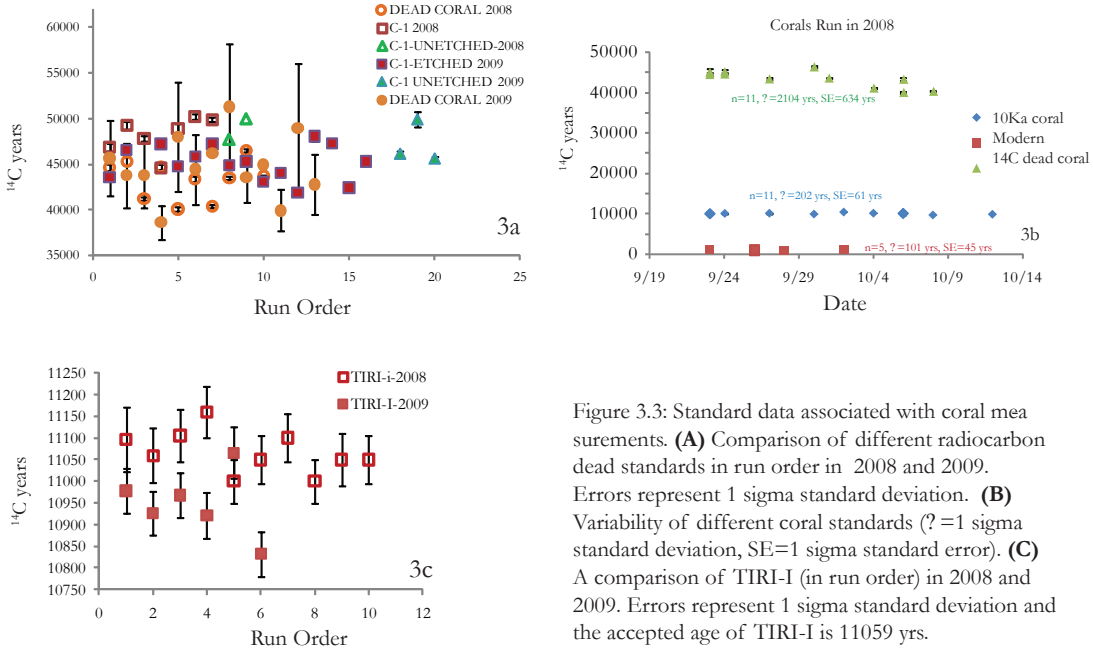

Figure 3.3: Standard data associated with coral mea surements. **(A)** Comparison of different radiocarbon dead standards in run order in 2008 and 2009. Errors represent 1 sigma standard deviation. **(B)** Variability of different coral standards (? =1 sigma standard deviation, SE=1 sigma standard error). **(C)** A comparison of TIRI-I (in run order) in 2008 and 2009. Errors represent 1 sigma standard deviation and the accepted age of TIRI-I is 11059 yrs.

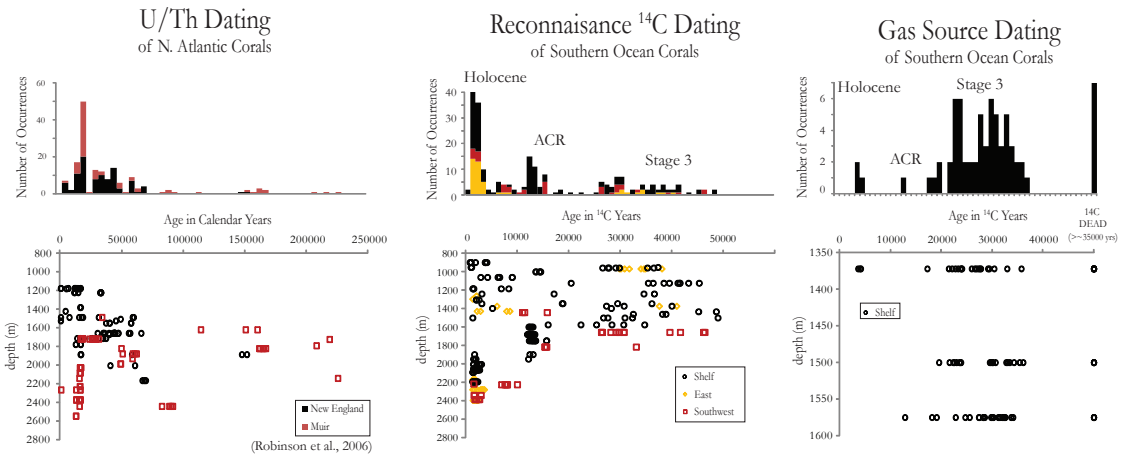

Figure 3.4: This figure describes the various methods of dating corals. The U/Th method can be used to screen corals up with an age of ~ 500,000 calendar years. This process is more labor intensive than ^{14}C dating. A ^{14}C date gives the age of the DIC from which the coral precipitated from as opposed to calendar years. Traditional hydrolysis ^{14}C dating is more time consuming and expensive; however, there are two new ^{14}C dating methods that are cheaper and faster. One is the reconnaisance ^{14}C dating method which has slightly larger error bars than the traditional method. However it is possible to prepare 30 corals in one day with this method. The second method is the gas ion source (GIS) method, where coral samples are reacted with H_3PO_4, and the resulting CO_2 is fed directly into the accelerator mass spectrometer (AMS) system. It is possible to measure 40 corals in 1 day with this method. However there is a much higher background with the GIS-AMS (~ 0.02) than with Reconnaissance Dating (~ 0.007).

These were run with another new development in ^{14}C dating, the Gas Ion Source (GIS) at NOSAMS in WHOI. In the GIS-AMS method, coral samples were reacted with H_3PO_4, and the resulting CO_2 is fed directly into the Accelerator Mass Spectrometer (AMS) system.

3.4 RESULTS

Figure 3.1 shows the depth and age distribution of corals collected from the New England, Corner Rise, Muir and Southern Ocean seamounts. Figure 3.1 also includes previously published U-series dated corals from the New England seamounts (Robinson, Adkins et al. 2005; Robinson, Adkins et al. 2006). There are several prominent features in the distribution of corals. One is that the coral population in the North Atlantic is in general older than the Southern Ocean coral population. There are several radiocarbon dead corals in the North Atlantic but no corals older than 45,000 ^{14}C years in the Southern Ocean. During the LGM, the coral populations in the North Atlantic predominate at 1850 m which roughly corresponds to the boundary between northern and southern source water as determined by $\delta^{13}C$ and Cd/Ca measurements (Oppo and Lehman 1993; Curry and Oppo 2005; Marchitto and Broecker 2006). Although the data are sparse, a similar boundary appears in the Southern Ocean. During the glacial time period in the North Atlantic, the bottom most extent of the coral distribution remains constant at 1850 m. Similarly in the Southern Ocean there is a nearly constant depth limit of 1650 m until 18,500 ^{14}C years, after which the population bifurcates in depth.

The coral populations both in the North Atlantic and Southern Ocean respond to rapid climate changes (Dansgaard, Johnsen et al. 1993; Blunier and Brook 2001). From sediment and ice core records we know that the YD and H1 events were both times of large reorganization of the atmospheric and ocean system. These are also times when the size and the depth range of the coral population increased in the North Atlantic (Figure 3.5). Interestingly the coral populations also expanded during the LIA in the North Atlantic (Figure 3.1, Figure 3.6), after a long period of coral growth only at the shallowest depths. In contrast to the New England seamount record, the Southern Ocean coral distribution has

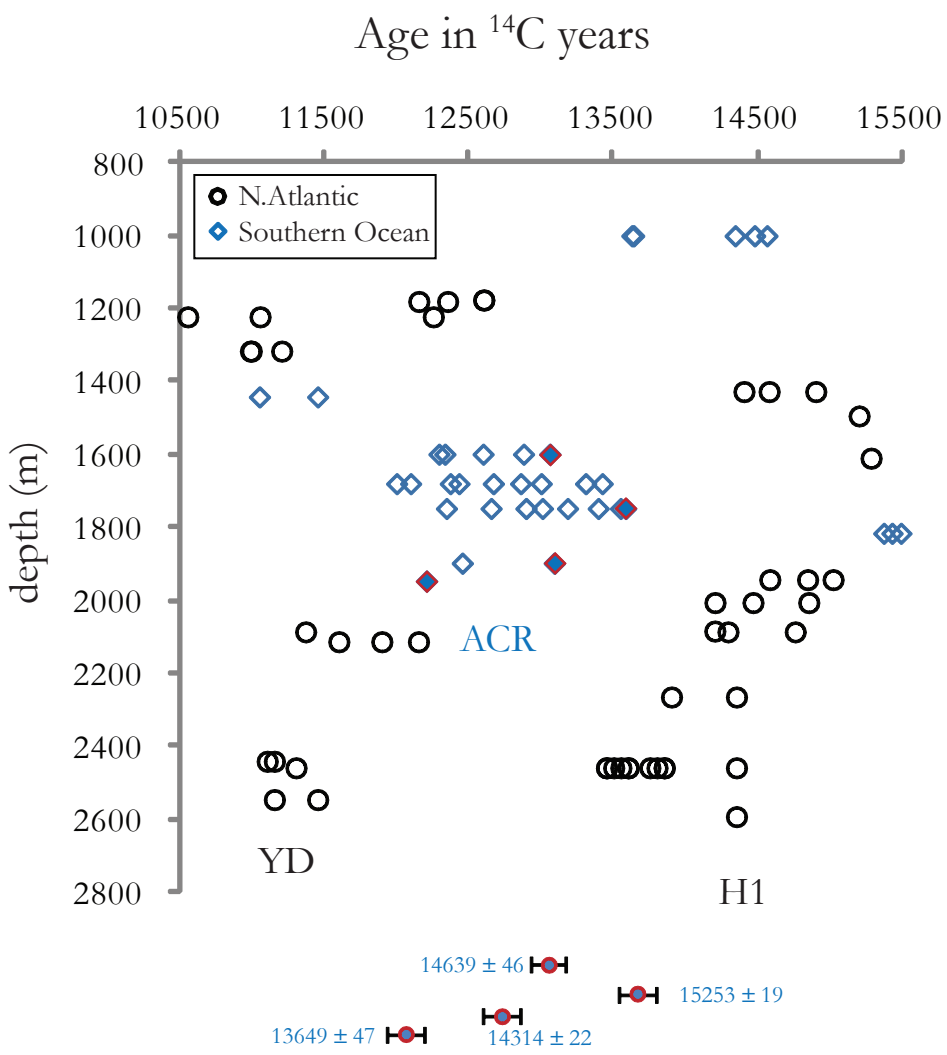

Figure 3.5: The ^{14}C age-depth distribution of deep-sea corals dated using the Reconnaissance dating method during the last deglaciation. The coral depth distribution is sharply modal during the three rapid climate changes in the deglaciation, the Younger Dryas (YD), Antarctic Cold Reversal (ACR) and Heinrich 1 (H1). Calendar ages and the associated error bars for selected ACR corals (diamonds outlined in red) are indicated at the bottom. Calendar ages for H1 and YD corals have been previously determined (36-37) and do not overlap with the ACR mode.

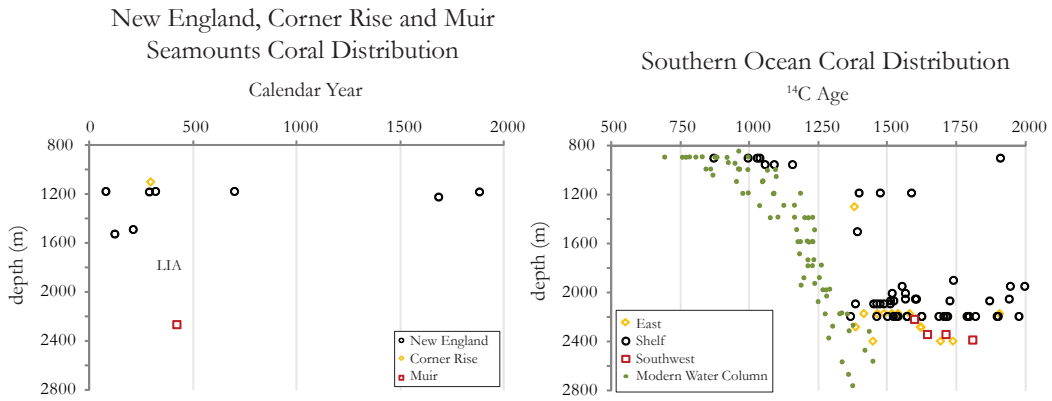

Figure 3.6: The age and depth distribution of deep-sea corals in the Late Holocene. The green diamonds represents the age of the modern water column profile. Most of the deep-sea community in the Southern Ocean is modern in radiocarbon age, while there is a mode in the deep-sea coral community in the New England sea mounts that is ~400 years old, and corresponds to the Little Ice Age (LIA).

only one deglacial mode, the Antarctic Cold Reversal (ACR). This Southern Ocean mode is different in both ^{14}C and U/Th ages (Figure 3.5, Table 3.4). As radiocarbon dates in the deep ocean, and especially in the Southern Ocean, have a large 'reservoir age', it is not possible to say with ^{14}C dates alone if the coral populations in Figure 3.2 are truly separate from one another. To check these results we selected four samples from the ACR mode in Figure 1 for U-series dating. The results are shown at the bottom of Figure 3.5. This cluster of calendar ages clearly predates that age of the start of the Younger Dryas and post-date the calendar ages of North Atlantic corals from the Heinrich Stadial interval (11). Our data show that deep ocean populations respond dramatically to local climate switches and that the populations in the North Atlantic and the Southern Ocean expanded at separate times during the last deglaciation.

In Figure 3.4 we explore the value of three different dating methods, U-series, reconnaissance ^{14}C dating and the gas ion source (GIS) method. The corals selected for analysis on the GIS-AMS were collected between 1350–1575 m of water depth. With this high frequency sampling we observe the minimum depth of the ACR to be 1575 m as corals do not appear in shallower depths. Also unlike the depth distribution of corals from the entire water column in the Southern Ocean, the depth distribution of corals at intermediate depths prefers Stage 3 relative to the Holocene. The Holocene mode is more strongly seen deeper in the water column (1800–2400 m). In the intermediate water column depths, there are two pulses in the Stage 3 mode, possibly correlated with Heinrich 3 and Heinrich 4 (Fig 3.4). These two pulses also correlate with two pulses seen in the Southern Ocean Reconnaissance data set, and perhaps with other smaller modes seen in the North Atlantic Reconnaissance data set which correspond to the other Heinrich Events (Figure 3.4).

3.5 DISCUSSION

While the overall picture of coral population dynamics is clear from Figure 3.1, we seek a more in-depth description of these results. We use the Wilcoxon rank sum test and Brown-Forsythe test to quantitatively assess the difference in medians and variances of the

different coral population shifts in depth (Table 3.3). For any single time period we bin all the coral depths and then calculate a mean and variance of this grouping. The population between 20,000 and 30,000 years in the North Atlantic is a unique distribution in mean depth compared to other North Atlantic time intervals in the Holocene and deglaciation and unique in depth variance compared to other North Atlantic time intervals during the glacial. We interpret this as a unique depth distribution for the LGM even though the age range we picked was widened to include enough corals to be statistically meaningful. In variance tests, H1 has a different value than does the YD as more corals expanded to shallower depths in the YD. The ACR distribution is also unique compared to all other times in the Southern Ocean and the YD and H1 in the North Atlantic. To further quantify our results, a targeted selection of our Southern Ocean corals was analyzed by the Gas Ion Source-AMS (GIS-AMS). Corals collected between 1350–1550 m were chosen to test the robustness of our observations of coral distributions in time, based on the reconnaissance method. The GIS allows us to analyze even more corals in a short period of time and can therefore target specific questions related to gaps in the record. As the ACR does not appear in the corals sampled from 1372 to 1500 m in the GIS results, the minimum population depth of the ACR is 1575 m (Figure 3.4). This data set also confirms the scarcity of corals during the LGM in the Southern Ocean as more corals do not appear with this higher frequency sampling.

Given these dramatic changes in coral populations in space and time, we can speculate on the factors that could affect the distributions. One possibility is a sampling bias at the field site in which the distribution of corals collected does not reflect the distribution of corals on the ocean floor. However, the coral distribution collected from the North Atlantic does not correlate with the amount of time spent looking for corals at each depth, making such a bias unlikely (Robinson, Adkins et al. 2007). Skeletal dissolution cannot explain all the diversity patterns because there are several cases where older corals survived multiple younger gaps in the population distribution at their depth. We believe that the

bottom of the ocean was randomly sampled during our dives and that our coral collection was essentially randomly sampled back on shore when we selected samples for ^{14}C dating (see Methods).

The modern distribution in the Southern Ocean has a distinctive gap between 1575–1825m that could help elucidate the factors controlling population depth preferences. It is unlikely that either a single water mass or dissolved nutrient supply is the dominant control on coral distribution because the gap does not correspond to the minimum in the salinity profile or the maximum in the phosphate or nitrate profile. Temperature is decreasing monotonically through the depth profile and is therefore not likely to be the single factor in determining coral growth in the modern. However it is possible that temperature is not low enough to be a limiting factor on coral growth at these depths and could be an important factor during other time periods. The gap does correspond to the oxygen minimum zone (OMZ) of 165 μmol/kg and the $[CO_3^{2-}]$ minimum of 110 μM in profiles from near our sampling sites (Figure 3.7). Recent work on another cosmopolitan deep-sea coral, *Lophelia pertusa*, has shown that the respiration rate of this species markedly declines at an oxygen concentration of approximately ~ 100–150 μmol/kg, depending on the growth temperature (Lawrence, Liu et al. 2006). This is a nice correspondence between lab based metabolic limits and our field based gap in the coral population. A temporary extinction of cold-water corals has also been seen from 11.4–5.9 cal kyr BP in the eastern Mediterranean (Fink, Wienberg et al. 2012). From 1400–2400 m the aragonite saturation state of the water column remains relatively constant at $\Omega \sim 0.9$, but below this depth it begins to decrease much more rapidly corresponding to the bottom-most extent of the coral distribution. So, below the oxygen minimum zone, oxygen concentrations increase and the coral populations again begin to thrive, despite low $[CO_3^{2-}]$. This suggests that the gap in coral distribution at this site is a function of declining coral respiration rate and that the bottom-most extent of the coral distribution, similar to the distribution of living *D. dianthus*, is a function of the aragonite saturation state of the water column.

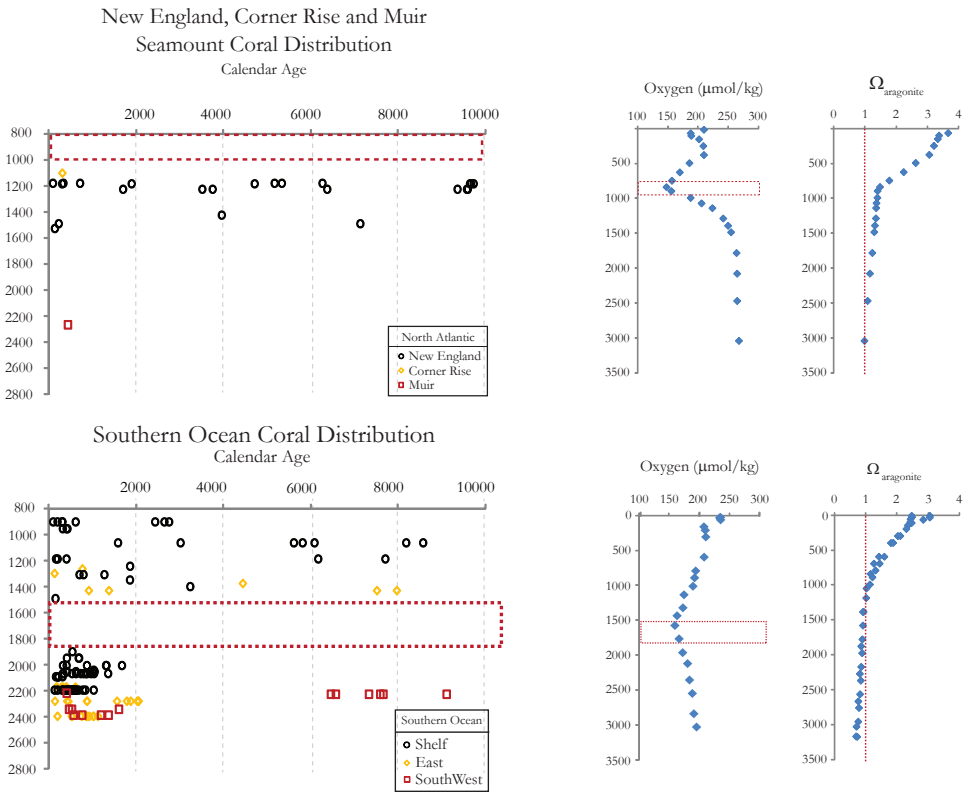

Figure 3. 7: The age-depth distributions of Holocene deep-sea corals. These corals were dated using the reconnaissance dating method (and then converted to calendar ages) and the U/Th method (19). The dashed red boxes represent gaps in the coral distribution which also correspond to the oxygen minimum zones. The dashed red lines on the $\Omega_{aragonite}$ profile represent the division between undersaturated and supersaturated water column conditions for aragonite precipitation.

Deep-sea corals are sessile filter feeders, so it is likely that surface ocean productivity is another important factor in controlling coral growth. Annual and decadal time-series studies in the modern ocean show that deep-sea biota can experience rapid changes due to variations in surface ocean productivity (Robinson and Sigman 2008; Benway, McManus et al. 2010). On longer timescales, previous work (Manighetti, McCave et al. 1995), has shown a relationship between changes in coral distributions and productivity that was attributed to changes in the location of the polar front. When all the population studies published to date are considered along with our current data set, we see a similar pattern. During the Holocene, there are abundant corals in the upper water column of the New England Seamounts, in the Rockall Trough and Porcupine Seabight regions near Iceland (Barnosky, Koch et al. 2004), and in the Sula Reef complex on the Norwegian Shelf (Marcus 1984). All of these regions are located in the subpolar gyre, or at the northern edge of the Gulf Stream and are regions of relatively high productivity. But there are few to rare occurrences of modern and Holocene deep-sea corals in the Corner Rise or the Gulf of Cadiz (Wienberg, Hebbeln et al. 2009) which are low productivity regions south of the Gulf Stream and in the subtropical gyre. In contrast, during the last glacial, atmospheric and oceanic circulation are thought to be more zonal perhaps indicating that the subpolar gyre itself was more zonally oriented. At this time there were corals in the New England and Corner Rise seamounts, as well as the Gulf of Cadiz, but none in the Rockall Trough, Porcupine Seabight or the Sula Reef complex. These latter three were north of the IRD belt and likely under sea ice with less surface productivity to fuel coral growth. In the Southern hemisphere, on the other hand, the ACR population mode does not spread across all depths as one would predict based on productivity control alone. So while surface productivity is a factor influencing coral growth in general, it cannot be the only factor in the area south of Tasmania.

This ecological dataset also has implications for our interpretation of past ocean conditions. Since the LGM, the Southern Ocean corals have increased in maximum depth. This could be due to a deepening of the aragonite saturation horizon. If the bottom-

most extent of the coral distribution during the LGM is controlled by [CO_3^{2-}] under saturation (where $\Omega < 0.9$) and not [O_2] (as there was more oxygen in the water column due to increased solubility with cooler temperatures), then the [CO_3^{2-}] at the base of the distribution during the LGM should be similar to that of the base of the modern except for temperature and pressure differences. Therefore, assuming that during the LGM, sea level is 125 m lower, the temperature is 2°C cooler (Cutler, Edwards et al. 2003), and there is a salinity increase of 3.3% (Adkins, McIntyre et al. 2002), we calculate that the [CO_3^{2-}] at 1575 m during the LGM was ~ 85 μM. This estimate for [CO_3^{2-}] during the LGM agrees with an estimate based on foraminifer dissolution rates (Sanyal, Hemming et al. 1995; Broecker 1998).

References:

Adkins, J.F., Griffin, S., Kashgarian, M., Cheng, H., Druffel, E.R.M., Boyle, E.A., Edwards, R.L., Shen, C.-C., 2002a. Radiocarbon dating of deep-sea corals. Radiocarbon 44, 567–580.

Adkins, J.F., McIntyre, K., Schrag, D.P., 2002b. The salinity, temperature, and delta O-18 of the glacial deep ocean. Science 298, 1769–1773.

Barnosky, A.D., Koch, P.L., Feranec, R.S., Wing, S.L., Shabel, A.B., 2004. Assessing the Causes of Late Pleistocene Extinctions on the Continents. Science 306, 70–75.

Benway, H.M., McManus, J.F., Oppo, D.W., Cullen, J.L., 2010. Hydrographic changes in the eastern subpolar North Atlantic during the last deglaciation. Quaternary Sci Rev 29, 3336–3345.

Blunier, T., Brook, E., 2001. Timing of millennial-scale climate change in Antarctica and Greenland during the last glacial period. Science 291, 109–112.

Boyle, E.A., Keigwin, L.D., 1982. Deep circulation of the North Atlantic over the last 200,000 years: Geochemical evidence. Science 218, 784–787.

Broecker, W.S., 1998. Paleocean Circulation during the Last Deglaciation: A Bipolar Seesaw? Paleoceanography 13, 119–121.

Burke, A., Robinson, L.F., McNichol, A.P., Jenkins, W.J., Scanlon, K.M., Gerlach, D.S., 2010. Reconnaissance dating: A new radiocarbon method applied to assessing the temporal distribution of Southern Ocean deep-sea corals. Deep Sea Research Part I: Oceanographic Research Papers 57, 1510–1520.

Cairns, S.D., 2007. Deep-water corals: An overview with special reference to diversity and distribution of deep-water scleractinian corals. B Mar Sci 81, 311–322.

Cheng, H., Adkins, J.F., Edwards, R.L., Boyle, E.A., 2000. U-Th dating of deep-sea corals. Geochimica et Cosmochimca Acta 64, 2401–2416.

Cronin, T.M., Raymo, M.E., 1997. Orbital forcing of deep-sea benthic species diversity.

Nature 385, 624–627.

Curry, W.B., Lohmann, G.P., 1985. Carbon deposition rates and deep water residence time in the equatorial Atlantic ocean throughout the last 160,000 years, in: Sundquist, E.A., Broecker, W.S. (Eds.), The Carbon Cycle and Atmospheric CO2: Natural Variations Archean to Present. Am. Geophys. Union, Geophys. Mon. 32, pp. 285–301.

Curry, W.B., Oppo, D., 2005. Glacial Water Mass Geometry and the Distribution of d13C of Total CO2 in the Western Atlantic Ocean. Paleoceanography 20, doi:10.1029/2004PA001021.

Cutler, K.B., Edwards, R.L., Taylor, F.W., Cheng, H., Adkins, J., Gallup, C.D., Cutler, P.M., Burr, G.S., Chappell, J., Bloom, A.L., 2003. Rapid sea-level fall and deep-ocean temperature change since the last interglacial. Earth Planet Sc Lett 206, 253–271.

Dansgaard, W., Johnsen, S.J., Clausen, H.B., Dahl-Jensen, D., Gundestrup, N.S., Hammer, C.U., Hvidberg, C.S., Steffensen, J.P., Sveinbjornsdottir, A.E., Jouzel, J., Bond, G., 1993. Evidence of general instability of past climate from a 250-kyr ice-core record. Nature 364, 218–220.

Eltgroth, S.F., Adkins, J.F., Robinson, L., Southon, J., Kashgarian, M., 2006. A deep-sea coral record of North Atlantic radiocarbon through the Younger Dryas: Evidence for Intermediate/Deep water reorganization. Paleoceanography.

Fink, H.G., Wienberg, C., Hebbeln, D., McGregor, H.V., Schmiedl, G., Taviani, M., Freiwald, A., 2012. Oxygen control on Holocene cold-water coral development in the eastern Mediterranean Sea. Deep Sea Research Part I: Oceanographic Research Papers 62, 89-96.

Lawrence, K.T., Liu, Z., Herbert, T.D., 2006. Evolution of the Eastern Tropical Pacific Through Plio-Pleistocene Glaciation. Science 312, 79–83.

Manighetti, B., McCave, I.N., Maslin, M., Shackleton, N.J., 1995. Chronology for Climate Change: Developing Age Models for the Biogeochemical Ocean Flux Study Cores. Paleoceanography 10, 513–525.

Marchitto, T.M., Broecker, W., 2006. Deep water mass geometry in the glacial Atlantic Ocean: A review of constraints from the paleonutrient proxy Cd/Ca. Geochem Geophy Geosy 7, doi:10.1029/2006GC001323.

Marcus, L.a.B., R, 1984. The significance of Radiocarbon Dates for Rancho La Brea, in: Martin, P.a.K., R (Ed.), Quaternary Extinctions. University of Arizona Press, Tucson, Arizona.

Oppo, D., Horowitz, M., 2000. Glacial deep water geometry: South Atlantic benthic foraminiferal Cd/Ca and delta C-13 evidence. Paleoceanography 15, 147–160.

Oppo, D.W., Lehman, S.J., 1993. Mid-depth circulation of the subpolar North Atlantic during the last glacial maximum. Science 259, 1148–1152.

Raymo, M.E., Ruddiman, W.F., Shackleton, N.J., Oppo, D.W., 1990. Evolution of Atlantic-Pacific C13 gradients over the last 2.5 m.y. Earth Planet Sc Lett 97, 353–368.

Robinson, L., Adkins, J.F., Fernandez, D.P., Burnett, D.S., Wang, S.-L., Gagnon, A.C., Krakauer, N., 2006. Primary U-distribution in scleractinian corals and its implications for U-series dating. Geochem Geophy Geosy 7, doi:10.1029/2005GC001138.

Robinson, L., Adkins, J.F., Keigwin, L.D., Southon, J., Fernandez, D.P., Wang, S.-L., Scheirer, D.S., 2005a. Radiocarbon variability in the Western North Atlantic during the last deglaciation. Science 310, 1469–1473.

Robinson, L.F., Adkins, J.F., Keigwin, L.D., Southon, J., Fernandez, D.P., Wang, S.L., Scheirer, D.S., 2005b. Radiocarbon variability in the western North Atlantic during the last deglaciation. Science 310, 1469–1473.

Robinson, L.F., Adkins, J.F., Scheirer, D., Fernandez, D.P., Gagnon, A.C., Waller, R., 2007. Deep-sea scleractinian coral age and depth distributions in the NW Atlantic for the last 225 thousand years. B Mar Sci 81, 371–391.

Robinson, R.S., Sigman, D.M., 2008. Nitrogen isotopic evidence for a poleward decrease in surface nitrate within the ice age Antarctic. Quaternary Sci Rev 27, 1076–1090.

Sanyal, A., Hemming, N.G., Hanson, G.N., Broecker, W.S., 1995. Evidence for a higher pH in the glacial ocean from boron isotopes in foraminifera. Nature 373, 234–236.

Streeter, S.S., Shackleton, N.J., 1979. Paleocirculation of the deep North Atlantic: 150,000-year record of benthic foraminifera and oxygen-18. Science 203, 168–171.

Thiagarajan, N.G., D. S.; Roberts, M.; McNichol, A. P.; Thresher, R.; Adkins, J. F., 2009. Radiocarbon Age Variability of Deep Sea Corals from the North Atlantic and the Southern Ocean, American Geophysical Union, San Francisco.

Wienberg, C., Hebbeln, D., Fink, H.G., Mienis, F., Dorschel, B., Vertino, A., Correa, M.L., Freiwald, A., 2009. Scleractinian cold-water corals in the Gulf of Cádiz—First clues about their spatial and temporal distribution. Deep Sea Research Part I: Oceanographic Research Papers 56, 1873–1893.

Xu, X., Trumbore, S.E., Zheng, S., Southon, J.R., McDuffee, K.E., Luttgen, M., Liu, J.C., 2007. Modifying a sealed tube zinc reduction method for preparation of AMS graphite targets: Reducing background and attaining high precision. Nuclear Instruments and Methods in Physics Research Section B: Beam Interactions with Materials and Atoms 259, 320–329.

Table 3.1-Radiocarbon and Calendar ages for North Atlantic deep-sea corals with their unique sample name, seamount, and depth

Name	Depth	Lab Code	Seamount	Region	F Modern	Fm Error	Libby Age	Age Error	Calendar Age
RBDASS05-H05_0818-1926-103-001-1098	1098	UBA06	VERRILL	Corner Rise	0.9003	0.0044	845	40	291
RBDASS05-H05_0818-1450-101-004-1316	1316	UBA04	VERRILL	Corner Rise	0.2485	0.0017	11200	55	11902
RBDASS05-H07-0821-0513-112-007-1929	1929	NTWH2-A01	GOODE	Corner Rise	0.0226	0.0017	30441	614	33940
RBDASS05-H07-0821-0513-112-013-1929	1929	NTWH2-A03	GOODE	Corner Rise	0.0203	0.0017	31325	689	34931
RBDASS05-H07-0821-0513-112-008-1929	1929	NTWH2-A10	GOODE	Corner Rise	0.0224	0.0017	30503	618	33994
RBDASS05-H09-0823-0225-216-022-1610	1610	NTWH2-B10	KUK	Corner Rise	0.1492	0.0017	15283	89	17371
RBDASS05-h09-0822-1800-201-001-1840	1840	NTWH2-B11	KUK	Corner Rise	0.0239	0.0017	29997	578	33534
RBDASS05-h09-0822-1800-201-002-1840	1840	NTWH2-B13	KUK	Corner Rise	0.1445	0.0017	15541	92	17697
RBDASS05-h09-0823-0349-217-012-1494	1494	NTWH2-B15	KUK	Corner Rise	0.0741	0.0017	20906	183	23783
RBDASS05-h09-0823-0349-217-007-1494	1494	NTWH2-B19	KUK	Corner Rise	0.1507	0.0017	15200	89	17281
RBDASS05-h09-0823-0349-217-009-1494	1494	ntwh2-b20	KUK	Corner Rise	0.0332	0.0015	27346	351	30945
RBDASS05-h09-0823-0225-216-006-1610	1610	ntwh2-b22	KUK	Corner Rise	0.0797	0.0014	20316	142	23013
RBDASS05-h09-0823-0225-216-002-1610	1610	ntwh2-b23-2	KUK	Corner Rise	0.0278	0.0014	28770	414	32031
RBDASS05-h09-0822-1800-201-003-1840	1840	NTWH2-B25	KUK	Corner Rise	0.1429	0.0018	15628	101	17796
RBDASS05-H03-0815-0156-304-001-1583	1583	NTWH2-A02	LYMAN	Corner Rise	0.0701	0.0017	21349	194	24277
RBDASS05-H03-0815-0156-304-005-1583	1583	NTWH2-A04	LYMAN	Corner Rise	0.0507	0.0017	23953	272	27718
RBDASS05-H03-0814-2151-301-003-1634	1634	NTWH2-A07	LYMAN	Corner Rise	0.0314	0.0017	27806	439	31226
RBDASS05-H03-0815-1004-314-3-003-1427	1427	NTWH2-A08	LYMAN	Corner Rise	0.0041	0.0017	44216	3450	46317
RBDASS05-h03-0815-0156-304-007-1583	1583	NTWH2-B24	LYMAN	Corner Rise	0.0799	0.0018	20302	184	22997
RBDASS05-H03-0815-1004-314-3-001-1427	1427	NTWH2-H48	LYMAN	Corner Rise	0.1565	0.0018	14899	90	16974
RBDASS05-H03-0815-1004-314-3-002-1427	1427	NTWH2-H49	LYMAN	Corner Rise	0.1629	0.0018	14576	88	16734
RBDASS05-H03-0815-1004-314-3-002-1427	1427	NTWH2-h49-2	LYMAN	Corner Rise	0.1665	0.0026	14402	125	16492
RBDASS05-H03-0814-2151-301-007-1634	1634	NTWH2-H50	LYMAN	Corner Rise	0.0253	0.0014	29534	454	32914
RBDASS05-H03-0814-2151-301-011-1634	1634	NTWH2-H51	LYMAN	Corner Rise	0.0251	0.0014	29600	457	33013
ALV-4162-1916-008-033-1943	1943	NTWH2-B08	PICKETT	Corner Rise	0.1542	0.0018	15019	91	17074
ALV-4162-1628-003-014-2006	2006	NTWH2-B09	PICKETT	Corner Rise	0.1574	0.0017	14851	86	16939
ALV-4162-1916-008-009-1943	1943	NTWH2-B12	PICKETT	Corner Rise	0.1576	0.0018	14843	94	16935
ALV-4162-1457-001-003-2086	2086	NTWH2-B14	PICKETT	Corner Rise	0.2429	0.0018	11366	60	12236
ALV-4162-1457-001-004-2086	2086	NTWH2-B16	PICKETT	Corner Rise	0.1688	0.0016	14291	78	16315
ALV-4162-1628-003-034-2006	2006	NTWH2-B17	PICKETT	Corner Rise	0.1652	0.0016	14465	80	16634
ALV-4162-1628-003-024-2006	2006	NTWH2-B18	PICKETT	Corner Rise	0.1707	0.0019	14201	89	16092
ALV-4162-1916-008-030-1943	1943	NTWH2-B21	PICKETT	Corner Rise	0.1628	0.0020	14581	99	16733
ALV-4162-1457-001-002-2086	2086	NTWH2-B26	PICKETT	Corner Rise	0.1593	0.0018	14757	90	16876
RBDASS05-H06-0819-1631-210-5-012-1640	1640	NTWH2-A05	VERRILL	Corner Rise	0.0696	0.0017	21406	195	24349
RBDASS05-H06-0819-1019-205-001-1950	1950	NTWH2-A06	VERRILL	Corner Rise	0.0067	0.0018	40251	2168	43407
RBDASS05-H05-0818-1450-101-003-1316	1316	NTWH2-A09	VERRILL	Corner Rise	0.2546	0.0016	10989	51	10760
RBDASS05-H06-0819-0534-201-5-001-2113	2113	NTWH2-B01	VERRILL	Corner Rise	0.2204	0.0016	12148	60	13028
RBDASS05-H06-0819-0534-201-5-007-2113	2113	NTWH2-B02	VERRILL	Corner Rise	0.2275	0.0019	11894	65	12768
RBDASS05-H06-0819-1019-205-017-1950	1950	NTWH2-B03	VERRILL	Corner Rise	0.0068	0.0017	40060	2041	43271
RBDASS05-H06-0819-0534-201-5-004-2113	2113	NTWH2-B04-2	VERRILL	Corner Rise	0.2361	0.0016	11596	56	12553
RBDASS05-H06-0819-1019-205-012-1950	1950	NTWH2-B05	VERRILL	Corner Rise	0.0067	0.0017	40189	2078	43367
RBDASS05-H06-0819-1631-210-5-020-1640	1640	NTWH2-B06	VERRILL	Corner Rise	0.0735	0.0017	20974	187	23865
RBDASS05-H06-0819-1631-210-5-019-1640	1640	NTWH2-B07	VERRILL	Corner Rise	0.0799	0.0017	20303	170	22998
RBDASS05-H05-0818-1450-101-001-1316	1316	UBA01	VERRILL	Corner Rise	0.2548	0.0014	10984	45	10742
ALV-3887-1436-003-020	2441	UBA11	Muir	Muir	0.2510	0.0016	11100	55	11698
ALV-3887-1436-003-017	2441	UBA08	Muir	Muir	0.2499	0.0018	11150	60	11816
ALV-3887-1324-002-001	2546	UBB02	Muir	Muir	0.2503	0.0018	11150	55	11820
ALV-3887-1324-002-006	2546	UBA18	Muir	Muir	0.2400	0.0019	11450	60	12356
ALV-3887-1652-005-B8	2265	UAN08	Muir	Muir	0.1773	0.0020	13900	90	15444
ALV-3884-1638-004-154	2084	UAK17	Muir	Muir	0.1712	0.0018	14200	85	16093
ALV-3887-1652-005-B2	2265	UAN07	Muir	Muir	0.1681	0.0019	14350	90	16447
ALV-3885-1239-001-010	2027	UAH19	Muir	Muir	0.1150	0.0018	17350	130	19506
ALV-3885-1452-004-027	1878	UAN02	Muir	Muir	0.0156	0.0020	33400	1000	37096
ALV-3885-1452-004-028	1878	UAN05	Muir	Muir	0.0088	0.0020	38100	1800	41686
ALV-3885-1452-004-025	1878	UAN03	Muir	Muir	0.0080	0.0020	38800	2000	42258
ALV-3885-1452-004-026	1878	UAN04	Muir	Muir	0.0072	0.0020	39600	2200	42886
ALV-3889-1353-003-002	1714	UAM02	Muir	Muir	0.0027	0.0020	60000	6000	60000
ALV-3887-1436-003-021	2441	UBA12	Muir	Muir	0.0023	0.0020	60000	6900	60000
ALV-3887-1436-003-022	2441	UBA13	Muir	Muir	0.0018	0.0020	60000	8800	60000
ALV-3887-1436-003-002	2441	UBA19	Muir	Muir	0.0032	0.0020	60000	5000	60000
ALV-3889-1326-002-001	1723	UAM03	Muir	Muir	Indistinguishable from background	0.0000	60000		60000
ALV-3891-1646-004-005	1180	UAJ10	Gregg	New Eng	0.9019	0.0024	830	20	285
ALV-3891-1459-003-012	1176	UAM14	Gregg	New Eng	0.8434	0.0025	1370	25	696
ALV-3891-1758-006-004	1222	UAM13	Gregg	New Eng	0.7447	0.0027	2370	30	1682
ALV-3891-1646-004-B1	1180	UBA02	Gregg	New Eng	0.7295	0.0027	2530	30	1879
ALV-3891-1758-006-011	1222	UBB07	Gregg	New Eng	0.6179	0.0016	3870	20	3499
ALV-3891-1758-006-012	1222	UBB08	Gregg	New Eng	0.6032	0.0022	4060	30	3734
ALV-3891-1459-003-008	1176	UAM19	Gregg	New Eng	0.5277	0.0016	5130	25	5154
ALV-3891-1459-003-008	1176	UAM19	Gregg	New Eng	0.5234	0.0015	5200	25	5321
ALV-3891-1758-006-002	1222	UAM18	Gregg	New Eng	0.4625	0.0016	6190	25	6361
ALV-3891-1758-006-010	1222	UBB06	Gregg	New Eng	0.3285	0.0030	8940	75	9347
ALV-3891-1758-006-010	1222	UBB06	Gregg	New Eng	0.3173	0.0018	9220	45	9582
ALV-3891-1646-004-002	1180	UAO05	Gregg	New Eng	0.3150	0.0020	9280	50	9633
ALV-3891-1646-004-006	1180	UAO04	Gregg	New Eng	0.3138	0.0016	9310	40	9656

ALV-3891-1646-004-002	1180	UAO05	Gregg	New Eng	0.3128	0.0017	9340	45	9717
ALV-3891-1758-006-009	1222	UBB05	Gregg	New Eng	0.2838	0.0018	10100	50	9562
ALV-3891-1725-005-B2	1222	UBB10	Gregg	New Eng	0.2695	0.0017	10550	50	10219
ALV-3891-1758-006-001	1222	UAM20	Gregg	New Eng	0.2529	0.0017	11050	55	10915
RBDASS05-H15_0831-2045-605-053-2459	2459	UCA06	Kelvin	New Eng	0.2448	0.0018	11300	60	12103
ALV-3891-1646-004-001	1180	UAO01	Gregg	New Eng	0.2201	0.0017	12150	65	13030
ALV-3891-1725-005-006	1222	UAN10	Gregg	New Eng	0.2177	0.0018	12250	65	13158
ALV-3891-1646-004-007	1180	UAN11	Gregg	New Eng	0.2145	0.0021	12350	75	13231
ALV-3891-1459-003-018	1176	UAN06	Gregg	New Eng	0.2090	0.0017	12600	65	13440
ALV-3891-1459-003-018	1176	UAN06	Gregg	New Eng	0.2090	0.0017	12600	65	13440
RBDASS05-H15_0831-2045-605-003-2459	2459	UCA03	Kelvin	New Eng	0.1870	0.0017	13450	75	14554
RBDASS05-H15_0831-2045-605-035-2459	2459	UCB17	Kelvin	New Eng	0.1876	0.0017	13450	75	14554
RBDASS05-H15_0831-2045-605-034-2459	2459	UCB16	Kelvin	New Eng	0.1866	0.0018	13500	75	14646
RBDASS05-H15_0831-2045-605-036-2459	2459	UCB18	Kelvin	New Eng	0.1849	0.0017	13550	75	14736
RBDASS05-H15_0831-2045-605-013-2459	2459	UBB20	Kelvin	New Eng	0.1837	0.0018	13600	80	14837
RBDASS05-H15_0831-2045-605-033-2459	2459	UCB15	Kelvin	New Eng	0.1835	0.0019	13600	85	14830
RBDASS05-H15_0831-2045-605-008-2459	2459	UBB18	Kelvin	New Eng	0.1806	0.0017	13750	75	15130
RBDASS05-H15_0831-2045-605-037-2459	2459	UCB19	Kelvin	New Eng	0.1794	0.0017	13800	80	15230
RBDASS05-H15_0831-2045-605-001-2459	2459	UCA01	Kelvin	New Eng	0.1787	0.0019	13850	85	15351
RBDASS05-H15_0831-2045-605-007-2459	2459	UCA10	Kelvin	New Eng	0.1778	0.0019	13850	85	15351
RBDASS05-H15_0831-1616-601_3-003-2593	2593	UBB17	Kelvin	New Eng	0.1675	0.0019	14350	90	16447
RBDASS05-H15_0831-2045-605-020-2459	2459	UCA05	Kelvin	New Eng	0.1676	0.0018	14350	85	16454
ALV-3891-1725-005-009	1222	UAI08	Gregg	New Eng	0.0112	0.0020	36100	1400	39925
ALV-3890-1718-006-004	1421	UAL01	Manning	New Eng	0.0026	0.0020	60000	6200	39600

Table 3.2-Radiocarbon and Calendar ages for Southern Ocean deep-sea corals with their unique sample name, seamount, and depth

Name	Lab Code	Seamount	Region	Depth	F Modern	Fm Error	Libby Age	Age Error	Calendar Age
TN228-J2-387-1225-1253-11-1898-001	ESA01	S.HILLS	SHELF	1898	0.19605	0.00164	13089	67.1	13086
TN228-J2-387-1225-1253-11-1898-002	ESA02	S.HILLS	SHELF	1898	0.21222	0.00163	12452	61.6	12497
TN228-J2-387-1225-1253-11-1898-003	ESA03	S.HILLS	SHELF	1898	0.80539	0.00169	1739	16.9	521
TN228-J2-387-1224-2355-1-2051-001	ESC02	S.HILLS	SHELF	2051	0.78538	0.00239	1941	24.4	602
TN228-J2-387-1224-2355-1-2051-002	ESC03	S.HILLS	SHELF	2051	0.82301	0.00336	1565	32.8	387
TN228-J2-387-1224-2355-1-2051-003	ESC04	S.HILLS	SHELF	2051	0.81887	0.00379	1605	37.2	399
TN228-J2-395-0113-0902-01-2193-001	ESC07	S.HILLS	SHELF	2193	0.82967	0.00183	1500	17.7	291
TN228-J2-395-0113-0902-01-2193-002	ESC08	S.HILLS	SHELF	2193	0.78948	0.00167	1899	17.0	589
TN228-J2-395-0113-0902-01-2193-003	ESC09	S.HILLS	SHELF	2193	0.76736	0.00164	2127	17.1	763
TN228-J2-395-0113-0902-01-2193-003	ESC09	S.HILLS	SHELF	2193	0.76518	0.00293	2150	30.7	818
TN228-J2-395-0113-0902-01-2193-004	ESD01	S.HILLS	SHELF	2193	0.80801	0.00236	1713	23.4	513
TN228-J2-395-0113-0902-01-2193-006	ESD02	S.HILLS	SHELF	2193	0.82753	0.00221	1521	21.4	306
TN228-J2-395-0113-0902-01-2193-006	ESD02	S.HILLS	SHELF	2193	0.82640	0.00175	1532	17.0	308
TN228-J2-395-0113-1830-5-1947-002	ESD03	S.HILLS	SHELF	1947	0.77987	0.00182	1997	18.7	674
TN228-J2-395-0113-1830-5-1947-003	ESD04	S.HILLS	SHELF	1947	0.21889	0.00164	12204	60.2	12112
TN228-J2-395-0113-1830-5-1947-004	ESD05	S.HILLS	SHELF	1947	0.82418	0.00172	1553	16.8	394
TN228-J2-395-0113-1830-5-1947-005	ESD07	S.HILLS	SHELF	1947	0.78491	0.00167	1945	17.1	664
TN228-J2-387-1225-0147-02-2066-02	ESD08	S.HILLS	SHELF	2066	0.71311	0.00157	2716	17.7	1340
TN228-J2-387-1225-0147-02-2066-03	ESD09	S.HILLS	SHELF	2066	0.77207	0.00182	2078	19.0	714
TN228-J2-387-1225-0147-02-2066-04	ESD10	S.HILLS	SHELF	2066	0.74696	0.00196	2344	21.1	947
TN228-J2-387-1225-0147-02-2066-05	ESD11	S.HILLS	SHELF	2066	0.76190	0.00183	2184	19.3	855
TN228-J2-387-1225-0147-02-2066-06	ESD12	S.HILLS	SHELF	2066	0.82725	0.00261	1523	25.4	314
TN228-J2-387-1226-1148-20-1680-001	ESE01	S.HILLS	SHELF	1680	0.21442	0.00162	12369	60.6	12407
TN228-J2-387-1226-1148-20-1680-002	ESE02	S.HILLS	SHELF	1680	0.18812	0.00165	13421	70.4	13369
TN228-J2-387-1226-1148-20-1680-003	ESE03	S.HILLS	SHELF	1680	0.19082	0.00166	13306	69.8	13276
TN228-J2-387-1226-1148-20-1680-004	ESE04	S.HILLS	SHELF	1680	0.21284	0.00168	12429	63.5	12476
TN228-J2-392-0110-1409-08-2225-03	ESE06	FINGER	SOUTHWEST	2225	0.36652	0.00148	8063	32.4	7578
TN228-J2-384-1218-0950-02-0952-03	ESF05	S.HILLS	SHELF	952	0.87666	0.00183	1057	16.8	300
TN228-J2-384-1218-0950-02-0952-01	ESF06	S.HILLS	SHELF	952	0.00959	0.00188	37332	1573.4	40179
TN228-J2-384-1218-0950-02-0952-04	ESF07	S.HILLS	SHELF	952	0.86596	0.00238	1156	22.1	407
TN228-J2-384-1218-0950-02-0952-06	ESG02	S.HILLS	SHELF	952	0.87315	0.00262	1090	24.1	388
TN228-J2-386-1223-1345-011-0899-001	ESG03	S.HILLS	SHELF	899	0.59844	0.00195	4124	26.1	2737
TN228-J2-386-1223-1345-011-0899-002	ESH01	S.HILLS	SHELF	899	0.62055	0.00254	3833	32.9	2629
TN228-J2-386-1223-1345-011-0899-004	ESH03	S.HILLS	SHELF	899	0.78853	0.00222	1909	22.7	596
TN228-J2-386-1223-1345-011-0899-008	ESH04	S.HILLS	SHELF	899	0.62354	0.00235	3794	30.3	2417
TN228-J2-386-1223-1345-011-0899-009	ESH05	S.HILLS	SHELF	899	0.88352	0.00302	995	27.5	179
TN228-J2-386-1223-0739-07-0958-001	ESH06	S.HILLS	SHELF	958	0.03656	0.00150	26580	329.6	29528
TN228-J2-386-1223-0739-07-0958-003	ESH07	S.HILLS	SHELF	958	0.03210	0.00193	27625	482.1	30485
TN228-J2-386-1223-0739-07-0958-003	ESH07	S.HILLS	SHELF	958	0.03139	0.00146	27804	374.0	30660
TN228-J2-386-1223-0739-07-0958-005	ESH08	S.HILLS	SHELF	958	0.02436	0.00188	29841	618.5	32310
TN228-J2-386-1223-0739-07-0958-005	ESH08-2	S.HILLS	SHELF	958	0.01063	0.00144	36506	1088.3	39550
TN228-J2-386-1223-0739-07-0958-008	ESI01	S.HILLS	SHELF	958	0.01237	0.00145	35287	940.4	38130
TN228-J2-386-1223-0739-07-0958-009	ESI02	S.HILLS	SHELF	958	0.02666	0.00143	29116	432.4	31506
TN228-J2-386-1223-0515-04-1000-001	ESI03	S.HILLS	SHELF	1000	0.16319	0.00213	14562	105.0	14945
TN228-J2-386-1223-0515-04-1000-002	ESI04	S.HILLS	SHELF	1000	0.16773	0.00169	14342	81.1	14541
TN228-J2-386-1223-0515-04-1000-003	ESJ01	S.HILLS	SHELF	1000	0.18334	0.00140	13627	61.5	13576
TN228-J2-386-1223-0515-04-1000-007	ESJ02	S.HILLS	SHELF	1000	0.16495	0.00174	14476	84.5	14779
TN228-J2-386-1223-0515-04-1000-008	ESJ03	S.HILLS	SHELF	1000	0.18308	0.00156	13639	68.5	13588
TN228-J2-390-0104-0815-968-002	ESJ04	CASCADE	EAST	968	0.02155	0.00190	30824	709.0	33402
TN228-J2-390-0104-0815-968-006	ESJ05	CASCADE	EAST	968	0.02434	0.00188	29846	620.2	32315
TN228-J2-390-0104-0815-968-007	ESJ06	CASCADE	EAST	968	0.01304	0.00188	34860	1160.1	37719
TN228-J2-390-0104-0815-968-008	ESJ07	CASCADE	EAST	968	0.01922	0.00145	31746	606.8	34351
TN228-J2-390-0104-0815-968-009	ESJ08	CASCADE	EAST	968	0.01349	0.00143	34586	853.2	37404
TN228-J2-389-0101-0330-01-1428-001	ESJ09	EAST OF ST. HELENS	EAST	1428	0.69753	0.00228	2894	26.3	1360
TN228-J2-389-0101-0330-01-1428-002	ESJ10	EAST OF ST. HELENS	EAST	1428	0.75726	0.00249	2234	26.4	898
TN228-J2-389-0101-0330-01-1428-007	ESK01	EAST OF ST. HELENS	EAST	1428	0.37144	0.00160	7956	34.6	7501
TN228-J2-389-0101-0330-01-1428-010	ESK02	EAST OF ST. HELENS	EAST	1428	0.34257	0.00163	8605	38.1	7957
TN228-J2-395-0114-0057-09-1500-004	ESK03	S.HILLS	SHELF	1500	0.03220	0.00191	27601	476.8	30467
TN228-J2-395-0114-0057-09-1500-004	ESK03-2	S.HILLS	SHELF	1500	0.03578	0.00191	26753	428.5	29720
TN228-J2-395-0114-0057-09-1500-05	ESK04	S.HILLS	SHELF	1500	0.02136	0.00143	30896	538.2	33553
TN228-J2-395-0114-0057-09-1500-07	ESK05	S.HILLS	SHELF	1500	0.00226	0.00144	48939	5120.4	48684
TN228-J2-395-0114-0057-09-1500-09	ESK06	S.HILLS	SHELF	1500	0.01780	0.00143	32360	645.9	35085
TN228-J2-387-1225-0318-3-2040-001	ESK07	S.HILLS	SHELF	2040	0.74464	0.00225	2369	24.3	1010
TN228-J2-383-1217-1611-07-1397-001	ESL01-2	S.HILLS	SHELF	1397	0.02965	0.00187	28263	507.1	30914
TN228-J2-383-1217-1611-07-1397-003	ESL02	S.HILLS	SHELF	1397	0.52294	0.00204	5208	31.4	3222
TN228-J2-395-0114-0555-17-1345-005	ESM01	S.HILLS	SHELF	1345	0.02548	0.00143	29479	450.7	31869
TN228-J2-395-0114-0555-17-1345-009	ESM02	S.HILLS	SHELF	1345	0.09707	0.00145	18736	120.0	20001
TN228-J2-395-0114-0555-17-1345-010	ESM03	S.HILLS	SHELF	1345	0.09542	0.00141	18873	118.6	20155
TN228-J2-385-1221-0558-05-1060-001	NTWH2-C01	S.HILLS	SHELF	1060	0.69383	0.00203	2936	23.5	1567
TN228-J2-385-1221-0558-05-1060-002	NTWH2-C02	S.HILLS	SHELF	1060	0.58837	0.00218	4261	29.7	3000
TN228-J2-385-1221-0558-05-1060-003	NTWH2-C03	S.HILLS	SHELF	1060	0.32413	0.00144	9050	35.7	8560

TN228-J2-385-1221-0558-05-1060-004	NTWH2-C04	S.HILLS	SHELF	1060	0.32504	0.00141	9028	34.9	8171
TN228-J2-385-1221-0558-05-1060-005	NTWH2-C05	S.HILLS	SHELF	1060	0.43908	0.00142	6612	25.9	6070
TN228-J2-385-1221-0229-04-1123-001	NTWH2-C06	S.HILLS	SHELF	1123	0.07828	0.00140	20464	143.6	22150
TN228-J2-385-1221-0229-04-1123-002	NTWH2-C07	S.HILLS	SHELF	1123	0.00566	0.00144	41566	2049.2	43725
TN228-J2-385-1221-0229-04-1123-003	NTWH2-C08	S.HILLS	SHELF	1123	0.00355	0.00144	45306	3251.0	46502
TN228-J2-385-1221-0229-04-1123-004	NTWH2-C09	S.HILLS	SHELF	1123	0.01081	0.00148	36367	1096.1	39404
TN228-J2-385-1221-0229-04-1123-005	NTWH2-C10	S.HILLS	SHELF	1123	0.00568	0.00174	41530	2451.9	43692
TN228-J2-385-1221-0229-04-1123-006	NTWH2-C11	S.HILLS	SHELF	1123	0.01215	0.00146	35430	968.4	38293
TN228-J2-385-1221-0229-04-1123-007	NTWH2-C12	S.HILLS	SHELF	1123	0.00730	0.00145	39518	1590.8	42196
TN228-J2-385-1221-0229-04-1123-008	NTWH2-C13	S.HILLS	SHELF	1123	0.00595	0.00144	41166	1945.4	43434
TN228-J2-385-1221-0229-04-1123-009	NTWH2-C14	S.HILLS	SHELF	1123	0.00834	0.00144	38456	1385.2	41304
TN228-J2-385-1221-0229-04-1123-010	NTWH2-C15	S.HILLS	SHELF	1123	0.00459	0.00144	43249	2517.6	45106
TN228-J2-385-1221-026-02-1184-001	NTWH2-C16	S.HILLS	SHELF	1184	0.42290	0.00167	6913	31.7	6154
TN228-J2-385-1221-026-02-1184-002	NTWH2-C17	S.HILLS	SHELF	1184	0.84033	0.00220	1397	21.1	144
TN228-J2-385-1221-026-02-1184-003	NTWH2-C18	S.HILLS	SHELF	1184	0.82068	0.00225	1587	22.1	386
TN228-J2-385-1221-026-02-1184-004	NTWH2-C19	S.HILLS	SHELF	1184	0.83240	0.00256	1474	24.7	182
TN228-J2-385-1221-026-02-1184-005	NTWH2-C20	S.HILLS	SHELF	1184	0.35250	0.00166	8376	37.9	7693
TN228-J2-385-1220-2149-01-1240-001	NTWH2-C21	S.HILLS	SHELF	1240	0.11839	0.00176	17141	119.4	18501
TN228-J2-385-1220-2149-01-1240-002	NTWH2-C22	S.HILLS	SHELF	1240	0.01351	0.00144	34579	856.4	37396
TN228-J2-385-1220-2149-01-1240-003	NTWH2-C23	S.HILLS	SHELF	1240	0.67460	0.00220	3162	26.2	1843
TN228-J2-385-1220-2149-01-1240-004	NTWH2-C24	S.HILLS	SHELF	1240	0.01050	0.00145	36605	1111.2	39642
TN228-J2-382-1216-1930-16-1305-001	NTWH2-C25	S.HILLS	SHELF	1305	0.72273	0.00213	2608	23.6	1254
TN228-J2-382-1216-1930-16-1305-002	NTWH2-C26	S.HILLS	SHELF	1305	0.77401	0.00233	2058	24.2	683
TN228-J2-382-1216-1930-16-1305-002	NTWH2-C26-2	S.HILLS	SHELF	1305	0.76735	0.00190	2127	19.9	776
TN228-J2-383-1217-1800-09-1346-001	NTWH2-C27	S.HILLS	SHELF	1346	0.67634	0.00218	3141	25.9	1840
TN228-J2-383-1217-1800-09-1346-002	NTWH2-C28	S.HILLS	SHELF	1346	0.01114	0.00144	36126	1037.8	39150
TN228-J2-382-1216-1820-14-1372-001	NTWH2-C29	S.HILLS	SHELF	1372	0.03334	0.00173	27321	416.2	30217
TN228-J2-382-1216-1820-14-1372-002	NTWH2-C30	S.HILLS	SHELF	1372	0.02180	0.00145	30734	536.2	33346
TN228-J2-382-1216-1820-14-1372-003	NTWH2-C31	S.HILLS	SHELF	1372	0.00687	0.00144	40011	1682.9	42584
TN228-J2-382-1216-1619-11-1433-001	NTWH2-C32	S.HILLS	SHELF	1433	0.00360	0.00176	45192	3925.4	46167
TN228-J2-382-1216-1619-11-1433-003	NTWH2-C34	S.HILLS	SHELF	1433	0.00235	0.00144	48617	4919.7	48362
TN228-J2-383-1217-1320-05-1460-001	NTWH2-C35	S.HILLS	SHELF	1460	0.00794	0.00174	38850	1756.2	41560
TN228-J2-383-1217-1320-05-1460-002	NTWH2-C36	S.HILLS	SHELF	1460	0.00862	0.00144	38188	1338.8	41068
TN228-J2-383-1217-1320-05-1460-003	NTWH2-C37	S.HILLS	SHELF	1460	0.01745	0.00145	32520	668.3	35267
TN228-J2-383-1217-1024-04-1500-001	NTWH2-D01-2	S.HILLS	SHELF	1500	0.84102	0.00303	1391	28.9	133
TN228-J2-383-1217-0725-01-1575-001	NTWH2-D02	S.HILLS	SHELF	1575	0.06177	0.00170	22366	221.2	24429
TN228-J2-383-1217-0725-01-1575-002	NTWH2-D03	S.HILLS	SHELF	1575	0.04238	0.00142	25393	268.6	28279
TN228-J2-383-1217-0725-01-1575-003	NTWH2-D04	S.HILLS	SHELF	1575	0.02923	0.00142	28376	390.9	31020
TN228-J2-383-1217-0725-01-1575-004	NTWH2-D05	S.HILLS	SHELF	1575	0.02197	0.00147	30669	536.9	33256
TN228-J2-383-1217-0725-01-1575-005	NTWH2-D06	S.HILLS	SHELF	1575	0.01326	0.00144	34729	872.6	37554
TN228-J2-383-1217-0725-01-1575-006	NTWH2-D07	S.HILLS	SHELF	1575	0.13654	0.00138	15995	81.1	17144
TN228-J2-387-1226-1635-23-1599-001	NTWH2-D08	S.HILLS	SHELF	1599	0.20130	0.00167	12876	66.6	12846
TN228-J2-387-1226-1635-23-1599-002	NTWH2-D09	S.HILLS	SHELF	1599	0.20847	0.00141	12596	54.2	12621
TN228-J2-387-1226-1635-23-1599-003	NTWH2-D10	S.HILLS	SHELF	1599	0.21655	0.00138	12290	51.2	12265
TN228-J2-387-1226-1635-23-1599-004	NTWH2-D11	S.HILLS	SHELF	1599	0.21544	0.00155	12331	57.9	12318
TN228-J2-387-1226-1635-23-1599-005	NTWH2-D12-2	S.HILLS	SHELF	1599	0.19680	0.00138	13058	56.1	13041
TN228-J2-387-1226-0615-017-1748-001	NTWH2-E01	S.HILLS	SHELF	1748	0.18516	0.00164	13548	71.3	13502
TN228-J2-387-1226-0615-017-1748-002	NTWH2-E02	S.HILLS	SHELF	1748	0.21514	0.00136	12342	50.8	12341
TN228-J2-387-1226-0615-017-1748-004	NTWH2-E03	S.HILLS	SHELF	1748	0.14146	0.00138	15710	78.5	16911
TN228-J2-387-1226-0615-017-1748-005	NTWH2-E04	S.HILLS	SHELF	1748	0.19807	0.00141	13007	57.0	12997
TN228-J2-387-1226-0615-017-1748-007	NTWH2-E05	S.HILLS	SHELF	1748	0.19382	0.00163	13181	67.7	13184
TN228-J2-387-1226-0615-017-1748-008	NTWH2-E06	S.HILLS	SHELF	1748	0.20090	0.00147	12893	58.9	12863
TN228-J2-387-1226-0615-017-1748-009	NTWH2-E07	S.HILLS	SHELF	1748	0.18434	0.00162	13583	70.6	13540
TN228-J2-387-1226-0615-017-1748-010	NTWH2-E08	S.HILLS	SHELF	1748	0.18876	0.00136	13393	57.8	13348
TN228-J2-387-1226-0615-017-1748-011	NTWH2-E09	S.HILLS	SHELF	1748	0.14158	0.00138	15704	78.2	16907
TN228-J2-387-1226-0615-017-1748-012	NTWH2-E10	S.HILLS	SHELF	1748	0.20704	0.00135	12651	52.5	12648
TN228-J2-387-1225-0439-04-2004-001	NTWH2-E11	S.HILLS	SHELF	2004	0.76103	0.00232	2194	24.5	853
TN228-J2-387-1225-0439-04-2004-006	NTWH2-E16	S.HILLS	SHELF	2004	0.72050	0.00191	2633	21.3	1291
TN228-J2-387-1225-0439-04-2004-007	NTWH2-E17	S.HILLS	SHELF	2004	0.82296	0.00270	1565	26.4	388
TN228-J2-387-1225-0439-04-2004-009	NTWH2-E18	S.HILLS	SHELF	2004	0.82792	0.00203	1517	19.7	304
TN228-J2-387-1225-0439-04-2004-010	NTWH2-E19	S.HILLS	SHELF	2004	0.71407	0.00213	2705	24.0	1300
TN228-J2-387-1225-0439-04-2004-011	NTWH2-E20	S.HILLS	SHELF	2004	0.68165	0.00187	3079	22.0	1656
TN228-J2-387-1225-0147-02-2066-001	NTWH2-E21	S.HILLS	SHELF	2066	0.80666	0.00245	1726	24.4	515
TN228-J2-387-1225-0147-02-2066-007	NTWH2-E22	S.HILLS	SHELF	2066	0.79234	0.00228	1870	23.1	603
TN228-J2-387-1225-0147-02-2066-008	NTWH2-E23	S.HILLS	SHELF	2066	0.82858	0.00302	1511	29.3	304
TN228-J2-387-1225-0147-02-2066-009	NTWH2-E24	S.HILLS	SHELF	2066	0.74247	0.00193	2392	20.8	1015
TN228-J2-387-1225-0147-02-2066-010	NTWH2-E25	S.HILLS	SHELF	2066	0.76577	0.00190	2144	19.9	776
TN228-J2-387-1225-0147-02-2066-010	NTWH2-E25-2	S.HILLS	SHELF	2066	0.76488	0.00198	2153	20.8	828
TN228-J2-395-0113-0902-01-2193-005	NTWH2-E26	S.HILLS	SHELF	2193	0.82580	0.00238	1538	23.2	387
TN228-J2-395-0113-0902-01-2193-007	NTWH2-E27	S.HILLS	SHELF	2193	0.79738	0.00274	1819	27.6	587
TN228-J2-395-0113-1206-01-2193-025	NTWH2-E28	S.HILLS	SHELF	2193	0.81699	0.00200	1624	19.6	451
TN228-J2-393-0112-0124-06-1657-001	NTWH2-F01	KNOB	SOUTHWEST	1657	0.02998	0.00172	28173	459.9	30865
TN228-J2-393-0112-0124-06-1657-004	NTWH2-F04	KNOB	SOUTHWEST	1657	0.02648	0.00194	29172	590.0	31661

TN228-J2-393-0112-0124-06-1657-005	NTWH2-F05	KNOB	SOUTHWEST	1657	0.00559	0.00196	41666	2822.7	43787
TN228-J2-393-0112-0124-06-1657-005	NTWH2-F05-2	KNOB	SOUTHWEST	1657	0.00721	0.00196	39619	2184.7	42141
TN228-J2-393-0112-0124-06-1657-006	NTWH2-F06	KNOB	SOUTHWEST	1657	0.02191	0.00194	30693	711.2	33252
TN228-J2-393-0112-0124-06-1657-006	NTWH2-F06-2	KNOB	SOUTHWEST	1657	0.02184	0.00195	30717	715.3	33279
TN228-J2-393-0112-0124-06-1657-007	NTWH2-F07	KNOB	SOUTHWEST	1657	0.03680	0.00192	26528	419.3	29454
TN228-J2-393-0112-0124-06-1657-007	NTWH2-F07-2	KNOB	SOUTHWEST	1657	0.03751	0.00193	26374	413.1	29268
TN228-J2-393-0112-0124-06-1657-008	NTWH2-F08	KNOB	SOUTHWEST	1657	0.00310	0.00197	46407	5116.3	46152
TN228-J2-393-0112-0124-06-1657-008	NTWH2-F08-2	KNOB	SOUTHWEST	1657	0.00320	0.00197	46145	4933.6	46137
TN228-J2-393-0112-0124-06-1657-009	NTWH2-F09	KNOB	SOUTHWEST	1657	0.03762	0.00197	26350	419.9	29240
TN228-J2-393-0112-0124-06-1657-010	NTWH2-F10	KNOB	SOUTHWEST	1657	0.02443	0.00194	29817	637.1	32298
TN228-J2-393-0112-0124-06-1657-010	NTWH2-F10-2	KNOB	SOUTHWEST	1657	0.02471	0.00194	29725	629.6	32211
TN228-J2-390-1615-06-2170-001	NTWH2-F11	CASCADE	EAST	2170	0.83858	0.00240	1414	23.0	154
TN228-J2-390-1615-06-2170-002	NTWH2-F12	CASCADE	EAST	2170	0.82808	0.00315	1515	30.6	306
TN228-J2-390-1615-06-2170-003	NTWH2-F13	CASCADE	EAST	2170	0.78882	0.00198	1906	20.2	592
TN228-J2-390-1615-06-2170-004	NTWH2-F14	CASCADE	EAST	2170	0.82148	0.00204	1580	20.0	387
TN228-J2-390-1615-06-2170-005	NTWH2-F15	CASCADE	EAST	2170	0.83348	0.00207	1463	19.9	169
TN228-J2-390-0113-1145-04-2279-01	NTWH2-G01	CASCADE	EAST	2279	0.66330	0.00238	3298	28.8	1859
TN228-J2-390-0113-1145-04-2279-02	NTWH2-G02	CASCADE	EAST	2279	0.75802	0.00192	2226	20.4	861
TN228-J2-390-0113-1145-04-2279-03	NTWH2-G03	CASCADE	EAST	2279	0.84170	0.00242	1384	23.1	122
TN228-J2-390-0113-1145-04-2279-04	NTWH2-G04	CASCADE	EAST	2279	0.66213	0.00261	3312	31.6	2011
TN228-J2-390-0113-1145-04-2279-05	NTWH2-G05	CASCADE	EAST	2279	0.63580	0.00193	3638	24.4	2038
TN228-J2-390-0113-1145-04-2279-06	NTWH2-G06	CASCADE	EAST	2279	0.69538	0.00206	2918	23.8	1544
TN228-J2-390-0113-1145-04-2279-07	NTWH2-G07	CASCADE	EAST	2279	0.66156	0.00208	3319	25.2	2031
TN228-J2-390-0113-1145-04-2279-08	NTWH2-G08	CASCADE	EAST	2279	0.81743	0.00337	1619	33.1	403
TN228-J2-390-0113-1145-04-2279-09	NTWH2-G09	CASCADE	EAST	2279	0.75851	0.00253	2220	26.7	853
TN228-J2-390-0113-1145-04-2279-10	NTWH2-G10	CASCADE	EAST	2279	0.67662	0.00202	3138	24.0	1769
TN228-J2-390-0103-1024-03-2281-001	NTWH2-G11	CASCADE	EAST	2281	0.81717	0.00343	1622	33.7	431
TN228-J2-392-0110-1120-07-2341-001	NTWH2-G12	FINGER	SOUTHWEST	2341	0.80803	0.00236	1712	23.4	511
TN228-J2-392-0110-1120-07-2341-003	NTWH2-G14	FINGER	SOUTHWEST	2341	0.68843	0.00203	2999	23.6	1588
TN228-J2-392-0110-1120-07-2341-004	NTWH2-G15	FINGER	SOUTHWEST	2341	0.81484	0.00279	1645	27.5	444
TN228-J2-391-0109-0930-25-2386-001	NTWH2-G16	FRACTURE	SOUTHWEST	2386	0.77048	0.00250	2095	26.1	746
TN228-J2-391-0109-0930-25-2386-002	NTWH2-G17	FRACTURE	SOUTHWEST	2386	0.71227	0.00210	2726	23.7	1351
TN228-J2-391-0109-0930-25-2386-003	NTWH2-G18	FRACTURE	SOUTHWEST	2386	0.79833	0.00289	1809	29.1	551
TN228-J2-391-0109-0930-25-2386-004	NTWH2-G19	FRACTURE	SOUTHWEST	2386	0.72737	0.00213	2557	23.5	1176
TN228-J2-390-0103-0815-02-2395-001	NTWH2-G20	CASCADE	EAST	2395	0.75753	0.00220	2231	23.4	871
TN228-J2-390-0103-0815-02-2395-002	NTWH2-G21	CASCADE	EAST	2395	0.74585	0.00223	2356	24.1	1008
TN228-J2-390-0103-0815-02-2395-003	NTWH2-G22	CASCADE	EAST	2395	0.81010	0.00271	1692	26.9	503
TN228-J2-390-0103-0815-02-2395-004	NTWH2-G23	CASCADE	EAST	2395	0.74597	0.00229	2354	24.7	1001
TN228-J2-390-0103-0815-02-2395-005	NTWH2-G24	CASCADE	EAST	2395	0.76308	0.00228	2172	24.0	834
TN228-J2-390-0103-0815-02-2395-006	NTWH2-G25	CASCADE	EAST	2395	0.83515	0.00284	1447	27.3	180
TN228-J2-390-0103-0815-02-2395-007	NTWH2-G26	CASCADE	EAST	2395	0.73395	0.00235	2485	25.8	1108
TN228-J2-390-0103-0815-02-2395-008	NTWH2-G27	CASCADE	EAST	2395	0.77098	0.00235	2089	24.5	733
TN228-J2-390-0103-0815-02-2395-009	NTWH2-G28	CASCADE	EAST	2395	0.80558	0.00342	1737	34.1	518
TN228-J2-390-0103-0815-02-2395-010	NTWH2-G29	CASCADE	EAST	2395	0.75247	0.00230	2285	24.6	910
TN228-J2-389-0101-1024-10-1261-001	NTWH2-G30	EAST OF ST. HELENS	EAST	1261	0.76879	0.00227	2112	23.7	752
TN228-J2-389-0101-0930-07-1296-001	NTWH2-G31	EAST OF ST. HELENS	EAST	1296	0.84218	0.00245	1380	23.4	113
TN228-J2-393-0111-1851-2-1816-002	NTWH2-G32	KNOB	SOUTHWEST	1816	0.14756	0.00181	15371	98.5	16626
TN228-J2-393-0111-1851-2-1816-004	NTWH2-G33	KNOB	SOUTHWEST	1816	0.14108	0.00183	15732	103.9	16930
TN228-J2-393-0111-1851-2-1816-005	NTWH2-G34	KNOB	SOUTHWEST	1816	0.14652	0.00180	15428	98.5	16686
TN228-J2-393-0111-1851-2-1816-007	NTWH2-G35	KNOB	SOUTHWEST	1816	0.14539	0.00180	15490	99.5	16741
TN228-J2-393-0111-1851-2-1816-008	NTWH2-G36	KNOB	SOUTHWEST	1816	0.01621	0.00195	33111	965.6	35797
TN228-J2-393-0112-0730-13-1442-001	NTWH2-G37	KNOB	SOUTHWEST	1442	0.13937	0.00219	15830	126.1	17010
TN228-J2-389-0101-0732-04-1373-002	NTWH2-G38-2	EAST OF ST. HELENS	EAST	1373	0.46792	0.00189	6101	32.5	4428
TN228-J2-389-0101-0732-04-1373-005	NTWH2-G39	EAST OF ST. HELENS	EAST	1373	0.00930	0.00204	37572	1762.5	40346
TN228-J2-389-0101-0732-04-1373-006	NTWH2-G40	EAST OF ST. HELENS	EAST	1373	0.00611	0.00198	40956	2607.3	43209
TN228-J2-385-1221-0558-05-1060-006	NTWH2-H01	S.HILLS	SHELF	1060	0.44383	0.00230	6525	41.6	5797
TN228-J2-385-1221-0558-05-1060-007	NTWH2-H02	S.HILLS	SHELF	1060	0.45758	0.00224	6280	39.4	5597
TN228-J2-390-0103-1615-06-2170-006	NTWH2-H04-2	CASCADE	EAST	2170	0.82576	0.00260	1538	25.3	379
TN228-J2-390-0103-1615-06-2170-007	NTWH2-H05	CASCADE	EAST	2170	0.83090	0.00537	1488	51.9	275
TN228-J2-395-0113-0902-01-2193-010	NTWH2-H06-2	S.HILLS	SHELF	2193	0.81063	0.00234	1686	23.2	477
TN228-J2-395-0113-0902-01-2193-005	NTWH2-H07-2	S.HILLS	SHELF	2193	0.81692	0.00394	1624	38.7	432
TN228-J2-395-0113-0902-01-2193-007	NTWH2-H08-2	S.HILLS	SHELF	2193	0.79965	0.00234	1796	23.6	546
TN228-J2-395-0113-0902-01-2193-008	NTWH2-H09-2	S.HILLS	SHELF	2193	0.80049	0.00323	1788	32.4	523
TN228-J2-395-0113-0902-01-2193-009	NTWH2-H10	S.HILLS	SHELF	2193	0.82237	0.00245	1571	23.9	388
TN228-J2-395-0113-1206-01-2193-021	NTWH2-H11	S.HILLS	SHELF	2193	0.82236	0.00342	1571	33.4	389
TN228-J2-395-0113-1206-01-2193-022	NTWH2-H12	S.HILLS	SHELF	2193	0.78192	0.00250	1976	25.7	663
TN228-J2-395-0113-1206-01-2193-023	NTWH2-H13	S.HILLS	SHELF	2193	0.84364	0.00250	1366	23.8	113
TN228-J2-395-0113-1206-01-2193-024	NTWH2-H14	S.HILLS	SHELF	2193	0.79997	0.00313	1793	31.4	546
TN228-J2-395-0113-1206-01-2193-025	NTWH2-H15-2	S.HILLS	SHELF	2193	0.80749	0.00398	1718	39.6	513
TN228-J2-395-0113-1206-01-2193-026	NTWH2-H16	S.HILLS	SHELF	2193	0.80890	0.00242	1704	24.0	506
TN228-J2-395-0113-1206-01-2193-027	NTWH2-H17	S.HILLS	SHELF	2193	0.78927	0.00237	1901	24.1	595
TN228-J2-395-0113-1206-01-2193-028	NTWH2-H18	S.HILLS	SHELF	2193	0.78968	0.00238	1897	24.2	600
TN228-J2-395-0113-1206-01-2193-029	NTWH2-H19	S.HILLS	SHELF	2193	0.83370	0.00404	1461	38.9	181

TN228-J2-395-0113-1206-01-2193-030	NTWH2-H20	S.HILLS	SHELF	2193	0.74564	0.00259	2358	27.9	1009
TN228-J2-387-1226-1148-20-1680-009	NTWH2-H21	S.HILLS	SHELF	1680	0.22458	0.00256	11997	91.7	11681
TN228-J2-387-1226-1148-20-1680-010	NTWH2-H22	S.HILLS	SHELF	1680	0.19829	0.00185	12998	74.8	12985
TN228-J2-387-1226-1148-20-1680-07	NTWH2-H23	S.HILLS	SHELF	1680	0.22189	0.00176	12094	63.5	11889
TN228-J2-387-1226-1148-20-1680-06	NTWH2-H24	S.HILLS	SHELF	1680	0.20662	0.00181	12667	70.2	12662
TN228-J2-387-1226-1148-20-1680-08	NTWH2-H25	S.HILLS	SHELF	1680	0.20182	0.00227	12856	90.2	12836
TN228-J2-392-0110-1547-10-2217-001	NTWH2-H26	FINGER	SOUTHWEST	2217	0.81958	0.00299	1598	29.3	390
TN228-J2-387-1224-2355-1-2051-06	NTWH2-H27	S.HILLS	SHELF	2051	0.73908	0.00218	2429	23.7	1030
TN228-J2-395-0113-1530-03-2090-005	NTWH2-H28	S.HILLS	SHELF	2090	0.83102	0.00341	1487	32.9	192
TN228-J2-395-0113-1530-03-2090-006	NTWH2-H29	S.HILLS	SHELF	2090	0.82867	0.00304	1510	29.4	296
TN228-J2-395-0113-1530-03-2090-007	NTWH2-H30	S.HILLS	SHELF	2090	0.84171	0.00751	1384	71.6	144
TN228-J2-395-0113-1530-03-2090-008	NTWH2-H31	S.HILLS	SHELF	2090	0.83372	0.00720	1461	69.4	198
TN228-J2-395-0113-1530-03-2090-009	NTWH2-H32	S.HILLS	SHELF	2090	0.83247	0.00674	1473	65.1	198
TN228-J2-395-0113-1530-03-2090-010	NTWH2-H33	S.HILLS	SHELF	2090	0.83481	0.00230	1450	22.2	175
TN228-J2-392-0110-1409-08-2225-01	NTWH2-H34	FINGER	SOUTHWEST	2225	0.28613	0.00180	10052	50.6	9099
TN228-J2-392-0110-1409-08-2225-02	NTWH2-H35	FINGER	SOUTHWEST	2225	0.36428	0.00144	8112	31.7	7647
TN228-J2-392-0110-1409-08-2225-05	NTWH2-H36	FINGER	SOUTHWEST	2225	0.38679	0.00144	7630	30.0	6558
TN228-J2-392-0110-1409-08-2225-08	NTWH2-H37	FINGER	SOUTHWEST	2225	0.41798	0.00181	7007	34.8	6445
TN228-J2-392-0110-1409-08-2225-09	NTWH2-H38	FINGER	SOUTHWEST	2225	0.37604	0.00258	7857	55.1	7318
TN228-J2-387-1224-2355-1-2051-09	NTWH2-H39	S.HILLS	SHELF	2051	0.81933	0.00288	1601	28.2	393
TN228-J2-393-0112-0730-13-1442-007	NTWH2-H40	KNOB	SOUTHWEST	1442	0.24042	0.00173	11450	57.9	10913
TN228-J2-393-0112-0730-13-1442-008	NTWH2-H41	KNOB	SOUTHWEST	1442	0.25280	0.00183	11047	58.1	10323
TN228-J2-390-0104-0815-16-968-003	NTWH2-H42	CASCADE	EAST	968	0.00873	0.00190	38087	1745.0	40838
TN228-J2-390-0104-0815-16-968-004	NTWH2-H43	CASCADE	EAST	968	0.01452	0.00193	33998	1066.3	36746
TN228-J2-390-0104-0815-16-968-005	NTWH2-H44	CASCADE	EAST	968	0.02351	0.00186	30126	635.4	32592
TN228-J2-386-1223-1345-011-899-003	NTWH2-H45	S.HILLS	SHELF	899	0.89722	0.00253	871	22.6	80
TN228-J2-386-1223-1345-011-899-006	NTWH2-H46	S.HILLS	SHELF	899	0.87986	0.00184	1028	16.8	285
TN228-J2-386-1223-1345-011-899-010	NTWH2-H47	S.HILLS	SHELF	899	0.87880	0.00197	1038	18.1	291

Table 4.3-Statistical results of comparing different coral populations

Distribution 1	Distribution 2	Wilcoxon Test Results		Brown Forsythe	
		Rank Sum	p-values	F	p value
YD (NA)	20000-30000 (NA)	460.5	0.10500	35.9736	<e-4
YD (NA)	H1 (NA)	1331	0.95400	8.4929	0.0044
YD (NA)	ACR (SO)	814	0.04610	23.6922	<e-4
H1 (NA)	LGM (NA)	637.5	0.00012	28.8051	<e-4
H1 (NA)	ACR (SO)	854	0.00004	14.1331	0.003
LGM (NA)	ACR (SO)	504	0.35640	5.2879	0.026
20000-30000 (NA)	0-10000 (NA)	780	0.00000	1.4049	0.2421
20000-30000 (NA)	10000-20000 (NA)	1061.5	0.00570	36.3609	<e-4
20000-30000 (NA)	30000-40000 (NA)	693	0.07220	11.7331	0.0012
20000-30000 (NA)	40000-50000 (NA)	506	0.37360	49.0273	<e-4

Table 4.3 Wilcoxon and Brown-Forsythe test results for comparing depth distributions during different time periods in this study. North Atlantic distributions are indicated by (NA) and Southern Ocean distributions are indicated by (SO).

Table 3.4-U-Series and Libby Age of Antarctic Cold Reversal (ACR) Corals

Name of Coral	Seamount	Depth	Libby Age	U/Th date
ESA01	Shelf	1898	13089	14314
ESD04	Shelf	1947	12204	13649
NTWH2-E07	Shelf	1748	13583	15253
NTWH2-H41	Southwest	1442	11047	12374
ESI04	Shelf	1000	14342	16652
NTWH2-G37	Southwest	1442	15830	17850
NTWH2-D07	Shelf	1575	15995	17939
NTWH2-G33	Southwest	1816	15732	18253
NTWH2-G34	Southwest	1816	15428	17746
NTWH2-D12	Shelf	1599	13058	14639

Table 3.4: Reconnaissance 14C ages and U/Th ages of Southern Ocean corals from the ACR mode. These U/Th ages confirm that the mode seen in the Southern ocean data set is the ACR and not the YD or H1

Chapter 4:

Evidence for the Buildup of the Thermobaric Capacitor in Deep North Atlantic Waters During the Last Deglaciation

4.1 INTRODUCTION

Ice core records from the past 800,000 years are broadly characterized by eight shifts from glacial to interglacial states forced by solar insolation on the 20,000, 40,000 and 100,000 year time scales (1). CO_2 and temperature closely follow each other during these shifts (Figure 4.1); however, there is a strong nonlinear response of climate to solar insolation. The classic "sawtooth" structure of glacial cycles requires an extra forcing, and although CO_2 rise does not precede glacial-interglacial (G/IG) shifts, it is one of the most important amplifiers to temperature change in the climate system. The deep ocean has been long been considered a central part of the climate shifts because it contains more than sixty times CO_2 than the atmosphere and is a large heat reservoir.

However, during the last glacial period, there were several extremely abrupt and large amplitude climate shifts characterized by dramatic changes in temperature (2). There are twenty one of these Dansgaard-Oeschger events and although they were first recognized in the ice cores, they have later been seen in a variety of marine (3, 4) and terrestrial archives (5, 6). Methane synchronization of the Greenland and Antarctic ice cores has shown that the Antarctica warms during the coldest of these rapid climate change events (Heinrich (H) Events) 1,000 to 3,000 years before Greenland (7). These changes further implicate the deep ocean as an important factor in climate shifts as the deep ocean is one of the only reservoirs in the climate system with the 'memory' to cause such a phase difference between Antarctica and Greenland on the millennial time scale.

The last termination or deglaciation is the most recent example of a G/IG climate shift. The termination began in Antarctica (8) and the Southern Ocean (9) at ~ 18 ka, and

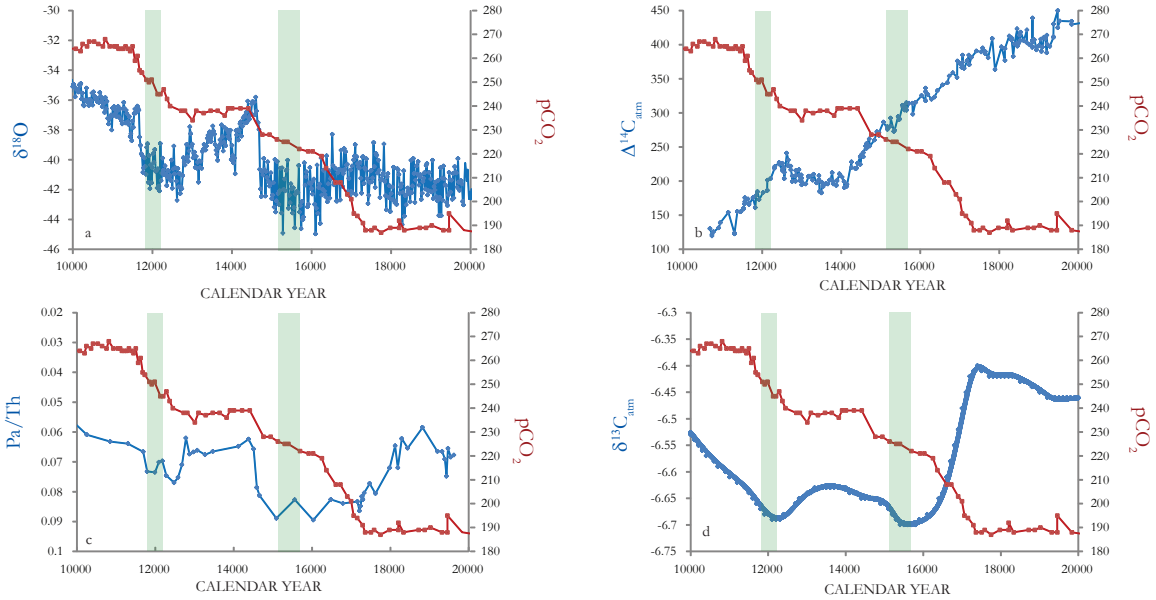

Figure 4.1: Ice core and marine recconstructions illustrating the evolution of major components of the climate system between 10 kya to 20kya. (A) pCO_2 and $\delta^{18}O$ (a proxy for temperature) reconstructions from ice core. (B) Reconstructed $\Delta^{14}C_{atm}$ from the ^{230}Th-dated Hulu cave record with pCO_2. (C) Pa/Th from the North Atlantic (a proxy for AMOC) with pCO_2. (D) $\delta^{13}C_{atm}$ of atmospheric CO_2 from the EPICA Dome C core and Talos Dome Ice Core with pCO2. All ice core records are plotted on a synchronized age scale. The grey shaded regions indicate the age range of corals used in the YD profile and H1 profile.

by 7,000 years only a small section of the Laurentide Ice Sheet that had covered all of North America was left. However, the warming was not gradual, but punctuated by several abrupt climatic shifts. Temperature records from Greenland and the North Atlantic reveal a cold interval (Heinrich Stadial 1) during which a massive ice rafted debris (IRD) field formed in the North Atlantic. This IRD event at 17.5 ka coincides with shut down of Atlantic Meridional Ocean Circulation (AMOC) circulation and the beginning of the rise in CO_2 (Figure 4.1c). In the North Atlantic, this cold interval was followed by an abrupt warming into the Bolling-Allerod (B/A) warm period at 14.7 ka. The B/A was then subsequently followed by a rapid return to near glacial conditions during the Younger Dryas (~ 12.8–11.5kya).

The Southern Hemisphere responded differently by warming more gradually between 17.5 ka and the Holocene. While Heinrich Stadial 1 (H1) in the Northern Hemisphere occurred, the Southern Hemisphere slowly warmed until the B/A. During the abrupt warming in the Northern Hemisphere, the Southern Hemisphere cooled (Antarctic Cold Reversal (ACR)) while CO_2 remained constant. As the Younger Dryas occurred in the Northern Hemisphere, the Southern Hemisphere slowly warmed and CO_2 began to rise.

To understand the role carbon cycle changes in these warmings, $\delta^{13}C_{atm}$ and $\Delta^{14}C_{atm}$ measurements have been made (Figure 4.1). These two carbon isotopes show some similar patterns to each other and CO_2 during the deglaciation. Both $\delta^{13}C_{atm}$ and $\Delta^{14}C_{atm}$ begin to decline at 17.5 ka. However there are extra features in these two records that are difficult to explain, for instance changes in slope at 16.2 ka and 15.4 ka that are difficult to explain.

There are two main hypotheses for explaining the offset between NH and SH. The first involves a southward shift to the Westerlies and the second is the "Bipolar See-Saw". Chiang and Bitz (10) demonstrated that the spread of winter sea ice over the Northern North Atlantic shifts the ITCZ and Southern westerly wind belt further south. This mechanism rapidly transfers the climate signal between hemispheres.

The Bipolar See-Saw is a marine-based explanation and involves an oscillating

AMOC regime hypothesized to be driven by changes in North Atlantic Deep Water (NADW) and Antarctic Bottom Water (AABW) formation. It is instigated by an increase in Northern Hemisphere summer insolation, which melts ice to trigger a reduction in AMOC. This reduction cools the Northern Hemisphere at the expense of warming the Southern Hemisphere. Eventually CO_2 is degassed from a warm, radiocarbon depleted and carbon rich water mass in the Southern Ocean, triggering global warming and the resumption of the AMOC. It is possible the two mechanisms occurred together with the bipolar see saw helping move the zonal wind systems further South by changing the sea surface temperature gradients (11).

The exact mechanism for the resumption of the AMOC after the release of CO_2 is not known, but one explanation for the resumption which is also consistent with the patterns of warming seen in the different hemispheres is the "Thermobaric Capacitor" hypothesis" (12). Pore fluid estimates of the distribution of $\delta^{18}O_w$ during the Last Glacial Maximum (LGM) shows that modern arrangement of salty northern source waters and relatively fresh southern source waters was reversed during the Last Glacial Maximum (LGM) and that salt dominated the stratification of the deep Atlantic (13). The "Thermobaric Capacior" hypothesis proposes that in the presence of a salt stratified deep ocean, geothermal heat (or warm deep isopycnals) can warm the deepest layers of the ocean while maintaining the static stability of the water column. The thermobaricity of seawater can allow for a virtually instantaneous release of the energy stored in the warm deep water causing abrupt overturning of the water column. This overturning can bring salt to the areas of deep-water convection in the glacial North Atlantic and reinvigorate northern source deep-water formation.

In Chapter 2 we have demonstrated that clumped isotope paleothermometry can be used to generate subdegree precision temperature reconstructions. In Chapter 3 we radiocarbon dated several hundred fossil deep-sea corals to determine their spatial and temporal range. In this study we utilize the results of the previous two chapters. Here, we

present radiocarbon and temperature profiles during the Younger Dryas (YD) and Heinrich 1 (H1) that provide new insights into the role of the ocean in deglacial releases of CO_2 and support for the thermobaric capacitor hypothesis.

4.2 METHODS

Samples examined in this study were obtained from the Caltech Deep-Sea Coral Fossil Collection. The deep-sea corals were *Desmophyllum dianthus* from the New England (34−40°N, 60−68°W) and Corner Rise Seamounts (34−36°N, 47−53°W) collected in 2003−2005 using the deep submergence vehicles ALVIN and HERCULES. Collection by ROV and submarine ensured that the depth of each coral was precisely known and that corals were collected near growth position. All samples in this study were analyzed for U/Th ages, ^{14}C ages and Δ_{47} temperatures.

4.2.i Radiocarbon Dating Method

All samples analyzed for ^{14}C and U/Th were physically cleaned with a Dremel tool, and chemically cleaned by ultrasonicating alternately in $NaOH/H_2O_2$ and MILLI Q water, and then rinsed with Methanol and leached in $HClO_4/H_2O_2$ (14). After this step, an aliquot of 1g was removed for U/Th analysis. Twenty mg of coral was then taken to UC-Irvine for radiocarbon analysis. There, immediately prior to phosphoric acid dissolution and graphitization, each sample was leached in HCl to remove, typically, 50% of its total mass. The resulting coral was hydrolyzed in phosphoric acid, and the evolved CO_2 was graphitized under H_2 on an iron catalyst for ^{14}C analysis (14). Radiocarbon ages were measured at the UC-Irvine Keck-CCAMS facility on an Accelerator Mass Spectrometer.

4.2.ii U-Series Methods

Remaining aliquots of 1 g of coral were processed to extract U and Th (15). Corals were dissolved in concentrated SEASTAR nitric acid and spiked with a ^{229}Th-^{236}U double spike. Uranium and Thorium were scavenged from the resulting solution by iron precipitation. The iron pellet was then dissolved in 8N SEASTAR nitric acid. Uranium and Thorium fractions were separated using trace metal-clean Teflon columns and a Bio

Rad AG-1X-8 Cation Exchange Resin. Eluted fractions were dried down several times after successive drop wise additions of concentrated perchloric acid and SEASTAR nitric acid.

Uranium and Th fractions were brought up in 5% SEASTAR Nitric Acid and separately run on a multi collector inductively coupled mass spectrometer. All samples were bracketed by an instrumental standard or SGS to correct for mass bias and mass drift. Calculated $\delta^{234}U_{initial}$ values ranged from 144–155‰.

4.2.iii Δ_{47} Analysis

All coral samples were physically cleaned with a Dremel tool. Fossil corals, unlike modern corals, typically have a Fe-Mn crust surrounding them. This crust contains trapped organic matter, and can skew isotopic measurements of the bulk coral. A cleaning study was performed on a modern coral and a coral with Fe-Mn crust from Tasmania that had the same radiocarbon age as the modern ocean from which it was collected (Figure 4.2) to determine the best method for removing the Fe-Mn crust. Corals were cleaned four different ways. The first was only physical cleaning with a Dremel tool, the second was physical cleaning and chemical cleaning with 1:1 H_2O_2:NaOH, the third was physical cleaning, and chemical cleaning with 1:1 H_2O_2:NaOH and MeOH and the fourth was physical cleaning and chemical cleaning with 1:1 H_2O_2:NaOH , MeOH and $HClO_4$. It was determined that physical cleaning with a Dremel tool was the only method that yielded expected temperatures.

All fossil corals were cleaned according to procedures detailed in Chapter 2. Corals were physically cleaned with a Dremel tool and powdered with a mortar and pestle. Samples were dissolved in 105% H_3PO_4 at 90°C. The evolved CO_2 was analyzed in a Dual Inlet Finnigan MAT-253 mass spectrometer with the simultaneous collection of ion beams corresponding to masses 44–49 to obtain Δ_{47}, Δ_{48}, Δ_{49}, $\delta^{13}C$ and $\delta^{18}O$ values. The mass 47 beam is composed of $^{17}O^{13}C^{17}O$, $^{17}O^{12}C^{18}O$ and predominantly $^{18}O^{13}C^{16}O$ and we define R^{47} as the abundance of mass 47 isotopologues divided by the mass 44 isotopologue. ($R^{47}=[^{17}O^{13}C^{17}O+ {}^{17}O^{12}C^{18}O+{}^{18}O^{13}C^{16}O\ ]/[\ {}^{16}O^{12}C^{16}O]$.) Δ_{47} is reported

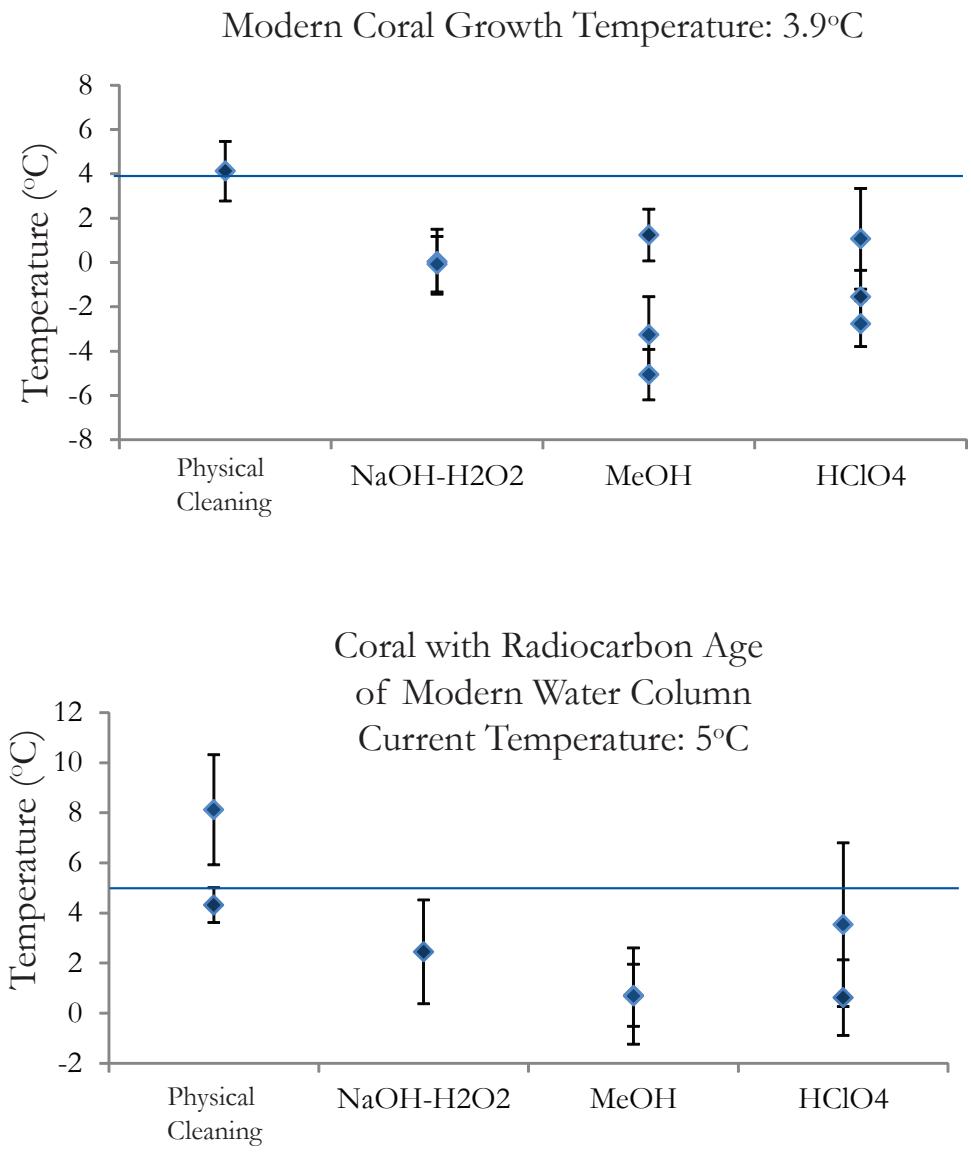

Figure 4.2: Cleaning experiment conducted to determine the best method to remove Fe-Mn crust from fossil corals. A modern coral was cleaned with the cleaning regimen used for radiocarbon cleaning. Reaction with the solvents likely dissolved the carbonate and changed the clumped isotope ratio. A fossil coral with the same age as the water column was also cleaned using the same protocol, and again the cleaning procedure did remove the Fe-Mn crust but also changed the clumped isotope ratio. For all subsequent clumped isotope analyses, corals were only physically cleaned.

relative to a stochastic distribution of isotopologues for the same bulk isotopic composition. (Δ_{47}=(((R$^{47}_{measured}$/R$^{47}_{stochastic}$)-1)- ((R$^{46}_{measured}$/R$^{46}_{stochastic}$)-1)- ((R$^{45}_{measured}$/R$^{45}_{stochastic}$)-1))*1000.) Mass 48 was monitored to detect any hydrocarbon contamination. Measurements of each gas were done at 16V of mass 44 and consisted of 8 acquisitions, each of which involved 7 cycles of sample-standard comparison with an ion integration time of 26s per cycle. Internal standard errors of this population of acquisition to acquisition for Δ_{47} ranged from 0.005–0.01$^{o}/_{oo}$, (1–2^{o}C) while external standard error ranged from 0.005–0.011 $^{o}/_{oo}$ (0.5–2^{o}C). The internal standard error for δ^{13}C ranged from 0.5-80ppm and the internal standard error for δ^{18}O ranged from .9–36ppm. Samples were corrected to standards run during the same session

4.3 RESULTS

We have examined 15 corals for U/Th ages, ^{14}C ages and Δ_{47} temperatures (Table 4.1, Table 4.2, Table 4.3, Table 4.4, Table 4.5, Table 4.6 and Table 4.7, and Figure 4.3). We selected these corals based on the results of a reconnaissance age screening dataset (16) made at NOSAMS at WHOI using a zinc-combustion method (17). These corals were then selected for high-precision ^{14}C dating and clumped isotopologue CO_2 measurements, and U/Th dating. The U/Th dating revealed that five of the analyzed corals were dated to the YD (11.7–12.1 ka BP), one was dated to the Bolling Allerod Event (13.8 ka), six corals were dated to late H1 (15.1–15.7 ka BP, and three corals were dated to early H1 /early deglaciation (16.1–17.7 ka BP). One of the H1 corals, NT 031, has an elevated $^{234}U_i$, so is not included in the Δ^{14}C profiles. These corals are not all at the same YD and H1 calendar age as the reconnaissance dating method had implied because the reconnaissance dating method has larger error bars than U/Th dating. Figure 4.3 shows the Δ_{47} reconstructed temperature profile and the Δ^{14}C profile for the Younger Dryas and Heinrich 1.

During the course of making clumped isotope measurements, we found that there is a possible vital effect in some deep-sea corals (Table 4.4 and Figure 4.4). Measurements with

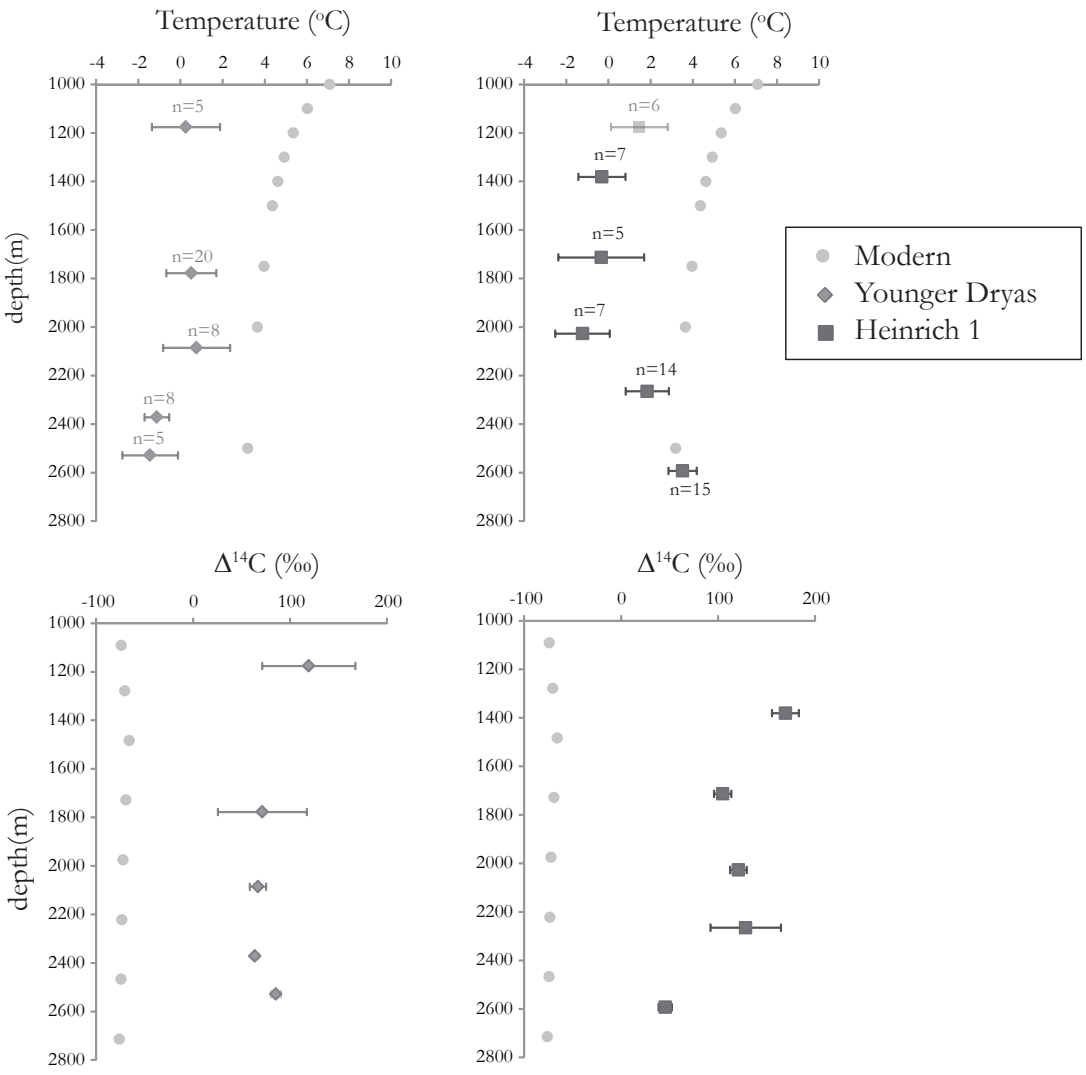

Figure 4.3: The temperature profiles for both the YD and late H1 are cooler than modern. The YD profile is isothermal at all measured depths while the H1 profile exhibits slight warming with depth. The $\Delta^{14}C$ profile for the YD is nearly constant with depth, while the H1 profile shows a depleted point at ~ 2600 m.

Table 4.1-Names and depths of Corals Analyzed

		sample name	seamount	depth
NT	001	ALV-3891-1646-004-001	GREGG	1180
NT	002	RBDASS05-H11-0826-0029-201-4-006-2529	NASHVILLE	2529
NT	006	RBDASS05-H03-0815-1004-314-3-002-1427	LYMAN	1427
NT	007	ALV-3885-1239-001-010	MUIR	2026
NT	009	ALV-3887-1549-004-007	MUIR	2372
NT	010	ALV-3887-1549-004-009	MUIR	2372
NT	011	ALV-3885-1239-001-004	MUIR	2027
NT	012	ALV-3892-1315-001-008	MANNING	1713
NT	013	ALV-3887-1652-005-013	MUIR	2265
NT	014	ALV-3890-1330-002-007	MANNING	1886
NT	015	RBDASS05-H15-0831-2045-605-020-2459	KELVIN	2529
NT	016	RBDASS05-H15-0831-1616-601-3-003-2593	KELVIN	2593
NT	017	ALV-3891-1459-003-006	GREGG	1176
NT	018	RBDASS05-H05-0818-1450-101-004-1316	VERILL	1316
NT	019	RBDASS05-H16-0901-2356-202-021-1918	BALANUS	1918
NT	020	ALV-4162-1457-001-003-2086	PICKETT	2086
NT	030	ALV-3890-1407-003-001	MANNING	1778
NT	031	ALV-3891-1459-003-009	GREGG	1176
NT	032	ALV-3890-1742-007-001	MANNING	1381

Table 4.2 Clumped Isotope Measurements

	SAMPLE	COUNT	AVERAGE	STDEV	STDERR	DEPTH (m)
YOUNGER DRYAS	NT 002	5	-1.5	2.9	1.3	2529
YOUNGER DRYAS	NT 010	8	-1.1	1.7	0.6	2372
YOUNGER DRYAS	NT 017	5	0.3	3.6	1.6	1176
YOUNGER DRYAS	NT 020	8	0.5	4.9	1.7	2086
YOUNGER DRYAS	NT 030	20	0.5	4.6	1.0	1778
HEINRICH 1	NT 031	6	1.7	3.3	1.4	1176
HEINRICH 1	NT 032	7	-0.2	3.0	1.1	1381
HEINRICH 1	NT 012	5	-0.7	5.0	2.3	1713
HEINRICH 1	NT 007	7	-1.2	3.4	1.3	2027
HEINRICH 1	NT 013	14	1.6	-4.1	-1.1	2265
HEINRICH 1	NT 016	15	3.5	2.6	0.7	2593
EARLY H1	NT 014	9	1.3	4.8	1.6	1886
EARLY H1	NT 015	9	-0.8	3.4	1.1	2459
EARLY H1	NT 006	3	-1.1	1.6	0.9	1427
BOLLING/ALLEROD	NT 018	4	3.1	1.2	0.6	1316

Table 4.3														
name	date	d47	d47err	FullD47	D47err	d48	FullD48	d13C	d18O	D47	Stretched D47	Acid corrected D47	Standard Corrected D47	T
NT012	April-10	13.6150	0.0171	0.1721	0.0095	58.4758	25.4124	-6.5293	41.3673	0.6127	0.7029	0.7829	0.7818	-1.4
NT012	April-10	13.8559	0.0162	0.1506	0.0104	58.2766	25.0367	-6.3553	41.4599	0.5859	0.6722	0.7522	0.7501	4.1
NT012	April-10	13.7490	0.0192	0.1465	0.0094	58.3591	25.1672	-6.4340	41.4343	0.5842	0.6702	0.7502	0.7480	4.5
NT013	April-10	13.1041	0.0113	0.1449	0.0088	58.8208	25.3744	-7.2139	41.5580	0.5966	0.6844	0.7644	0.7627	1.9
NT013	April-10	13.0673	0.0156	0.1515	0.0094	58.7911	25.3781	-7.2414	41.5416	0.6040	0.6929	0.7729	0.7715	0.3
NT013	April-10	13.1023	0.0190	0.1262	0.0100	58.5929	25.2176	-7.1635	41.5255	0.5779	0.6630	0.7430	0.7406	5.8
NT 014	April-10	14.1518	0.0136	0.1733	0.0099	60.8201	26.4465	-6.6184	41.9956	0.6023	0.6909	0.7709	0.7695	0.7
NT 014	April-10	14.1192	0.0116	0.1613	0.0076	60.4212	26.0814	-6.6285	41.9850	0.5909	0.6779	0.7579	0.7560	3.1
NT 014	April-10	13.7587	0.0423	0.1391	0.0109	59.3339	25.4192	-6.7061	41.8219	0.5766	0.6614	0.7414	0.7390	6.1
NT 015	April-10	18.8515	0.0126	0.2574	0.0079	65.0206	28.0563	-3.1758	43.2323	0.5840	0.6699	0.7499	0.7478	4.5
NT 015	April-10	18.9207	0.0147	0.2600	0.0085	64.9233	27.9251	-3.1271	43.2509	0.5852	0.6713	0.7513	0.7492	4.3
NT 016	April-10	17.3602	0.0134	0.2355	0.0106	63.9554	27.6709	-4.3414	42.9083	0.5946	0.6821	0.7621	0.7604	2.3
NT 016	April-10	17.0993	0.0108	0.2269	0.0101	63.6578	27.4826	-4.5470	42.8583	0.5917	0.6788	0.7588	0.7569	2.9
NT 016	April-10	17.7141	0.0124	0.2473	0.0099	64.0952	27.5258	-4.1371	43.0500	0.5987	0.6868	0.7668	0.7652	1.4
NT 017	April-10	16.8563	0.0111	0.2319	0.0084	59.0975	25.5606	-3.5179	41.5911	0.6019	0.6905	0.7705	0.7691	0.8
NT 018	April-10	15.6313	0.0142	0.1864	0.0087	58.8818	25.5159	-4.6358	41.5104	0.5832	0.6690	0.7490	0.7468	4.7
NT 018	April-10	15.3945	0.0123	0.1922	0.0096	58.2708	25.1616	-4.7610	41.3898	0.5941	0.6815	0.7615	0.7597	2.4
NT 019	April-10	12.2227	0.0095	0.1209	0.0081	56.1129	24.1274	-7.3800	40.8581	0.5918	0.6789	0.7589	0.7571	2.9
NT 019	April-10	12.2340	0.0120	0.1628	0.0088	56.6165	24.6260	-7.4068	40.8530	0.6334	0.7266	0.8066	0.8064	-5.5
NT 020	April-10	18.9524	0.0138	0.2882	0.0089	62.9427	27.0406	-2.5943	42.7274	0.6127	0.7028	0.7828	0.7818	-1.4
NT 020	April-10	18.7998	0.0147	0.2654	0.0111	62.4374	26.6975	-2.6511	42.6536	0.5931	0.6804	0.7604	0.7586	2.6
NT 020	April-10	18.9561	0.0129	0.2709	0.0086	62.6102	26.7573	-2.5528	42.7080	0.5953	0.6829	0.7629	0.7612	2.1
102 GC AZ 01	April-10	3.1611	0.0100	-0.1458	0.0082	-2.4151	-1.1915	0.4909	24.3121	0.5222	0.5991	0.6791		
102 GC AZ 01	April-10	3.4705	0.0101	-0.1404	0.0096	-1.3628	-0.5868	0.5679	24.5421	0.5209	0.5976	0.6776		
102 GC AZ 01	April-10	3.4985	0.0095	-0.1243	0.0089	-1.2178	-0.5379	0.5289	24.5916	0.5364	0.6154	0.6954		
102 GC AZ 01	April-10	3.0765	0.0132	-0.1958	0.0094	-2.5988	-1.2154	0.5400	24.2298	0.4741	0.5439	0.6239		
102 GC AZ 01	April-10	2.9058	0.0171	-0.1682	0.0111	-3.1195	-1.4997	0.4604	24.1084	0.5054	0.5798	0.6598		
102 GC AZ 01	April-10	3.3326	0.0112	-0.1760	0.0093	-1.7927	-0.8917	0.5284	24.4781	0.4884	0.5602	0.6402		
102 GC AZ 01	April-10	3.1878	0.0120	-0.1654	0.0101	-2.1925	-0.9939	0.5256	24.3249	0.5021	0.5760	0.6560		
102 GC AZ 01	April-10	8.4493	0.0094	-0.0365	0.0090	23.5753	10.3795	-1.6886	31.6241	0.5165	0.5925	0.6725		
102 GC AZ 01	April-10	3.2916	0.0104	-0.1531	0.0092	-2.1030	-1.0272	0.5551	24.3880	0.5121	0.5875	0.6675		
45923	April-10	22.5068	0.0173	0.3114	0.0090	64.6841	27.8357	0.5453	43.1705	0.5585	0.6406	0.7206		
45923	April-10	22.2518	0.0117	0.3292	0.0090	64.5868	27.8556	0.3258	43.1135	0.5819	0.6675	0.7475		
CARRERA MARBLE	April-10	17.6862	0.0261	-0.1032	0.0097	42.4002	18.1079	2.2423	37.1054	0.2488	0.2854	0.3654		
CARRERA MARBLE	April-10	18.1655	0.0113	-0.0982	0.0087	44.1182	19.0909	2.3653	37.4591	0.2434	0.2792	0.3592		
NT 015	May-10	19.1828	0.0080	0.3366	0.0079	65.9220	28.7171	-3.0281	43.3380	0.6303	0.7111	0.7911	0.7980	-4.1
NT 016	May-10	16.7839	0.0082	0.2211	0.0080	63.9932	27.9376	-4.7951	42.7923	0.5717	0.6450	0.7250	0.7328	7.3
NT 016	May-10	17.5865	0.0087	0.2671	0.0094	64.4980	28.1372	-4.1733	42.9373	0.5986	0.6754	0.7554	0.7628	1.9
NT 016	May-10	17.3952	0.0098	0.2491	0.0090	63.3953	27.1520	-4.3084	42.8968	0.5852	0.6602	0.7402	0.7478	4.5
NT 019	May-10	12.4465	0.0082	0.1301	0.0076	56.8373	24.5836	-7.2879	40.9833	0.5838	0.6586	0.7386	0.7462	4.8

NT 019	May-10	12.2522	0.0090	0.1138	0.0090	56.3469	24.3219	-7.3594	40.8746	0.5721	0.6454	0.7254	0.7332	7.2
NT 019	May-10	12.2535	0.0076	0.1345	0.0069	56.8429	24.7064	-7.4291	40.9239	0.5927	0.6687	0.7487	0.7562	3.0
NT 020	May-10	17.5151	0.0089	0.2567	0.0087	60.5126	25.8979	-3.4040	42.1159	0.5899	0.6656	0.7456	0.7531	3.6
NT 020	May-10	17.9501	0.0089	0.2518	0.0082	60.9526	25.9729	-3.1365	42.2934	0.5747	0.6484	0.7284	0.7361	6.7
NT 020	May-10	17.6691	0.0088	0.2669	0.0086	60.8387	25.9315	-3.4031	42.2589	0.5965	0.6729	0.7529	0.7604	2.3
45923	May-10	22.7568	0.0087	0.3822	0.0083	66.1025	29.0188	0.6299	43.2651	0.5910	0.6668	0.7468		
45923	May-10	22.6945	0.0084	0.3677	0.0082	65.7893	28.7448	0.5966	43.2509	0.5779	0.6520	0.7320		
CARRERA MARBLE	May-10	18.1654	0.0089	-0.0966	0.0092	44.3796	19.2216	2.2986	37.5226	0.2212	0.2496	0.3296		
CARRERA MARBLE	May-10	18.1619	0.0096	-0.0748	0.0092	43.6746	18.7395	2.3799	37.4175	0.2431	0.2742	0.3542		
CARRERA MARBLE	May-10	18.2243	0.0089	-0.1013	0.0085	43.4714	18.4027	2.3991	37.4879	0.2151	0.2427	0.3227		
CARRERA MARBLE	May-10	18.2222	0.0084	-0.0779	0.0078	45.2029	20.1007	2.3766	37.4839	0.2385	0.2691	0.3491		
NT 017	July-10	16.5115	0.0101	0.2334	0.0097	57.5415	24.4994	-3.6410	41.3646	0.6003	0.6761	0.7561	0.7895	-2.7
NT 017	July-10	16.5204	0.0092	0.2118	0.0090	57.3946	24.3010	-3.6385	41.3931	0.5785	0.6515	0.7315	0.7618	2.0
NT 017	July-10	16.6438	0.0104	0.2419	0.0103	57.5671	24.4715	-3.5419	41.3915	0.6057	0.6822	0.7622	0.7963	-3.9
NT 006	July-10	12.5838	0.0111	0.1347	0.0099	56.0217	23.7546	-7.1721	41.0025	0.5928	0.6676	0.7476	0.7800	-1.1
NT 006	July-10	12.5775	0.0125	0.1421	0.0109	55.8679	23.6096	-7.1843	41.0004	0.6004	0.6762	0.7562	0.7896	-2.7
NT 006	July-10	12.6660	0.0147	0.1292	0.0103	55.9294	23.5051	-7.1650	41.0838	0.5855	0.6594	0.7394	0.7707	0.5
NT 007	July -10	12.6873	0.0197	0.1287	0.0108	56.6072	23.4735	-7.4975	41.4351	0.5845	0.6583	0.7383	0.7694	0.7
NT 007	July-10	12.7319	0.0154	0.1555	0.0097	57.2628	24.1144	-7.4765	41.4320	0.6102	0.6872	0.7672	0.8020	-4.8
NT 007	July-10	12.6487	0.0113	0.1530	0.0076	57.0266	23.9313	-7.5353	41.4089	0.6097	0.6866	0.7666	0.8013	-4.7
NT 023	July-10	11.1165	0.0116	0.1045	0.0090	53.7416	22.8493	-7.9663	40.3391	0.5967	0.6720	0.7520	0.7849	-2.0
NT 023	July-10	11.0353	0.0095	0.1042	0.0092	53.0380	22.2656	-7.9978	40.2888	0.5983	0.6738	0.7538	0.7869	-2.3
NT 023	July-10	11.0607	0.0107	0.1014	0.0105	53.7114	22.8587	-8.0003	40.3194	0.5950	0.6701	0.7501	0.7827	-1.6
102 GC AZ 01	July-10	2.9856	0.0174	-0.2034	0.0106	-2.7939	-1.2452	0.5543	24.1695	0.4778	0.5381	0.6181		
45923	July-10	21.5692	0.0165	0.3171	0.0110	62.6157	26.6294	-0.0066	42.7699	0.5665	0.6380	0.7180		
45923	July-10	22.1773	0.0338	0.3209	0.0089	63.1122	26.8165	0.4574	42.9174	0.5561	0.6263	0.7063		
CARMEL CHALK	July-10	11.4389	0.0085	0.0153	0.0083	35.5768	15.6774	-2.0731	34.9490	0.5000	0.5631	0.6431		
CARMEL CHALK	July-10	11.4507	0.0113	0.0179	0.0106	34.7876	14.8993	-2.0659	34.9510	0.5024	0.5658	0.6458		
CARMEL CHALK	July-10	11.3842	0.0184	-0.0011	0.0091	34.6696	14.8396	-2.0863	34.9210	0.4850	0.5462	0.6262		
CARRERA MARBLE	July-10	18.0164	0.0171	-0.0880	0.0108	43.2449	18.5665	2.3734	37.2916	0.2439	0.2747	0.3547		
CARRERA MARBLE	July-10	18.0475	0.0105	-0.0694	0.0104	43.0958	18.3862	2.3676	37.3095	0.2618	0.2948	0.3748		
NT 012	September-10	9.3527	0.0095	-0.0240	0.0093	48.0929	18.6703	-8.9515	39.6846	0.5391	0.6032	0.6832	0.7029	13.0
NT 013	September-10	12.9000	0.0101	0.1251	0.0101	53.7629	20.8358	-7.2060	41.3846	0.6151	0.6883	0.7683	0.7932	-3.3
NT 016	September-10	16.3196	0.0088	0.1530	0.0085	57.5599	22.3417	-4.8675	42.4864	0.5727	0.6408	0.7208	0.7428	5.4
NT 016	September-10	16.8338	0.0106	0.1754	0.0101	57.8357	22.3877	-4.4808	42.5981	0.5845	0.6540	0.7340	0.7569	2.9
NT 016	September-10	16.7086	0.0105	0.1965	0.0101	58.8302	23.3819	-4.6131	42.5816	0.6081	0.6804	0.7604	0.7849	-2.0
NT 016	September-10	16.5168	0.0106	0.1826	0.0108	58.1105	22.7991	-4.7359	42.5243	0.5983	0.6694	0.7494	0.7732	0.0
NT 016	September-10	16.4594	0.0103	0.1559	0.0099	58.0752	22.7640	-4.7673	42.5249	0.5727	0.6408	0.7208	0.7429	5.4
NT 016	September-10	16.1942	0.0101	0.1522	0.0099	58.0472	22.8754	-4.9621	42.4545	0.5744	0.6427	0.7227	0.7449	5.1
NT 016	September-10	15.6688	0.0087	0.1358	0.0082	57.5797	22.7069	-5.3344	42.3109	0.5688	0.6365	0.7165	0.7383	6.3
NT 016	September-10	17.0630	0.0105	0.1624	0.0106	59.4628	23.7390	-4.3479	42.7105	0.5668	0.6342	0.7142	0.7359	6.7
NT 016	September-10	16.5688	0.0093	0.1696	0.0084	58.3871	23.0522	-4.6768	42.5316	0.5841	0.6536	0.7336	0.7564	3.0

NT 017	September-10	16.5371	0.0100	0.1590	0.0094	53.8769	20.8837	-3.5615	41.4083	0.5742	0.6425	0.7225	0.7446	5.1
NT 019	September-10	11.7572	0.0095	0.0671	0.0092	51.1525	19.9278	-7.4743	40.5566	0.5807	0.6497	0.7297	0.7523	3.7
NT 019	September-10	12.0048	0.0085	0.1146	0.0084	51.2559	19.8261	-7.3748	40.6596	0.6230	0.6971	0.7771	0.8026	-4.9
NT 019	September-10	11.8383	0.0100	0.0983	0.0099	51.4172	20.1968	-7.4174	40.5503	0.6102	0.6827	0.7627	0.7873	-2.4
NT 019	September-10	11.8697	0.0098	0.0897	0.0091	51.4138	20.1163	-7.4164	40.5899	0.6010	0.6724	0.7524	0.7764	-0.5
NT 019	September-10	11.8608	0.0081	0.0735	0.0079	51.5017	20.1762	-7.4216	40.6026	0.5850	0.6545	0.7345	0.7574	2.8
NT 019	September-10	11.5814	0.0082	0.0559	0.0083	51.5381	20.4281	-7.5770	40.4924	0.5731	0.6412	0.7212	0.7433	5.3
NT 019	September-10	11.4845	0.0092	0.0781	0.0091	51.5381	20.4136	-7.7064	40.5001	0.5973	0.6683	0.7483	0.7720	0.2
NT 019	September-10	11.5184	0.0087	0.0892	0.0086	51.4734	20.3655	-7.6756	40.4926	0.6077	0.6800	0.7600	0.7844	-1.9
NT 007	September-10	12.7405	0.0093	0.0940	0.0091	54.7174	21.6012	-7.4189	41.4665	0.5873	0.6571	0.7371	0.7602	2.3
NT 007	September-10	12.6027	0.0090	0.1240	0.0088	54.3527	21.3566	-7.5344	41.4111	0.6202	0.6939	0.7739	0.7992	-4.3
NT 007	September-10	12.5979	0.0114	0.0880	0.0114	54.3897	21.4086	-7.4936	41.4029	0.5843	0.6537	0.7337	0.7566	3.0
NT 024	September-10	13.2076	0.0091	0.1060	0.0084	53.0818	20.9372	-6.4789	40.9943	0.5897	0.6598	0.7398	0.7630	1.8
NT 024	September-10	13.2983	0.0084	0.1105	0.0083	53.0134	20.7859	-6.4348	41.0375	0.5923	0.6627	0.7427	0.7661	1.3
NT 024	September-10	13.4221	0.0101	0.1360	0.0103	53.4110	21.0800	-6.3819	41.0840	0.6153	0.6884	0.7684	0.7934	-3.4
102 GC AZ 01	September-10	2.9597	0.0080	-0.1998	0.0079	-2.5428	-0.9225	0.5590	24.1183	0.4948	0.5536	0.6336		
45923	September-10	22.0784	0.0096	0.2784	0.0097	58.6715	22.5411	0.4183	42.9208	0.5796	0.6485	0.7285		
45923	September-10	22.0303	0.0090	0.2986	0.0086	58.8857	22.6715	0.3084	42.9601	0.6008	0.6722	0.7522		
45923	September-10	22.3554	0.0099	0.2687	0.0093	59.8257	23.4460	0.6014	43.0276	0.5641	0.6312	0.7112		
CARMEL CHALK	September-10	11.3024	0.0084	-0.0355	0.0082	32.7104	12.8832	-2.1416	34.9504	0.4875	0.5454	0.6254		
CARMEL CHALK	September-10	11.2734	0.0081	-0.0338	0.0077	32.2987	12.6008	-2.1094	34.8884	0.4897	0.5479	0.6279		
CARMEL CHALK	September-10	11.3266	0.0097	-0.0496	0.0092	32.8911	13.0338	-2.1160	34.9641	0.4729	0.5291	0.6091		
CARRERA MARBLE	September-10	17.9175	0.0098	-0.1402	0.0099	40.5811	16.0458	2.3785	37.2611	0.2466	0.2759	0.3559		
CARRERA MARBLE	September-10	17.8768	0.0102	-0.1418	0.0098	40.5237	16.0706	2.3808	37.2196	0.2459	0.2751	0.3551		
NT 014	December-10	13.5725	0.0107	0.1435	0.0103	52.4127	18.9666	-6.8294	41.6709	0.6214	0.6991	0.7791	0.7991	-4.3
NT 014	December-10	9.6418	0.0113	-0.0043	0.0094	46.9956	17.3485	-8.8084	39.8149	0.5527	0.6218	0.7018	0.7235	9.0
NT 015	December-10	18.6215	0.0086	0.2264	0.0082	56.2795	19.8904	-3.2269	43.1034	0.6025	0.6779	0.7579	0.7784	-0.8
NT 030	December-10	13.1703	0.0104	0.1226	0.0105	48.7597	17.0199	-6.3924	40.8544	0.6085	0.6847	0.7647	0.7850	-2.0
NT 030	December-10	12.4964	0.0094	0.0521	0.0095	47.7294	16.4005	-6.8106	40.6606	0.5516	0.6207	0.7007	0.7223	9.2
NT 030	December-10	12.6926	0.0087	0.1206	0.0082	48.7852	17.3026	-6.7443	40.7229	0.6161	0.6932	0.7732	0.7934	-3.4
NT 030	December-10	12.6633	0.0097	0.0907	0.0096	48.4107	16.9741	-6.7253	40.7053	0.5868	0.6603	0.7403	0.7611	2.1
NT 030	December-10	12.7142	0.0087	0.1338	0.0084	48.5109	16.9585	-6.7764	40.7631	0.6289	0.7077	0.7877	0.8075	-5.7
NT 031	December-10	13.4632	0.0082	0.1010	0.0081	48.2329	16.7295	-5.9565	40.7404	0.5810	0.6537	0.7337	0.7547	3.3
NT 031	December-10	13.4501	0.0093	0.0965	0.0092	48.7340	17.1596	-5.9941	40.7690	0.5768	0.6490	0.7290	0.7501	4.1
NT 031	December-10	13.3871	0.0106	0.1025	0.0102	48.8622	17.4358	-5.9859	40.6913	0.5841	0.6572	0.7372	0.7581	2.7
NT 031	December-10	13.3699	0.0095	0.1352	0.0093	48.8641	17.4273	-6.1279	40.6998	0.6171	0.6943	0.7743	0.7944	-3.5
NT 031	December-10	13.3294	0.0081	0.0905	0.0079	48.3313	16.9300	-6.0278	40.6868	0.5732	0.6450	0.7250	0.7461	4.8
NT 031	December-10	13.6864	0.0096	0.1288	0.0094	48.8218	17.1505	-5.8353	40.8169	0.6043	0.6799	0.7599	0.7803	-1.2
NT 032	December-10	17.5139	0.0095	0.1690	0.0094	53.3984	18.3424	-3.6541	42.4715	0.5674	0.6384	0.7184	0.7397	6.0
NT 032	December-10	17.4767	0.0094	0.1405	0.0095	53.6064	18.5504	-3.6593	42.4681	0.5397	0.6072	0.6872	0.7092	11.8
NT 032	December-10	17.6603	0.0092	0.2129	0.0091	54.5984	19.3342	-3.6378	42.5575	0.6083	0.6845	0.7645	0.7848	-1.9
NT 032	December-10	17.6070	0.0097	0.2197	0.0095	54.5393	19.3776	-3.6473	42.5060	0.6162	0.6934	0.7734	0.7935	-3.4
NT 012	December-10	9.7513	0.0090	-0.0214	0.0086	46.0164	16.3437	-8.7065	39.8421	0.5334	0.6002	0.6802	0.7023	13.1
NT 012	December-10	9.5236	0.0088	-0.0037	0.0088	46.0222	16.5435	-8.8569	39.7431	0.5557	0.6252	0.7052	0.7268	8.4

NT 014	December-10	13.3426	0.0092	0.1512	0.0089	51.6131	18.4146	-6.9568	41.5573	0.6336	0.7129	0.7929	0.8127	-6.5
NT 015	December-10	18.5675	0.0091	0.2244	0.0088	56.2006	19.8304	-3.2715	43.0951	0.6016	0.6769	0.7569	0.7774	-0.7
45923	December-10	22.3602	0.0091	0.2442	0.0088	55.5144	19.1528	0.5641	43.0941	0.5450	0.6132	0.6932		
45923	December-10	22.5466	0.0102	0.2989	0.0100	56.6689	20.1291	0.6251	43.1650	0.5959	0.6705	0.7505		
45923	December-10	22.3900	0.0095	0.2810	0.0090	56.1402	19.6824	0.5175	43.1326	0.5811	0.6539	0.7339		
CARRERA MARBLE	December-10	18.0107	0.0097	-0.1827	0.0094	38.0786	13.3443	2.3828	37.3933	0.2057	0.2315	0.3115		
CARRERA MARBLE	December-10	17.9624	0.0090	-0.2090	0.0087	37.7671	13.1202	2.4028	37.3521	0.1804	0.2030	0.2830		
CARRERA MARBLE	December-10	18.0128	0.0093	-0.1705	0.0094	38.3951	13.6735	2.3828	37.3830	0.2178	0.2451	0.3251		
CARRERA MARBLE	December-10	18.0048	0.0086	-0.1654	0.0080	38.3530	13.6999	2.4046	37.3481	0.2231	0.2510	0.3310		
CARRERA MARBLE	December-10	17.9825	0.0104	-0.1395	0.0099	38.3986	13.8339	2.4019	37.3024	0.2495	0.2807	0.3607		
NT 012	February-11	10.0859	0.0109	-0.0885	0.0100	40.2082	10.3465	-8.5193	40.0543	0.5804	0.6328	0.7128	0.7234	9.0
NT 012	February-11	9.6742	0.0087	-0.1133	0.0085	39.8487	10.2374	-8.7895	39.9311	0.5599	0.6105	0.6905	0.6999	13.6
NT 012	February-11	9.7463	0.0106	-0.0930	0.0101	40.2167	10.5507	-8.7598	39.9538	0.5794	0.6318	0.7118	0.7223	9.3
NT 012	February-11	9.6031	0.0108	-0.0920	0.0100	40.0035	10.5141	-8.8183	39.8661	0.5819	0.6346	0.7146	0.7252	8.7
NT 032	February-11	16.7781	0.3246	0.0301	0.0132	46.5807	12.0532	-3.5986	42.6299	0.6283	0.6852	0.7652	0.7784	-0.8
NT 032	February-11	17.4946	0.0090	0.0390	0.0085	47.1295	12.1232	-3.6621	42.5839	0.6297	0.6867	0.7667	0.7800	-1.1
NT 032	February-11	17.5677	0.0097	0.0365	0.0095	46.7588	11.6366	-3.6524	42.6500	0.6265	0.6831	0.7631	0.7762	-0.5
NT 032	February-11	17.4828	0.0099	0.0319	0.0094	47.2823	12.2283	-3.6894	42.6060	0.6227	0.6790	0.7590	0.7719	0.3
45923	February-11	22.2565	0.0087	0.0692	0.0087	48.0056	11.7301	0.5103	43.2135	0.6097	0.6648	0.7448		
CARRERA MARBLE	February-11	18.0290	0.0127	-0.3227	0.0112	33.4163	8.5016	2.3535	37.5735	0.2624	0.2861	0.3661		
CARRERA MARBLE	February-11	18.0184	0.0112	-0.3328	0.0098	33.8686	8.9271	2.3449	37.5819	0.2524	0.2753	0.3553		
CARRERA MARBLE	February-11	18.0379	0.0113	-0.1088	0.0109	39.7288	15.0239	2.3695	37.3581	0.4762	0.5193	0.5993		
TV01	February-11	11.3254	0.0084	-0.0897	0.0079	14.6117	3.7987	2.5028	30.4878	0.5661	0.6173	0.6973		
TV01	February-11	11.3236	0.0113	-0.1288	0.0101	15.0068	4.0605	2.4735	30.5541	0.5270	0.5746	0.6546		
NT 012	April-11	9.9732	0.0099	0.0327	0.0099	65.2537	34.9888	-8.5591	39.8650	0.5991	0.5980	0.6780	0.7124	11.2
NT 014	April-11	13.1407	0.0108	0.1785	0.0110	72.7511	39.1539	-7.0545	41.4228	0.6558	0.6545	0.7345	0.7744	-0.2
NT 014	April-11	13.6076	0.0119	0.1924	0.0114	73.1311	39.0107	-6.8519	41.6788	0.6567	0.6554	0.7354	0.7753	-0.3
NT 014	April-11	13.3026	0.0135	0.1476	0.0126	73.4421	39.6319	-6.9545	41.5185	0.6204	0.6191	0.6991	0.7356	6.8
NT 014	April-11	13.2890	0.0115	0.1471	0.0111	71.8669	38.2070	-6.9166	41.4680	0.6203	0.6190	0.6990	0.7355	6.8
NT 014	April-11	17.8542	0.0147	-0.0973	0.0136	52.2669	27.5454	2.3150	37.2160	0.2475	0.2470	0.3270	0.3279	139.3
NT 015	April-11	18.9526	0.0096	0.3400	0.0094	81.0040	43.6584	-3.0606	43.1553	0.6538	0.6525	0.7325	0.7722	0.2
NT 015	April-11	18.4143	0.0127	0.3498	0.0122	80.1896	43.3589	-3.3719	42.9123	0.6788	0.6775	0.7575	0.7995	-4.4
NT 015	April-11	18.8593	0.0102	0.3486	0.0097	79.1007	42.0529	-3.0464	43.0390	0.6651	0.6638	0.7438	0.7845	-1.9
NT 015	April-11	18.5192	0.0127	0.3543	0.0118	79.6495	42.7158	-3.3314	42.9730	0.6804	0.6790	0.7590	0.8012	-4.7
NT 018	April-11	15.1693	0.0094	0.2238	0.0088	73.0780	39.8722	-4.8271	41.2164	0.6441	0.6428	0.7228	0.7615	2.1
NT 018	April-11	15.3413	0.0129	0.2216	0.0123	72.9436	39.7072	-4.6670	41.2335	0.6371	0.6358	0.7158	0.7539	3.4
NT 018	April-11	12.5918	0.0120	0.1300	0.0112	66.2062	34.3845	-6.7630	40.6304	0.6228	0.6215	0.7015	0.7382	6.3
NT 030	April-11	12.6858	0.0101	0.1843	0.0096	70.1282	38.1366	-6.7503	40.6568	0.6744	0.6731	0.7531	0.7947	-3.6
NT 030	April-11	12.6011	0.0104	0.1822	0.0102	70.6186	38.6850	-6.7975	40.6206	0.6748	0.6734	0.7534	0.7951	-3.7
NT 030	April-11	12.6704	0.0123	0.1706	0.0117	68.3107	36.5891	-6.6419	40.5481	0.6612	0.6599	0.7399	0.7802	-1.2
45923	April-11	22.3721	0.0144	0.4097	0.0136	77.7985	40.8873	0.5154	42.9846	0.6274	0.6262	0.7062		
45924	April-11	22.2118	0.0092	0.4181	0.0088	80.0823	43.0951	0.3446	42.9841	0.6403	0.6391	0.7191		

45925	April-11	22.9073	0.0087	0.4208	0.0081	81.0087	43.5318	0.8169	43.2119	0.6235	0.6223	0.7023		
CARMEL CHALK	April-11	11.4073	0.0132	-0.0045	0.0126	42.8289	22.8077	-2.0659	34.9504	0.5216	0.5206	0.6006		
CARRERA MARBLE	April-11	17.9981	0.0094	-0.0473	0.0092	53.6301	28.7796	2.3601	37.2648	0.2934	0.2928	0.3728		
CARRERA MARBLE	April-11	18.0488	0.0101	-0.0770	0.0100	53.8107	28.8174	2.3715	37.3348	0.2623	0.2618	0.3418		
CARRERA MARBLE	April-11	18.0342	0.0109	-0.0926	0.0106	52.4764	27.5170	2.3741	37.3335	0.2472	0.2467	0.3267		
CARRERA MARBLE	April-11	17.5697	0.0089	-0.0771	0.0085	51.8898	27.5889	2.2156	37.0081	0.2757	0.2751	0.3551		
TV01	April-11	11.3187	0.0116	0.0299	0.0113	22.6202	11.8971	2.5036	30.3684	0.5585	0.5574	0.6374		
TV01	April-11	11.1381	0.0119	0.0294	0.0113	22.6379	12.1287	2.4303	30.2595	0.5631	0.5620	0.6420		
NT 012	September-11	12.6621	0.0084	0.1373	0.0082	56.6058	24.2974	-7.1238	41.0839	0.7104	0.7137	0.7937	0.8172	-7.2
NT 012	September-11	11.9269	0.0074	0.1021	0.0072	55.4389	23.4195	-7.7073	40.9564	0.6907	0.6939	0.7739	0.7951	-3.7
NT 013	September-11	18.8498	0.0101	0.2719	0.0096	63.8077	27.1232	-3.0868	43.1806	0.7139	0.7171	0.7971	0.8211	-7.9
NT 013	September-11	13.7802	0.0088	0.1326	0.0087	58.7062	25.2659	-6.5268	41.6248	0.6820	0.6851	0.7651	0.7853	-2.0
NT 013	September-11	12.9658	0.0104	0.1063	0.0099	55.2360	22.7550	-6.8923	41.1926	0.6729	0.6760	0.7560	0.7751	-0.3
NT 013	September-11	12.5919	0.0084	0.0878	0.0079	56.5262	24.0878	-7.2121	41.1515	0.6623	0.6654	0.7454	0.7632	1.8
NT 013	September-11	12.2790	0.0100	0.0768	0.0096	55.3178	23.3484	-7.2979	40.9318	0.6580	0.6610	0.7410	0.7583	2.6
NT 013	September-11	12.2603	0.0127	0.0732	0.0120	54.9967	23.0351	-7.3144	40.9325	0.6548	0.6578	0.7378	0.7547	3.3
NT 013	September-11	16.4930	0.0093	0.1660	0.0089	60.4187	25.1302	-4.7181	42.5329	0.6579	0.6609	0.7409	0.7582	2.7
NT 013	September-11	12.5995	0.0120	0.0771	0.0113	55.9964	23.6570	-7.1510	41.1091	0.6515	0.6545	0.7345	0.7510	4.0
NT 013	September-11	16.9540	0.0092	0.1664	0.0090	61.3194	25.6725	-4.4179	42.6993	0.6485	0.6515	0.7315	0.7476	4.6
NT 013	September-11	16.6990	0.0083	0.1398	0.0079	61.2595	25.8285	-4.5399	42.5905	0.6273	0.6301	0.7101	0.7237	9.0
NT 020	September-11	14.5559	0.4273	0.1490	0.0140	58.1793	25.0378	-5.6073	41.4780	0.6819	0.6851	0.7651	0.7852	-2.0
NT 020	September-11	17.4042	0.2822	0.2518	0.0104	60.2664	25.6305	-3.5439	42.2001	0.7244	0.7277	0.8077	0.8329	-9.7
NT 007	September-11	12.6860	0.0096	0.1035	0.0090	57.3689	24.1364	-7.5280	41.5429	0.6761	0.6792	0.7592	0.7787	-0.9
45923	September-11	22.8291	0.0111	0.2913	0.0105	63.1518	26.2163	0.8051	43.3110	0.6489	0.6519	0.7317		
45924	September-11	22.9039	0.0112	0.3193	0.0106	65.5247	28.4314	0.8135	43.3491	0.6753	0.6784	0.7583		
45925	September-11	23.9871	0.0097	0.2010	0.0092	64.8294	27.9882	0.5865	43.2340	0.5340	0.5365	0.6165		
CARRERA MARBLE	September-11	17.9510	0.0101	-0.1932	0.0097	43.6186	18.8680	2.3659	37.3938	0.2678	0.2690	0.3489		
CARRERA MARBLE	September-11	17.8912	0.0104	-0.2003	0.0097	43.0360	18.3859	2.3573	37.3495	0.2619	0.2631	0.3431		
CARRERA MARBLE	September-11	18.6397	0.2192	-0.0936	0.0241	46.2773	19.9230	2.1738	38.1698	0.3528	0.3544	0.4343		
CARRERA MARBLE	September-11	17.9951	0.0088	-0.1791	0.0087	43.3756	18.5783	2.3691	37.4206	0.2809	0.2822	0.3621		
TV01	September-11	11.5029	0.0098	0.0260	0.0094	20.0074	9.1565	2.5881	30.5073	0.6236	0.6265	0.7064		
TV01	September-11	11.4582	0.0096	0.0320	0.0093	19.8296	8.9847	2.5379	30.5053	0.6306	0.6335	0.7134		
NT 023	October-11	10.8268	0.0099	-0.1661	0.0107	33.8010	3.3037	-8.1025	40.5090	0.7029	0.6740	0.7540	0.7861	-2.2
NT 023	October-11	13.0399	0.0098	-0.1680	0.0097	35.4629	3.6096	-6.5260	41.1833	0.6984	0.6697	0.7497	0.7813	-1.3
NT 023	October-11	13.1265	0.0087	-0.1857	0.0096	35.7491	3.7584	-6.4871	41.2499	0.6806	0.6527	0.7327	0.7623	1.9
NT 023	October-11	10.8201	0.0074	-0.1837	0.0088	33.6907	3.2189	-8.0791	40.4973	0.6853	0.6571	0.7371	0.7673	1.1
NT 023	October-11	11.0534	0.0084	-0.1642	0.0096	33.6778	3.0666	-7.9345	40.5695	0.7045	0.6756	0.7556	0.7878	-2.4
NT 024	October-11	13.0565	0.0094	-0.1620	0.0105	35.6261	3.7446	-6.5275	41.1954	0.7044	0.6755	0.7555	0.7877	-2.4
NT 024	October-11	13.0827	0.0084	-0.1487	0.0082	36.3380	4.4489	-6.5069	41.1876	0.7176	0.6882	0.7682	0.8019	-4.8

45923	October-11	22.2340	0.0101	-0.2109	0.0095	40.0647	3.9718	0.7401	43.2919	0.6449	0.6184	0.6984		
45923	October-11	22.3402	0.0082	-0.1984	0.0085	40.0532	3.7186	0.7071	43.4176	0.6572	0.6302	0.7102		
CARRERA MARBLE	October-11	17.4551	0.0073	-0.5863	0.0081	25.7411	1.5143	2.3178	37.3431	0.2750	0.2637	0.3437		
CARRERA MARBLE	October-11	17.5486	0.0082	-0.6056	0.0085	26.2415	1.8531	2.3543	37.4209	0.2555	0.2451	0.3251		
CARRERA MARBLE	October-11	17.5788	0.0107	-0.5132	0.0098	27.3632	3.0469	2.3410	37.3698	0.3480	0.3337	0.4137		
CARRERA MARBLE	October-11	17.5096	0.0088	-0.5782	0.0107	27.5658	3.2432	2.3371	37.3706	0.2830	0.2714	0.3514		
CARRERA MARBLE	October-11	17.4110	0.0098	-0.5414	0.0171	28.7942	4.6604	2.3129	37.2583	0.3199	0.3068	0.3868		
TV01	October-11	11.0985	0.0086	-0.2520	0.0103	12.2499	1.4094	2.4200	30.5453	0.6167	0.5914	0.6714		
TV01	October-11	11.1803	0.0102	-0.2719	0.0104	11.8897	0.9815	2.4871	30.5820	0.5966	0.5721	0.6521		
NT 030	November-11	12.6919	0.0105	-0.0024	0.0103	39.5846	8.3509	-6.6521	40.7571	0.6362	0.6836	0.7636	0.7807	1.7
NT 030	November-11	11.7684	0.0083	0.0272	0.0082	39.7401	9.5029	-7.1028	40.2413	0.6765	0.7270	0.8070	0.8211	-5.6
NT 030	November-11	11.8886	0.0095	-0.0129	0.0090	39.5798	9.1675	-7.0321	40.3341	0.6350	0.6824	0.7624	0.7795	1.9
NT 030	November-11	11.8422	0.0106	-0.0316	0.0102	39.2909	8.9399	-7.0326	40.3066	0.6168	0.6629	0.7429	0.7614	5.4
NT 030	November-11	11.8313	0.0095	-0.0480	0.0094	39.6081	9.2043	-7.0496	40.3293	0.6006	0.6454	0.7254	0.7451	8.7
45923	November-11	22.3285	0.0097	0.0391	0.0092	45.3963	9.2367	0.6484	43.1899	0.5652	0.6074	0.6874		
CARRERA MARBLE	November-11	17.7672	0.0101	-0.3867	0.0095	30.8744	6.3802	2.3621	37.3781	0.1927	0.2071	0.2871		
CARRERA MARBLE	November-11	17.7456	0.0089	-0.3939	0.0084	30.7422	6.3116	2.3797	37.3469	0.1857	0.1995	0.2795		
CARRERA MARBLE	November-11	17.7518	0.0102	-0.3640	0.0100	31.0032	6.6086	2.3770	37.3253	0.2155	0.2316	0.3116		
CARRERA MARBLE	November-11	17.7518	0.0102	-0.3640	0.0100	31.0032	6.6086	2.3770	37.3253	0.2155	0.2316	0.3116		
CARRERA MARBLE	November-11	17.5860	0.0091	-0.3639	0.0081	30.8404	6.7184	2.3490	37.1865	0.2176	0.2338	0.3138		
TV01	November-11	11.1954	0.0090	-0.1491	0.0082	13.3828	2.7569	2.5431	30.3883	0.5069	0.5448	0.6248		
TV01	November-11	11.2988	0.0105	-0.1220	0.0105	13.6008	2.9446	2.6067	30.4024	0.5328	0.5726	0.6526		
TV01	November-11	11.0942	0.0086	-0.1608	0.0088	13.3247	2.9014	2.5581	30.2843	0.4964	0.5334	0.6134		
TV01	November-11	11.2704	0.0075	-0.0740	0.0070	14.3850	3.8301	2.5853	30.3464	0.5811	0.6245	0.7045		
NT 030	January-12	12.0863	0.0094	-0.0188	0.0082	42.5035	11.7772	-6.9431	40.4513	0.5564	0.6535	0.7335	0.7325	7.3
NT 030	January-12	12.1535	0.0099	0.0296	0.0093	42.7352	11.9813	-6.9354	40.4620	0.6040	0.7095	0.7895	0.7884	-2.5
NT 030	January-12	11.9847	0.0082	0.0073	0.0079	42.5622	11.8976	-7.0409	40.4190	0.5837	0.6857	0.7657	0.7646	1.5
NT 030	January-12	11.8485	0.0077	-0.0030	0.0069	42.4258	11.9107	-7.0936	40.3443	0.5751	0.6755	0.7555	0.7545	3.3
NT 030	January-12	11.9682	0.0095	0.0124	0.0084	42.8592	12.2821	-7.0128	40.3696	0.5890	0.6918	0.7718	0.7708	0.5
NT 030	January-12	12.0016	0.0119	0.0153	0.0101	42.7668	12.1249	-7.0171	40.4041	0.5916	0.6949	0.7749	0.7738	-0.1
NT 030	January-12	12.0675	0.0078	0.0387	0.0077	43.2609	12.5897	-6.9816	40.4116	0.6141	0.7214	0.8014	0.8003	-4.5
45923	January-12	22.9425	0.0095	0.1340	0.0089	50.7253	14.0975	1.0264	43.3351	0.5795	0.6807	0.7607		
CARMEL CHALK	January-12	11.3532	0.0096	-0.1189	0.0092	27.5098	7.6940	-2.0694	35.0159	0.4651	0.5464	0.6264		
CARRERA MARBLE	January-12	17.8568	0.0084	-0.2704	0.0082	34.5584	10.0435	2.3678	37.3439	0.2359	0.2771	0.3571		
TV01	January-12	11.3832	0.0098	-0.0782	0.0086	15.1171	4.3202	2.5820	30.4666	0.5054	0.5937	0.6737		
TV01	January-12	11.2733	0.0107	-0.0967	0.0088	15.0897	4.3511	2.5186	30.4369	0.4882	0.5735	0.6535		

Table 4.4 Heated Gases

Date	d47	d47 stdev	D47	D47 stderr	d48	D48	D48 stdev
April-10	28.567	0.060	-0.116	0.012	128.971	53.513	0.880
April-10	-4.799	0.103	-0.851	0.007	10.199	4.099	0.300
April-10	-3.958	0.075	-0.817	0.012	12.273	5.179	0.205
April-10	27.925	0.014	-0.132	0.011	125.961	52.129	0.633
April-10	-2.320	0.015	-0.786	0.011	18.606	7.996	0.272
April-10	25.145	0.035	-0.180	0.013	116.299	48.616	0.684
April-10	-4.942	0.035	-0.826	0.008	8.749	3.648	0.123
April-10	-3.127	0.032	-0.822	0.015	15.518	6.541	0.174
April-10	26.648	0.020	-0.163	0.008	120.466	49.515	0.388
May-10	24.335	0.064	-0.146	0.011	114.441	48.778	1.788
May-10	-3.406	0.076	-0.807	0.010	15.045	6.604	0.348
May-10	23.563	0.074	-0.199	0.010	110.968	46.609	1.288
May-10	-3.449	0.060	-0.852	0.009	14.713	6.325	0.306
May-10	22.432	0.059	-0.234	0.007	107.796	46.056	1.147
July-10	27.648	0.021	-0.088	0.008	124.692	51.808	1.170
July-10	-3.422	0.016	-0.812	0.013	15.457	6.714	0.283
July-10	26.276	0.029	-0.125	0.013	120.198	50.105	0.784
July-10	26.985	0.017	-0.163	0.012	119.701	48.283	0.829
July-10	-3.214	0.017	-0.844	0.010	15.559	6.661	0.434
July-10	9.669	0.016	-0.526	0.013	58.398	23.681	0.485
July-10	20.978	0.031	-0.257	0.012	100.124	41.812	0.656
September-10	25.103	0.016	-0.253	0.010	108.100	40.484	0.911
September-10	27.447	0.028	-0.232	0.010	115.565	43.145	0.976
September-10	26.634	0.016	-0.230	0.008	112.780	42.406	0.845
September-10	-2.279	0.013	-0.826	0.017	18.063	7.068	0.262
September-10	24.881	0.017	-0.239	0.011	106.959	40.621	0.607
September-10	25.589	0.015	-0.209	0.007	110.951	42.162	0.990
September-10	27.411	0.012	-0.199	0.015	116.367	44.196	0.915
September-10	-4.113	0.015	-0.808	0.012	11.797	4.757	0.157
September-10	25.289	0.011	-0.178	0.013	113.819	45.903	1.441
September-10	-3.359	0.022	-0.849	0.011	14.626	5.887	0.308
September-10	25.927	0.027	-0.218	0.019	112.601	43.413	0.593
September-10	-3.584	0.013	-0.820	0.015	13.758	5.658	0.288
September-10	25.952	0.021	-0.215	0.015	112.566	43.296	0.480
December-10	-3.092	0.017	-0.811	0.011	13.460	4.568	0.261
December-10	26.004	0.013	-0.236	0.013	104.155	34.756	0.327
December-10	-2.776	0.016	-0.823	0.020	14.379	4.859	0.364
December-10	16.299	0.016	-0.430	0.007	74.174	25.707	0.338
December-10	-3.621	0.032	-0.809	0.009	12.440	4.505	0.149
December-10	27.337	0.012	-0.203	0.015	108.433	36.778	0.263
December-10	27.086	0.009	-0.205	0.015	107.918	36.768	0.284
December-10	27.170	0.018	-0.193	0.004	109.105	37.500	0.260
December-10	27.233	0.014	-0.201	0.010	108.943	37.282	0.417
December-10	26.529	0.015	-0.213	0.009	107.290	36.959	0.131
February-11	-2.471	0.010	-0.792	0.009	13.670	3.592	0.567
February-11	24.096	0.022	-0.498	0.014	86.004	21.225	0.407
February-11	24.286	0.024	-0.505	0.012	85.813	20.701	0.492
February-11	-5.078	0.027	-0.833	0.010	7.210	2.027	0.263
February-11	-2.977	0.019	-0.784	0.013	12.135	3.031	0.282
February-11	25.440	0.019	-0.523	0.009	89.775	22.197	0.391
February-11	-3.972	0.023	-0.845	0.013	9.732	2.190	0.331
February-11	26.498	0.024	-0.516	0.014	92.313	22.410	0.377
April-11	-3.676	0.018	-0.955	0.014	16.676	8.185	0.903
April-11	27.087	0.017	-0.076	0.014	151.726	77.566	1.352
April-11	18.498	0.028	-0.318	0.016	114.863	60.253	1.767

April-11	19.757	0.033	-0.292	0.020	118.608	61.650	1.266
April-11	20.226	0.013	-0.283	0.016	123.199	65.321	1.711
April-11	-3.062	0.017	-0.938	0.012	18.875	9.894	1.187
April-11	-3.215	0.026	-0.924	0.015	18.823	9.504	1.042
April-11	17.870	0.020	-0.354	0.013	113.079	59.771	1.029
April-11	17.552	0.027	-0.359	0.019	109.589	57.139	1.781
September-11	17.458	0.023	-0.484	0.011	87.032	35.636	1.125
September-11	17.630	0.011	-0.491	0.010	88.168	36.380	0.825
September-11	15.501	0.020	-0.538	0.013	83.001	33.837	0.969
September-11	24.189	0.016	-0.289	0.014	110.991	45.515	1.020
September-11	-3.837	0.020	-0.973	0.009	14.410	6.543	1.412
September-11	23.195	0.012	-0.353	0.009	105.207	41.843	0.745
September-11	19.367	0.009	-0.466	0.013	91.771	37.119	0.939
September-11	20.623	0.022	-0.360	0.022	103.382	44.175	3.177
September-11	-4.886	0.027	-0.911	0.012	9.964	3.577	0.775
September-11	15.635	0.016	-0.490	0.017	81.408	33.030	0.931
September-11	-3.619	0.024	-0.933	0.007	16.035	7.104	1.084
September-11	-5.129	0.020	-0.942	0.013	9.207	3.557	0.661
September-11	23.159	0.022	-0.353	0.017	107.511	43.499	1.064
September-11	-6.663	0.015	-0.953	0.019	4.796	1.636	0.922
September-11	22.231	0.012	-0.380	0.011	104.243	42.334	0.736
October-11	21.707	0.015	-0.836	0.014	64.174	4.887	0.693
October-11	22.325	0.016	-0.873	0.016	65.802	5.069	0.547
October-11	21.520	0.040	-0.853	0.018	64.131	5.206	0.660
October-11	21.381	0.005	-0.863	0.018	63.860	5.176	0.766
October-11	-2.800	0.018	-0.889	0.012	10.812	0.722	0.578
October-11	-2.984	0.019	-0.887	0.017	10.373	0.601	0.619
October-11	-2.921	0.020	-0.879	0.015	11.162	1.327	0.526
November-11	18.125	7.324	-0.550	0.013	71.631	14.407	0.258
November-11	-3.458	0.029	-0.819	0.013	10.749	2.218	0.175
November-11	-2.847	0.044	-0.829	0.014	12.221	2.456	0.100
November-11	19.308	0.039	-0.550	0.014	68.169	14.040	0.323
November-11	20.802	0.034	-0.578	0.014	72.591	15.125	0.250
November-11	15.406	0.026	-0.622	0.010	58.119	12.216	0.126
November-11	20.695	0.013	-0.533	0.006	72.447	15.391	0.232
November-11	-3.400	0.029	-0.825	0.006	11.196	2.382	0.258
January-12	-5.997	0.020	-0.793	0.008	4.843	1.504	0.373
January-12	24.612	0.037	-0.402	0.014	89.322	23.851	0.270
January-12	27.002	9.547	-0.404	0.013	96.456	25.862	0.215
January-12	-3.869	0.026	-0.742	0.009	10.054	3.001	0.326
January-12	26.538	0.029	-0.417	0.010	94.898	24.860	0.157
January-12	-3.563	0.030	-0.785	0.011	10.756	2.963	0.248

Table 4.5 Corals Displaying Vital Effects

name	d47	D47	d48	D48	d13C	d18O	Standard Corrected D47	T	
NT 018	15.63132	0.186437	58.88185	25.51586	-4.63575	41.51038	0.74681058	4.704097	
NT 018	15.39448	0.192188	58.27079	25.1616	-4.761	41.38975	0.75973821	2.391137	
NT 018	15.16933	0.223778	73.07797	39.87223	-4.82713	41.21638	0.7615392	2.073473	
NT 018	15.34129	0.221621	72.94356	39.70716	-4.667	41.2335	0.75389262	3.429828	
NT 018	12.59185	0.129974	66.20617	34.38449	-6.763	40.63038	0.73824471	6.269145	displays Vital Effect
NT 012	12.66207	0.137344	56.60584	24.2974	-7.12375	41.08388	0.81723665	-7.23873	
NT 012	11.92694	0.102082	55.43887	23.41951	-7.70725	40.95638	0.79510827	-3.65345	
NT 012	13.61496	0.172114	58.47579	25.41241	-6.52925	41.36725	0.78184756	-1.43417	
NT 012	13.85587	0.150584	58.27658	25.03667	-6.35525	41.45988	0.75010847	4.108521	
NT 012	13.74895	0.146518	58.35912	25.16717	-6.434	41.43425	0.74804622	4.480499	
NT 012	9.352701	-0.02395	48.09286	18.67026	-8.9515	39.68463	0.70293999	13.01053	displays Vital Effect
NT 012	10.08594	-0.08848	40.20823	10.34648	-8.51925	40.05425	0.72337957	9.049046	displays Vital Effect
NT 012	9.6742	-0.11327	39.8487	10.23738	-8.7895	39.93113	0.69994756	13.60462	displays Vital Effect
NT 012	9.746315	-0.093	40.21668	10.55068	-8.75975	39.95375	0.72230748	9.252759	displays Vital Effect
NT 012	9.603088	-0.09199	40.00354	10.51414	-8.81825	39.86613	0.72519396	8.70529	displays Vital Effect
NT 012	9.973165	0.032681	65.2537	34.9888	-8.55913	39.865	0.71240277	11.1559	displays Vital Effect
NT 012	9.751269	-0.0214	46.01635	16.34367	-8.7065	39.84213	0.70228525	13.1402	displays Vital Effect
NT 012	9.523557	-0.00371	46.02221	16.54354	-8.85688	39.74313	0.72681455	8.39931	displays Vital Effect
NT 014	14.15176	0.173341	60.82013	26.44655	-6.61838	41.99563	0.76945394	0.690359	
NT 014	14.11915	0.161277	60.42125	26.08135	-6.6285	41.985	0.75599303	3.055259	
NT 014	13.75872	0.139085	59.3339	25.41925	-6.70613	41.82188	0.73898241	6.13332	
NT 014	13.57255	0.143543	52.41274	18.96659	-6.82938	41.67088	0.79913414	-4.31653	
NT 014	13.14066	0.178453	72.75109	39.15385	-7.0545	41.42275	0.77437003	-0.15831	
NT 014	13.6076	0.192435	73.13108	39.01066	-6.85188	41.67875	0.77529744	-0.31753	
NT 014	13.30258	0.147566	73.44214	39.63194	-6.9545	41.5185	0.73562198	6.753651	
NT 014	13.28895	0.147076	71.86689	38.20698	-6.91663	41.468	0.73550516	6.77529	
NT 014	9.64182	-0.00433	46.99558	17.34848	-8.80838	39.81488	0.72350563	9.025123	displays Vital Effect
NT 014	13.34258	0.151188	51.61309	18.41459	-6.95675	41.55725	0.81265527	-6.5082	

Table 4.6-14C Dates

UCIAMS	Sample Name	Fm	±	D14C	±	14C age	±
94283	14C-NT-002	0.246821	0.000797	-753.179	0.796519	11240	30
94294	14C-NT-006	0.159514	0.000746	-840.486	0.745506	14745	40
94295	14C-NT-007	0.16904	0.000713	-830.96	0.712631	14280	35
94297	14C-NT-010	0.246049	0.000752	-753.951	0.752397	11265	25
94298	14C-NT-012	0.169699	0.000712	-830.301	0.712215	14250	35
94299	14C-NT-013	0.171814	0.000777	-828.186	0.777304	14150	40
94300	14C-NT-014	0.169222	0.000761	-830.778	0.761363	14270	40
94301	14C-NT-015	0.165354	0.000751	-834.646	0.750784	14455	40
94302	14C-NT-016	0.167163	0.000726	-832.837	0.726462	14370	35
94303	14C-NT-017	0.269392	0.000946	-730.608	0.946269	10535	30
94304	14C-NT-018	0.255347	0.0008	-744.653	0.799811	10965	30
94306	14C-NT-020	0.244856	0.000785	-755.144	0.785297	11305	30
94307	14C-NT-030	0.254247	0.000806	-745.753	0.805702	11000	30
94308	14C-NT-031	0.20836	0.000784	-791.64	0.783763	12600	35
94309	14C-NT-032.	0.179448	0.000793	-820.552	0.793096	13800	40

Table 4.7-U-Series Age determination for Corals

ID	U238 conc ppb	Error	232 Th pmol/g	Error	d234U(T)	Error	230Th/238U	Corrected Age	Error	d234U initial
U-NT002	3396.39	0.64	1.31	0.57	142.90	0.45	0.12	12244	42	147.9336
U-NT006	3569.01	0.84	5.98	0.73	148.35	0.55	0.17	17739	178	155.9805
U-NT007	3448.81	0.84	3.30	0.75	146.65	0.46	0.15	15638	102	153.2785
U-NT010	3072.02	0.90	0.22	0.89	143.94	0.45	0.12	12104	10	148.949
U-NT012	3588.71	0.58	3.79	0.46	145.59	0.45	0.15	15487	113	152.1037
U-NT013	3542.14	0.91	17.39	0.81	146.23	0.39	0.16	15560	527	152.8013
U-NT014	3512.94	0.72	8.85	0.63	144.90	0.41	0.16	16107	270	151.6499
U-NT015	4724.64	1.00	5.12	0.00	139.34	0.40	0.17	17228	116	146.2889
U-NT016	5287.18	4.20	3.93	0.03	142.14	0.45	0.15	15154	80	148.363
U-NT017	3907.84	7.29	25.66	0.09	145.24	0.81	0.12	11773	708	150.1589
U-NT018	5149.60	5.09	20.13	0.04	143.77	0.54	0.14	13870	420	149.5148
U-NT020	4463.25	3.56	4.69	0.03	142.91	0.52	0.12	12168	113	147.9122
U-NT030	3611.69	4.59	23.60	0.06	143.61	0.65	0.12	11889	705	148.5139
U-NT031	3482.02	4.31	2.55	0.05	155.06	0.68	0.16	15698	78	162.0975
U-NT-032	4075.44	3.01	6.79	0.03	147.30	0.45	0.15	15495	178	153.8901

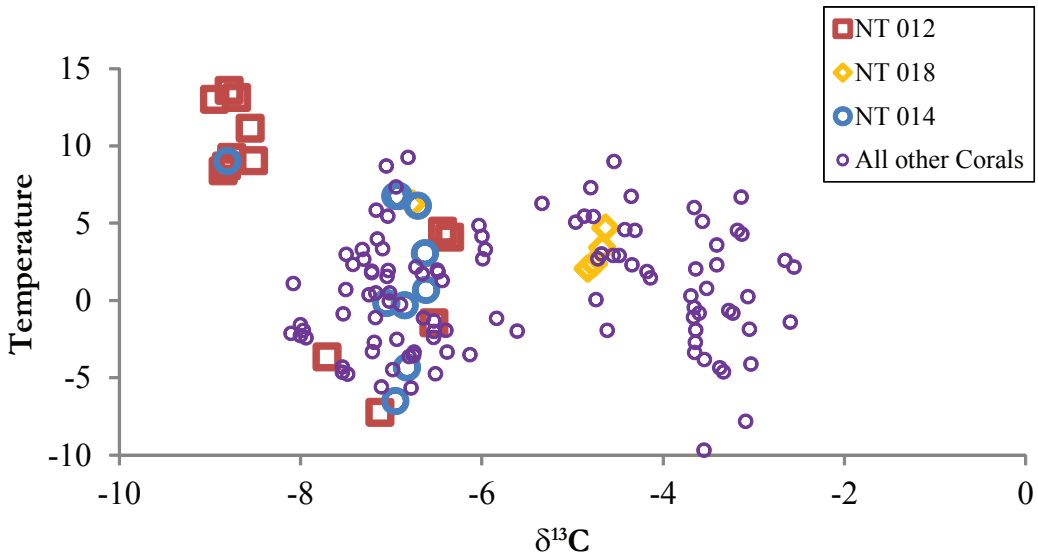

Figure 4.4: Three deep-sea corals exhibit vital effects. This vital effect is exhibited as an increase in temperature that corresponds to very depleted $\delta^{13}C$ values.

very depleted $\delta^{13}C$ values correspond to elevated temperatures. These very depleted $\delta^{13}C$ values are typically found in the centers of calcification (COCs). Future work will involve measuring the clumped isotope value of COCs.

After excluding points, that were effected by vital effects, we reconstructed temperature profiles. The temperature profile for the YD and H1 is much cooler than the modern ocean. The Younger Dryas temperature profile is isothermal -1.5 to 0.5°C at all measured depths. The coral from the Bolling Allerod is as warm as modern at 3.1°C at 1316 m while the H1 profile is isothermal from 1000–2000 m, with a range of (-1.2–-0.2°C). At deeper depths, there is a slight warming to 3.5°C. From 16.1–17.7ka BP at 1427–2459 m the temperature ranges form -1.1–1.3°C implying that the warming at deeper depths started after 16.1 ka BP.

The isothermal temperature profile of the YD and slight warming at deeper depths in the H1 profile implies that the deglacial ocean was stratified by salt as opposed to by temperature as it is in the modern ocean. The $\Delta^{14}C$ profile for the YD ranges from 64-119‰ while the H1 profile ranges from 45–170‰. During late H1, at 1381–2265 m the profile is near constant while below at 2593 m, the $\Delta^{14}C$ is depleted relative to the upper water column.

4.4 DISCUSSION

The corals dated to later in H1 can either be interpreted in two ways; as a time series with four corals at 15.6 ka and one at 15.1 ka, or a single profile of five corals with overlapping 2σ error bars at 15.35 ka. In the first scenario, the 15.6ka profile is isothermal from 1176–2027 m at -0.7°C and there is a slight warming from 2027–2372m of -1.2±1.2°C to 1.6±1°C. At 15.1±0.2 ka, the deep ocean warms to 3.5°C. In the second instance, the profile at 15.35 ka is isothermal between 1381–2027m and exhibits warming with depth.

The increase in temperature at depths in the H1 profile is an unusual feature. This warming at depth implies that salt is controlling the density stratification with depth as

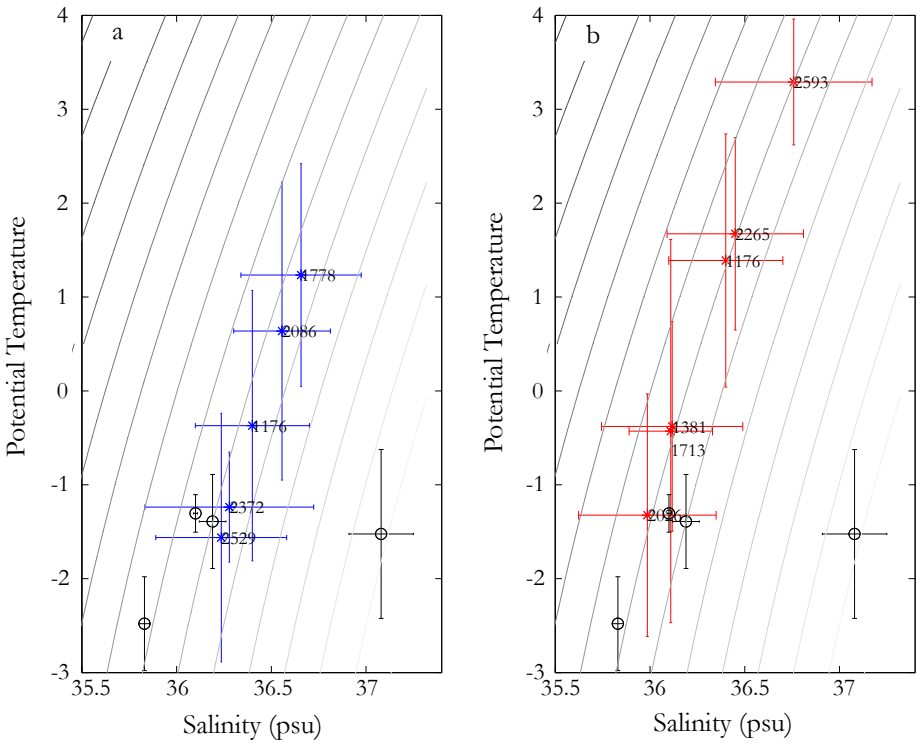

Figure 4.5: The salinity values needed if a constant potential density profile is assumed. (A) LGM theta and salinity estimates in black with the YD in blue. (B) LGM theta and salinity estimates in black with H1 in red. The depths of corals are indicated next to each point.

opposed to temperature, as in the modern ocean. The increase in temperature is a feature of late H1, and begins after 17.1 ka. The warming is also not present during the time of the Younger Dryas seven thousand years later.

Salt stratification in the ocean has been shown to exist during the last glacial time period (18). If we assume constant potential density through the water column we can calculate the minimum salt difference needed to support the warming with depth. We find that the salinity ranges from 36.15 psu to 36.94 psu at late H1 (Figure 4.5), which is within the bounds of the endmembers of the glacial ocean (North Atlantic: 35.83 psu and Southern Ocean: 37.08 psu) (19). This scenario of a salty, warm, and depleted in $\Delta^{14}C$ water below cooler, fresher and more ventilated intermediate waters is consistent with the "thermobaric effect" hypothesis (20).

In the presence of a salt stratified deep ocean, warming at depth can maintain the static stability of the water column. Geothermal heating at the ocean's bottom ranges from 50–100 mW/m^2 (21). For a geothermal heat flux of 50 mW/m^2, 10,000 years are necessary to heat a two km thick parcel of seawater with a salinity difference of 0.4 psu, by 2°C. This long time scale implies that the warming seen at depth at 15.1±0.2 ka must also have been present at 15.6 ka. However if the relevant water mass was thinner, then less time would be required to heat the deeper isopycnals.

The thermobaric effect is a potential energy storage mechanism, a capacitor, which can result in an abrupt overturning of the water column (or deep ocean mixing). As this scenario occurs, the water column changes from having cold fresh water above cold salty water (as in the LGM state) to cold fresh water above warm salty water as geothermal heating occurs. Afterwards cooler waters from the surface are pushed deeper so the water column changes to cold fresh water above warm salty water, above a growing cold water mass. Finally as the density difference between the cold water being pushed downwards and the bottom water mass becomes close to zero, the water column becomes unstable and convects. This convection results in warm salty water above cold fresh water (as in the

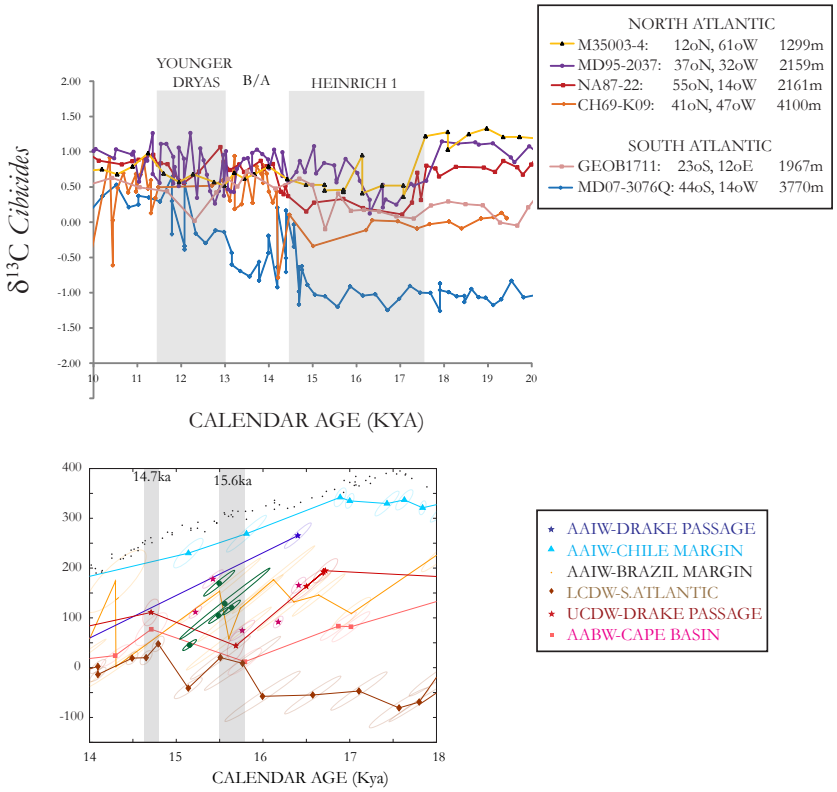

Figure 4.6: (A) The cores that mixed at the end of Heinrich 1 in the North and South Atlantic are all 1200-4100 m. Deeper and shallower cores did not mix. (B) The cores that mixed during at 15.6 ka event in the Southern Ocean are all from deeper isopycnals, while the shallow isopycnals (AAIW by Chile and the corals) did not mix. One core at the Brazilian margin is at a shallower isopycnal and did mix. One possible explanation is the $\Delta^{14}C$ values from the core are affected by methane hydrate seeps.

modern state).

The source of heating at depth could be geothermal heating, but another possibility is a temperature increase at the location of outcropping of the deeper isopycnals, possibly through frontal movement. The "charging of the capacitor" is also seen in the Iberian Margin (22). Similarly to our record, from 17 ka to 15 ka, the deep ocean temperature (as record in Mg/Ca of *G. affinis*) increases from -0.5°C to 2°C (at 3146 m). After which the temperature begins to decline.

The "discharging of the capacitor" is also seen in several other marine and atmospheric records. Benthic $\delta^{13}C$ from the North and South Atlantic show vertical convection of the water column from 1200–4000 m at the beginning of the B/A as the benthic $\delta^{13}C$ at these locations all share a common value of 0.5‰ (Figure 4.6a). This event is also seen in the $\Delta^{14}C$ record as a decrease in ventilation age in the deep South Atlantic and a deepening of the Atlantic overturning circulation (23, 24). The beginning of the Bolling-Allerod is at 14.7 ka is also associated with abrupt changes in the atmosphere (Figure 4.1) (25). There was a sharp rise in pCO_2 of 12 ppmv that lasted 300 years (26) which was also synchronous with the start of the Antarctic Cold Reversal (27) as well as abrupt rises in $\delta^{18}O$ of ice (28). There is also a change in the slope of the $\delta^{13}C_{atm}$ record, as well as a rapid rise in sea level (MWP 1a) (29) and a retreat of sea ice in the Northern Hemisphere (30). These features are all consistent with ocean mixing causing the restart of the AMOC and ventilating an isolated reservoir of carbon causing warming.

There is evidence for two other mixing events occurring over the course of the last glacial termination, at 17.5 and 15.6 ka. At 17.5 ka there are two purported areas of the ocean where increased mixing released CO_2 into the atmosphere, the Southern Ocean and North Pacific. The Southern Ocean shows an increase in upwelling as seen in opal flux (9) and a decline in ^{14}C ages of benthic foraminifera in intermediate depth waters(37). It is thought that this increase in upwelling could have ventilated a deep ocean reservoir near Antarctica which would have supplied ^{14}C-depleted carbon to the atmosphere, causing

the drop in $\Delta^{14}C_{atm}$ that is seen at the start of 17.5 ka. The intermediate depth waters saw this depleted-^{14}C as it was being ventilated to the atmosphere. 17.5 ka is also the time of increased vertical deep convection in the North Pacific which has been shown through a model to have been capable of releasing depleted $\delta^{13}C$ and $\Delta^{14}C$ carbon into the atmosphere (38).

At 15.6 ka, the Southern Ocean's $\Delta^{14}C$ of Upper Circumpolar Deep Water (UCDW), Lower Circumpolar Deep Water (LCDW) and AABW become more similar as the $\Delta^{14}C$ of UCDW and AABW decrease and that of LCDW increases (Figure 4.6b). There is also an intensification of upwelling in the Southern Ocean (9). These changes are indicative of increased deep mixing in the Southern Ocean and a breakdown of the deep vertical stratification that characterizes the LGM. This increased mixing supports the release of carbon from the Southern Ocean and is reflected in changes in slope in the pCO_2, $\Delta^{14}C_{atm}$ and the $\delta^{13}C_{atm}$ records. At essentially the same time (15.4 ka) in the deep North Atlantic there is evidence of increased lateral mixing as seen in older $\Delta^{14}C$ and Cd in a narrow depth range of 1500–2000 m, implying an increase in southern sourced waters (43). This lateral mixing is consistent with the near constant $\Delta^{14}C$ and temperature values seen in the H1 profile between 1300–2000 m. However the effect on the atmospheric record is different than the onset of the termination. There is no change in slope of the pCO_2 record at 15.6, although there is a pause in the decline of $\Delta^{14}C_{atm}$ and an increase in $\delta^{13}C_{atm}$.

The marine benthic $\delta^{13}C$ records do not show a similar mixing pattern as seen in the $\Delta^{14}C$ records. Only the intermediate depth water benthic $\delta^{13}C$ records converge to a single value (implying mixing). The benthic $\delta^{13}C$ records of the shallow depths compared to deeper depths in the North and South Atlantic remain stratified and do not converge until the start of the Bolling/Allerod. Further evidence of this mismatch in timing is seen in a southern Atlantic core, MD07-3076Q at 44° S, 14° W and 3770 m which shows the mixing in $\Delta^{14}C$ (41) occurring at a deeper depth in the core than the increase in $\delta^{13}C$ to a heavier value of 0.5‰ (22).

One explanation for this seeming discrepancy is as follows. At 15.6 ka, the Southern Ocean begins to mix vertically which is exhibited in $\Delta^{14}C$ records from the Southern Ocean. This mixing is seen in $\Delta^{14}C$ because the different water masses have dramatically different $\Delta^{14}C$ values, so any change in mixing is seen rapidly in $\Delta^{14}C$. $\delta^{13}C$ in ocean is a nonconservative tracer, so this mixing might have coincided with changes in air-sea gas exchange or remineralization rates which masked the mixing event in $\delta^{13}C$. This mixing event must also have been associated with an increase in formation of southern sourced intermediate waters, or a decrease in formation of Glacial North Atlantic Intermediate waters. This change allows southern sourced waters to arrive in the North Atlantic and cause lateral mixing there, as seen in high Cd, and depleted $\Delta^{14}C$ (42, 43). At the start of the Bolling-Allerod, at 14.7 ka, there is the restart of the AMOC and increased warming. This restart of AMOC brings NADW (high in $\delta^{13}C$) to the deep North and South Atlantic explaining the mixing seen in $\delta^{13}C$ and $\Delta^{14}C$. The warm coral at 15.1 ka could show evidence of geothermal heating warming the bottom before destabilizing the water column allowing for AMOC to resume.

An alternate explanation for the warming at depth in the late H1 profile, which does not involve the "Thermobaric Capacitor Hypothesis", is perhaps that the NW Atlantic is seeing the warming of a deep water mass. The deeper points in the profile could reflect a depleted warm Southern sourced deep water in the North Atlantic while the depths between 1300–2000 m could reflect the presence of a ventilated cool Northern sourced water. There is evidence for deglacial warming of the surface ocean in high Southern latitudes (44, 45). This warming could be transferred to depth by deep water formation and thus be reflected in our profile.

The Younger Dryas profile at 12.1–11.7 ka occurs at a time when the state of the ocean during the YD/Holocene transition was very different to the deglacial ocean during H1. Deep water formation had slowed allowing fresh water to pool on the surface as the result of extensive winter sea ice cover (30). This shut down of AMOC led to a cooling

of the Northern hemisphere which caused a southward shift to the ITCZ (11) as well as a weakened Asian Monsoon (6). The atmospheric records also show strong changes., for instance the CO_2 record begins to rise at the YD after stalling at the Bolling Allerod. This rise is associated with a burst of upwelling in the Southern Ocean(9). At the start of the YD, the $\Delta^{14}C_{atm}$ initially rises, which is thought to be associated with the reduction of $\Delta^{14}C$ oceanic exchange due to the slowdown of AMOC that persisted for ~ 200 years. At 12.6 ka, the $\Delta^{14}C_{atm}$, declines which is consistent with a reinvigoration of NADW or the activation of another radiocarbon sink which brings radiocarbon back into equilibrium with the atmosphere.

At the start of the YD, the $\delta^{13}C$ of *Cibicides* in the deep North and South Atlantic (41), and Cd/Ca ratios indicate an increased Southern influence to deep North Atlantic, while the intermediate depth records are more equivocal and indicate either an increased Southern (42) or Northern influence (46). At 12.2 ka (within error of the beginning of the decline of $\Delta^{14}C_{atm}$ and the beginning of Southern Ocean upwelling) the $\delta^{13}C$ of Cibicides in the North Atlantic from 1200–4100 m and the deep South Atlantic approach 0.57‰, implying mixing within those isopycnals. This is also a time of increased upwelling in the Southern Ocean(9). Later at 11.6 ka in the intermediate depth waters in the NW Atlantic there are very large and mobile gradients in $\Delta^{14}C$ (47). Our temperature and $\Delta^{14}C$ record at 12.1–11.7 ka are nearly constant with depth and occur after the mixing event in the North and South Atlantic and likely before the appearance of transients in the intermediate depth waters. However future work of top, middle and bottom radiocarbon dates will elucidate the exact timing of our profile relative to the appearance of transients.

4.5 CONCLUSIONS

In conclusion, we show coupled radiocarbon, U-series and clumped isotope measurements that show evidence for salinity stratification at late H1 and the YD. We also find increased warming at depth during late H1 which could be consistent with the charging of a "Thermobaric Capacitor" at the beginning of the B/A. The discharge of

the capacitor causes the ocean to convect and release CO_2 into the atmosphere, which is seen in marine benthic $\delta^{13}C$, $\Delta^{14}C$ and atmospheric records. We review other oceanic mixing events that occurred during the termination and find they each had a different signature in marine and atmospheric records. The 17.8 ka event released CO_2 into the atmosphere and initiated warming while shutting down AMOC. The 15.6 ka event did also change the slope of the pCO_2 record and $\delta^{13}C$ record, and the benthic $\Delta^{14}C$ record but not $\delta^{13}C$ record. We also place the YD in the context of other marine records and conclude that our record takes place after an oceanic mixing event that released CO_2 into the atmosphere. This is supported by the nearly constant temperature and $\Delta^{14}C$ seen in the profile.

References

1. EPICA, Eight glacial cycles from an Antarctic ice core. Nature 429, 623 (2004).

2. W. Dansgaard et al., North Atlantic climate oscillations revealed by deep Greenland Cores, Climate Processes and Climate Sensitivity. Am. Geophy. Union Mon. 29, 288 (1984).

3. C. D. Charles, J. Lynch-Stieglitz, U. S. Ninnemann, R. G. Fairbanks, Climate connections between the hemisphere revealed by deep sea sediment core/ice core correlations. Earth Planet Sc Lett 142, 19 (1996).

4. R. J. Behl, J. P. Kennett, Brief interstadial events in the Santa Barbara basin, NE Pacific, during the past 60 kyr. Nature 379, 243 (1996).

5. X. Wang et al., Wet periods in northeastern Brazil over the past 210 kyr linked to distant climate anomalies. Nature 432, 740 (2004).

6. Y. J. Wang et al., A high-resolution absolute-dated late Pleistocene monsson record from Hulu Cave, China. Science 294, 2345 (2001).

7. T. Blunier, E. Brook, Timing of millennial-scale climate change in Antarctica and Greenland during the last glacial period. Science 291, 109 (2001).

8. B. Lemieux-Dudon et al., Consistent dating for Antarctic and Greenland ice cores. Quaternary Sci Rev 29, 8 (2010).

9. R. F. Anderson et al., Wind-Driven Upwelling in the Southern Ocean and the Deglacial Rise in Atmospheric CO2. Science 323, 1443 (March 13, 2009, 2009).

10. J. C. H. Chiang, C. M. Bitz, Influence of high latitude ice cover on the marine intertropical convergence zone. Clim Dynam 25, 477 (2005).

11. J. C. H. Chiang, The Tropics in Paleoclimate. Annual Review of Earth and Planetary Sciences 37, 263 (2009/05/01, 2009).

12. J. F. Adkins, A. P. Ingersoll, C. Pasquero, Rapid climate change and conditional instability of the glacial deep ocean fron the thermobaric effect and geothermal heating. Quaternary Sci Rev 24, 581 (2005).

13. J. F. Adkins, K. McIntyre, D. P. Schrag, The salinity, temperature, and delta O-18 of

the glacial deep ocean. Science 298, 1769 (Nov 29, 2002).

14. J. F. Adkins et al., Radiocarbon dating of deep-sea corals. Radiocarbon 44, 567 (2002).

15. L. F. Robinson et al., Deep-sea scleractinian coral age and depth distributions in the NW Atlantic for the last 225 thousand years. B Mar Sci 81, 371 (2007).

16. N. G. Thiagarajan, D. S.; Roberts, M.; McNichol, A. P.; Thresher, R.; Adkins, J. F., paper presented at the American Geophysical Union, San Francisco, 2009.

17. A. Burke et al., Reconnaissance dating: A new radiocarbon method applied to assessing the temporal distribution of Southern Ocean deep-sea corals. Deep Sea Research Part I: Oceanographic Research Papers 57, 1510 (2010).

18. J. F. Adkins, K. McIntyre, D. P. Schrag, The salinity, temperature, and d18O of the glacial deep ocean. Science 298, 1769 (2002).

19. J. F. Adkins, K. McIntyre, D. P. Schrag, The temperature, salinity and delta O-18 of the LGM deep ocean. Geochim Cosmochim Ac 66, A7 (Aug, 2002).

20. J. F. Adkins, A. P. Ingersoll, C. Pasquero, Rapid climate change and conditional instability of the glacial deep ocean from the thermobaric effect and geothermal heating. Quaternary Sci Rev 24, 581 (Mar, 2005).

21. C. A. Stein, S. Stein, A model for the global variation in oceanic depth and heat-flow with lithospheric age. Nature 359, 123 (1992).

22. L. C. Skinner, N. J. Shackleton, Deconstructing Terminations I and II: revisiting the glacioeustatic paradigm based on deep-water temperature estimates. Quaternary Sci Rev 25, 3312 (2006).

23. S. Barker, G. Knorr, M. J. Vautravers, P. Diz, L. C. Skinner, Extreme deepening of the Atlantic overturning circulation during deglaciation. Nature Geosci 3, 567 (2010).

24. J. McManus, R. Francois, J. Gherardi, L. Keigwin, S. Brown-Leger, Collapse and rapid resumption of Atlantic meridional circulation linked to deglacial climate changes. Nature 428, 834 (2004).

25. J. P. Steffensen et al., High-Resolution Greenland Ice Core Data Show Abrupt Climate Change Happens in Few Years. Science 321, 680 (August 1, 2008, 2008).

26. A. Lourantou, J. Chappellaz, J. M. Barnola, V. Masson-Delmotte, D. Raynaud, Changes in atmospheric CO2 and its carbon isotopic ratio during the penultimate deglaciation. Quaternary Sci Rev 29, 1983 (2010).

27. B. Stenni et al., An Oceanic Cold Reversal During the Last Deglaciation. Science 293, 2074 (September 14, 2001, 2001).

28. NGRIP, High-resolution record of Northern Hemisphere climate extending into the last interglacial period. Nature, 147 (2004).

29. A. J. Weaver, O. A. Saenko, P. U. Clark, J. X. Mitrovica, Meltwater Pulse 1A from Antarctica as a Trigger of the Bølling-Allerød Warm Interval. Science 299, 1709 (March 14, 2003, 2003).

30. G. H. Denton, R. B. Alley, G. C. Comer, W. S. Broecker, The role of seasonality in abrupt climate change. Quaternary Sci Rev 24, 1159 (2005).

31. EPICA, One-to-one coupling of glacial cliamte variability in Greenland and Antarctica. Nature 444, 195 (2006).

32. J. Southon, A. L. Noronha, H. Cheng, R. L. Edwards, Y. Wang, A high-resolution record of atmospheric 14C based on Hulu Cave speleothem H82. Quaternary Sci Rev 33, 32 (2012).

33. J. Schmitt et al., Carbon Isotope Constraints on the Deglacial CO2 Rise from Ice Cores. Science, (March 29, 2012, 2012).

34. S. R. Hemming, Heinrich events: Massive late Pleistocene detritus layers of the North Atlantic and their global climate imprint. Reviews of Geophysics 42, RG1005 (2004).

35. H. Heinrich, Origin and consequences of cyclic ice rafting in the northeast Atlantic Ocean during the past 130,000 years. Quaternary Research 29, 142 (1988).

36. S. Toucanne et al., Timing of massive 'Fleuve Manche' discharges over the last 350 kyr: insights into the European ice-sheet oscillations and the European drainage

network from MIS 10 to 2. Quaternary Sci Rev 28, 1238 (2009).

37. T. M. Marchitto, S. Lehman, J. Ortiz, J. Fluckiger, A. vanGeen, Marine radiocarbon evidence for the Mechanism of deglacial atmospheric CO2 rise. Science 316, 1456 (2007).

38. J. Rae, Foster, G, Gutjahr, M, Sarnthein, M, Skinner, L, Schmidt, D, Elliot, T paper presented at the Goldschmidt, Prague, 2011.

39. C. Laj et al., Geomgnetic field intensity, North Atlantic deep water circulation and atmospheric D14C during the last 50 kyr. Earth Planet Sc Lett 200, 177 (2002).

40. R. Muscheler et al., Changes in the carbon cycle during the last deglaciation as indicated by the comparison of 10Be and 14C records. Earth Planet Sc Lett 219, 325 (2004).

41. C. Waelbroeck et al., The timing of deglacial circulation changes in the Atlantic. Paleoceanography 26, PA3213 (2011).

42. R. E. M. Rickaby, H. Elderfield, Evidence from the high-latitude North Atlantic for variations in Antarctic Intermediate water flow during the last deglaciation. Geochem Geophy Geosy 6, doi:1029/2004GC000858 (2005).

43. J. F. Adkins, H. Cheng, E. A. Boyle, E. R. M. Druffel, L. Edwards, Deep-sea coral evidence for rapid change in ventilation of the deep North Atlantic 15,400 years ago. Science 280, 725 (1998).

44. E. Calvo, C. Pelejero, P. De Deckker, G. A. Logan, Antarctic deglacial pattern in a 30 kyr record of sea surface temperature offshore South Australia. Geophys. Res. Lett. 34, L13707 (2007).

45. F. Lamy et al., Antarctic Timing of Surface Water Changes off Chile and Patagonian Ice Sheet Response. Science 304, 1959 (June 25, 2004, 2004).

46. T. M. Marchitto, W. B. Curry, D. W. Oppo, Millennial-scale changes in North Atlantic circulation since the last glaciation. Nature 393, 557 (1998).

47. S. F. Eltgroth, J. F. Adkins, L. F. Robinson, J. Southon, M. Kashgarian, A deep-sea coral record of North Atlantic radiocarbon through the Younger Dryas: Evidence for intermediate water/deepwater reorganization. Paleoceanography 21, (Nov 17, 2006).

Chapter 5:
Radiocarbon chronology and the response of Late Quaternary Megafauna to Rapid Climate Change

5.1 INTRODUCTION

The Quaternary megafaunal extinction is the most recent of Earth's major extinction events and wiped out nearly all large and slow-breeding mammals. On a global scale, the extinctions followed first appearances of humans or expanding human populations in many regions as well as the end of the last glacial period (1). However due to uncertainties in dating, estimates of the duration of co-existence between humans and megafauna remain imprecise. The megafaunal extinction is also difficult to explain by relying solely on environmental change as megafauna had survived through previous glacial-interglacial cycles, as well as several rapid climate change events. Debate about the possible cause of the extinction has continued for over 150 years, stimulated by new fossil finds, dating techniques, and modes of analysis.

There are several hypotheses for how climate change could have affected the megafauna extinction. They all focus on the ecological effects of climate change that would lead to extinction, for instance, the "habitat loss hypothesis" (HLH), the "mosaic-nutrient hypothesis" (MNH), the "co-evolutionary disequilibrium hypothesis" (CED) and "self-organized instability Hypothesis" (SOI). HLH posits that as climate changed, areas with adequate conditions to maintain megafauna reduced in area, making it difficult to support megafauna populations (2). MNH suggests that climate change reduced the growing season, local plant diversity, and increased plant antiherbivore defenses all of which reduced the ability of the land to support herbivores (3). The CED hypothesizes that the rapid glacial-interglacial transition stressed the flora, causing a reorganization of the ecology. This reorganization essentially starved herbivores, as preferred species became less abundant (4). The SOI hypothesis holds that species in an ecosystem will reach a certain level and will subsequently be maintained through immigration, speciation, or extinction. A slight perturbation (in this case climate change) is amplified into

a catastrophe by dynamics intrinsic to complex ecosystems with multiple subunits (5). To disentangle the processes underlying megafauna response to climate change, we investigated the radiocarbon chronologies of megafauna from the La Brea Tar Pits and other deposits around the world.

The La Brea Tar Pits are located in Downtown Los Angeles and span 23 acres. They are an exceptional fossil deposit in the Miocene-aged Monterrey Shale Formation and have preserved over three million fossil skeletons including 3400 large mammals. These deposits provide the type assemblage of the Rancho Land Mammal Age and provide a unique view of terrestrial ecology in the LA Basin during the Pleistocene. The deposits are a series of open asphalt seeps that have acted as animal traps for at least the past 50,000 years (6). Previous studies have been limited by weak chronological control, as stratigraphic position is known to be an unreliable indicator of relative age within the asphalt deposits (7). Dating the megafauna remains in this fossil deposit could help put further constraints on the relationship of terrestrial megafauna in North America with climate change. The preferred method for dating megafauna remains has been radiocarbon dating. However, radiocarbon dating remains from the La Brea Tar Pits has been plagued by difficulties in removing the impregnating asphalt.

Radiocarbon dates on bones are often the most direct method of obtaining chronological information on geological and anthropological events in terrestrial settings. They are also helpful for bypassing problems with stratigraphic correlation or the necessity of finding and dating coeval wood or charcoal. However, radiocarbon dates on bones are particularly problematic, as some dates have yielded ages contrary to stratigraphic or cultural expectations (8, 9). This discrepancy has been attributed to environmental contamination of the bone sample. Preservation of bone is influenced by the depositional environment, including pH, microbial activity, temperature, and water (10). It has been thought that if ^{14}C from the original bone itself could be isolated and analyzed, the correct age of the bone could be determined.

Another difficulty with radiocarbon dating of bones is how to isolate fractions of bones that are not susceptible to environmental contamination. Bone is composed of two carbon-

bearing fractions, hydroxyapatite and organic matter. Hydroxyapatite has an open structure into which precipitates from ground water can easily be deposited, so it is not commonly used for radiocarbon ages. In modern bone, organic matter or proteins make up 30% of the bulk of bone material of which 90–95% is composed of collagen.

There has been much recent development to reduce contamination in radiocarbon dating, including filtering organic components through molecular filters and isolating specific molecular components (11). The most common of these is to isolate amino acids from bones using column chemistry. However it is possible that single amino acids in bone could have several sources besides the animal itself, such as contamination from bacterial degradation products or natural ground water (12).

It was first suggested by Ho et al. in 1969 (13) that isolating hydroxyproline from bones in the La Brea Tar Pits could improve radiocarbon dating of bones because hydroxyproline is a nonessential amino acid that is found almost exclusively in mammalian collagen and elastin. However extracting and suitably purifying hydroxyproline from bone has proved to be a challenging task. The isolation of hydroxyproline has almost exclusively relied on ion-exchange chromatography, XAD resins and derivatization routines, using organic solvents (14). These resins, organic solvents and derivatzing compounds could be a potential source of carbon contamination. Here, I have developed a high-performance liquid chromatography method for separating hydroxyproline from other amino acids in collagen using only Milli Q H2O.

5.2 METHOD DEVELOPMENT

All analyses for method development were made using a *Smilodon fatalis* femur dated previously to 29,600 years by separating collagen-derived amino acids using a liquid chromatography method (6). Fractions of bones were analyzed using %C, $\delta^{13}C$, and $\Delta^{14}C$ to determine the proper procedure for extracting organic matter from bones. Once the organic matter was extracted, a high performance liquid chromatography (HPLC) method was developed for separating hydroxyproline from organic matter.

5.2.i Extracting Organic Matter from Bones

Several grams of bone was cut from the femur using a Dremel tool and powdered finely to pass through a ~ 200 um sieve. This powder was divided into three portions. One portion was acidified in 1N HCl for 8 hours and washed with water. An aliquot was removed for %C and $\delta^{13}C$ analysis, and the process was repeated eight times to determine the amount of HCl needed to remove carbonates from powdered bone. A second portion was processed through a microwave assisted solvent removal system (MARS). The MARS allows organic matter (asphalt, humic acids) to be leached from bones at a much faster rate than typical reaction times on bench tops because the MARS elevates the temperature of the sample. The bone sample was dissolved in 20 ml of 9:1 Dichloromethane/acetone and heated to 100°C in the MARS. Afterwards an aliquot was removed for %C and $\delta^{13}C$ analysis and the process was repeated eight times. The third portion was decalcified, processed through the MARS, again decalcified and again processed through the MARS. Aliquots were removed at each step for %C and $\delta^{13}C$ analysis. The aliquots were analyzed for %C and $\delta^{13}C$ and the results are shown on Figure 5.1.

For successive steps of decalcification, the %C in the sample increases from 12% (predominantly carbonate) to ~ 40% (predominantly organic matter) over the course of four steps of carbonate removal using implying that only four steps of decalcification are necessary. After four steps, the %C begins to decrease to 25%. The $d^{13}C$ of these samples also drops from -18‰ to -19.5‰ until the fourth decalcification step. Afterwards, the $d^{13}C$ begins declining. There are two possibilities to explain the decrease in %C and $\delta^{13}C$ after Step 4. One is that the reaction with HCl is removing acid volatile organic matter (carbohydrates and proteins), leaving only lipids in the sample. Lipids are ~ 4‰ depleted relative to carbohydrates, therefore this scenario would also explain the decrease in $\delta^{13}C$. A second possibility is that the continued reaction with HCl is dissolving the organic matter and leaving behind the asphalt. The asphalt has been characterized to have a $\delta^{13}C$ of -25‰ (15), so could explain the decline in $\delta^{13}C$ after four steps of decalcification. For successive steps of MARS reaction, the $\delta^{13}C$ of the bone immediately rises to -16‰ from -18‰, and further MARS reaction steps do not alter this value, implying that only

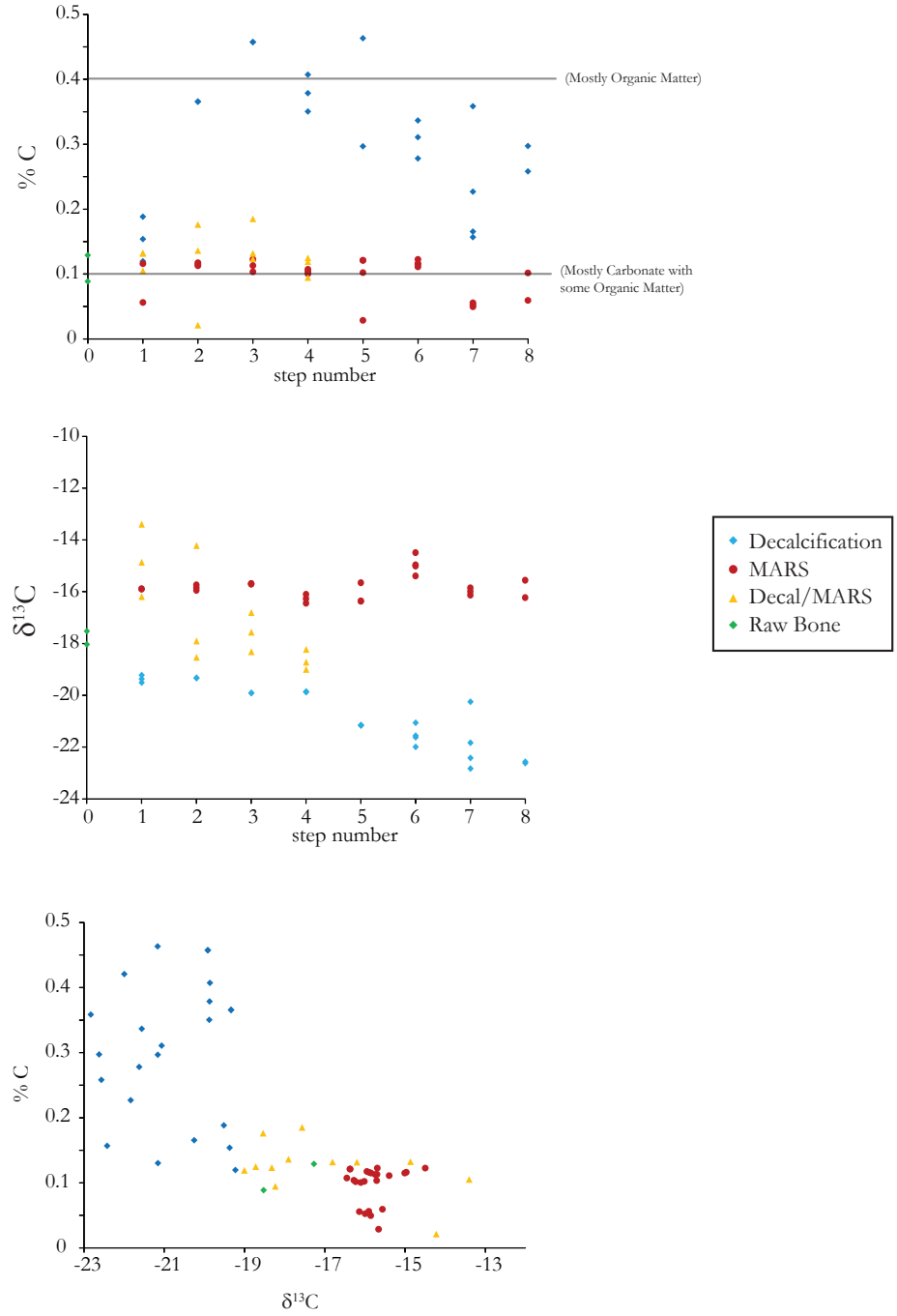

Figure 5.1: %C and $\delta^{13}C$ results of three different cleaning procedures. Decal: 8 sequential decalcification steps. MARS: 8 sequential MARS steps. Decal/MARS: a sample of bone that was Step 1: decalcified, Step 2: processed through MARS, Step 3: decalcified, and Step 4: processed through MARS

one MARS reaction step is needed. For the alternate decalcification and MARS steps, never rises about 0.2%, and the $\delta^{13}C$ begins to decline to -20‰, though does not plateau.

Further method development was done using ^{14}C. A bone sample was reacted with 1N HCl, and then processed through the MARS twice. Aliquots of the bone were removed at each step, and the solvents extracted from the bone were also saved. Both the solid and liquid fractions were sent to KECK-UCIAMS for ^{14}C analysis and the results are shown on Figure 5.2. The first step of 1N HCl acidification resulted in the bone increasing in age by 1300 years, implying that young carbonate was removed. The first MARS step lowered the age by 800 years, implying that older asphalt was removed. The second MARS step did not change the age, further confirming that only one MARS step is needed for asphalt removal. The asphalt removed at both steps had a Fm of 0.006, close to the detection limit of the AMS, consistent with the source of the asphalt being derived from the Miocene aged Monterrey Shale Formation.

From these results we conclude that the proper cleaning procedure for these bones is four sequential steps of 1N HCl for 8 hours each and one step of asphalt removal through the MARS.

5.2.ii Extracting Hydroxyproline from the Organic Matter

The remaining organic matter is composed of proteins, carbohydrates, and lipids. We developed a HPLC protocol for separating hydroxyproline from this organic matter. The organic matter was reacted with 30 ml of 6 M HCl for 24 hours at 105°C under a nitrogen atmosphere following standard laboratory procedures (16). After the reaction was complete, the aqueous acid was lyophilized and then redissolved in MILLI Q H2O for HPLC separation and analysis. Chromatography was performed on a Agilent 1100 series HPLC system consisting of two isocratic pumps all controlled by HPCORE Chemstation PC software. The autosampler was fitted with a 900 uL sample loop and a 1 mL syringe and a Supelco Primesep A column. Primsep A is a mixed mode column with reversed phase and hydrophilic interaction chromatography making it especially suited for separating amino acids and other weak acids and bases. The column was washed with 2L of 75:25:0.1 ‘ACN:H2O:acetic acid’. Up to 900 uL of sample (hydrolyzed collagen or a reference sample) was injected with a flow rate of 4.7 ml/min into the

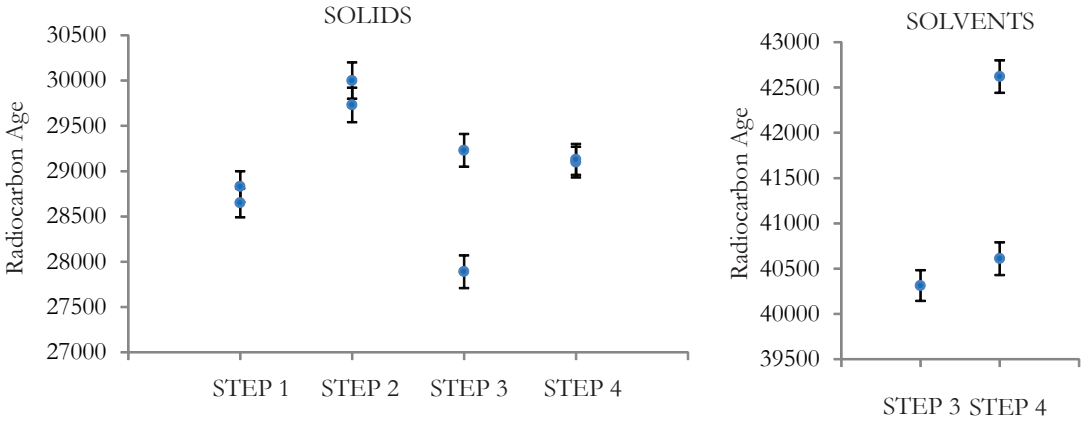

Figure 5.2: $\Delta^{14}C$ results of a cleaning procedure on one bone sample taken through four cleaning procedures. Step 1: raw bone, Step 2: bone after decalcification, Step 3: bone (or extracted solvents) after the first MARS procedure, and Step 4: bone (or extracted solvents) after the second MARS procedure

guard column with MILLI Q H_2O tirated to pH 4 with concentrated SeaStar HCl. At 2 min, the guard column was then backflushed to remove most of the more nonpolar amino acids, and the polar amino acids (which included hydroxyproline) were allowed to separate for 22.5 min in pH 4 MILLI Q H2O. This procedure allowed for the separation of aspartic acid, hydroxyproline, glutamic acid, glycine, and proline in MILLI Q H_2O. Amino acids were detected using an APCI quadrupole mass spectrometer. After 22.5 min the mobile phase was changed to 0.5% TFA to flush out any remaining compounds from the column. The column was then re-equilibrated for 20 min with pH 4 MILLI Q H_2O. Complete time from sample injection, separation and column cleaning and re-equilibration was 1 hr. Sample HPLC traces are shown on Figure 5.3. Fractions of hydroxyproline were collected and lyophyllized to remove water. Yields were quantified by two methods. The amount of sample injected was compared to peak area calibration curves made for the day (Figure 5.4) or fractions of amino acids were collected and lyophyllized to remove water and weighed. Yields ranged from 95−100%. After lyophillization, the hydroxyproline was sealed in quartz vialed with baked CuO and Ag and heated to 850°C for 5 hours to generate CO_2 for ease of analysis by Gas Source-AMS. A modern hydroxyproline was analyzed for $\Delta^{14}C$ before and after processing through the HPLC and no fractionation was observed within error (Figure 5.5). The error bars are larger than traditional hydrolysis ^{14}C measurements. However, this is a feature of the gas source-AMS. Since these measurements were made, errors made using this technique have declined.

Future work entails measuring the hydroxyproline for $\Delta^{14}C$ to determine whether hydroxyproline extracted from fossilized bone has a different $\Delta^{14}C$ signature than radiocarbon dates made on collagen or carbonates in bone, before analyzing bones from the La Brea Tar Pits.

5.3 DISCUSSION

Although bones from the La Brea Tar Pits have not been radiocarbon dated using extracted hydroxyproline, 152 ^{14}C dates have been made using a variety of different methods (Figure 5.6). The dates were made with two different methods (scintillation counter and AMS) and made on a variety of different carbon extracts, (apatite, carbonate, collagen and amino acids).

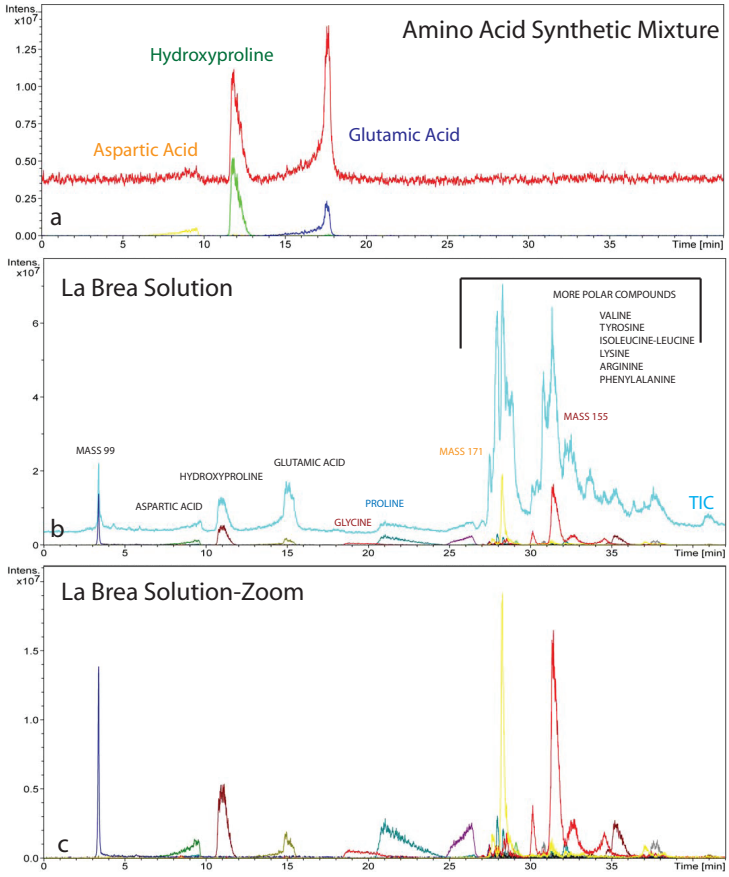

Figure 5.3: HPLC traces of a) an amino acid synthetic mixture of aspartic acid, hydroxyproline, and glutamic acid, and b) a La Brea Solution. Both solutions baseline separate hydroxyproline from all other amino acids.

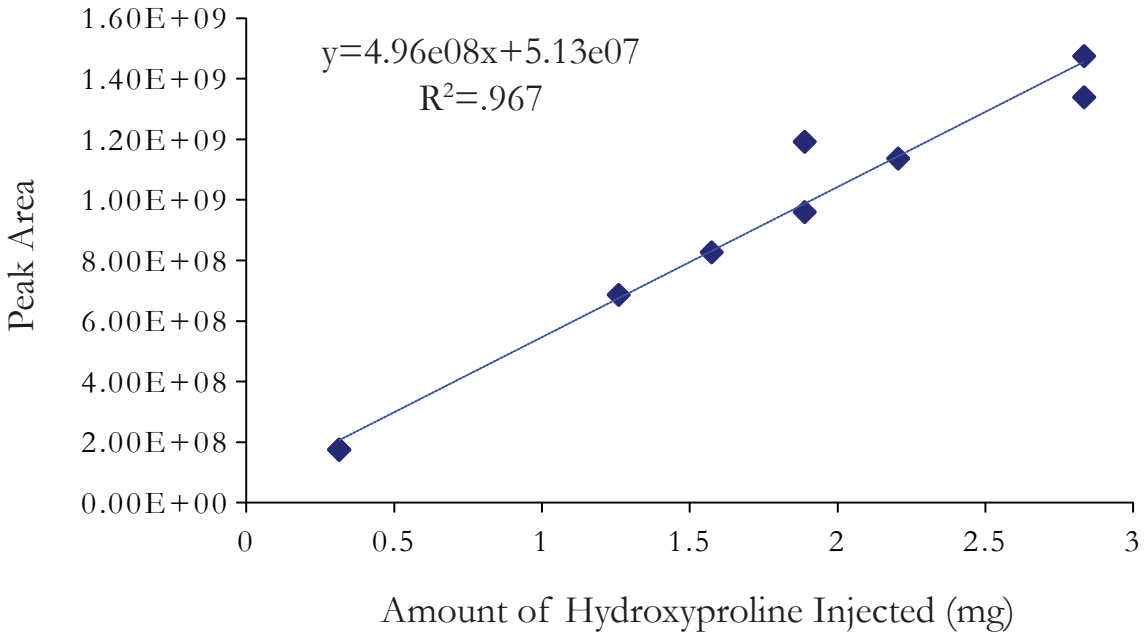

Figure 5.4: An example of a peak area calibration used to quantify yield. Individual points were determined by running a hydroxyproline standard through the HPLC.

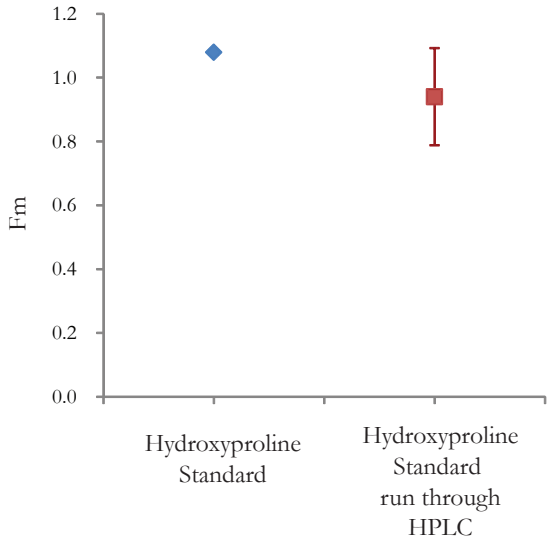

Figure 5.5: Hydroxyproline standard before and after running through HPLC. The hydroxyproline before HPLC was run on a conventional graphite source-AMS. The hydroxyproline after running through the HPLC was run on a gas source-AMS, hence the larger error bars.

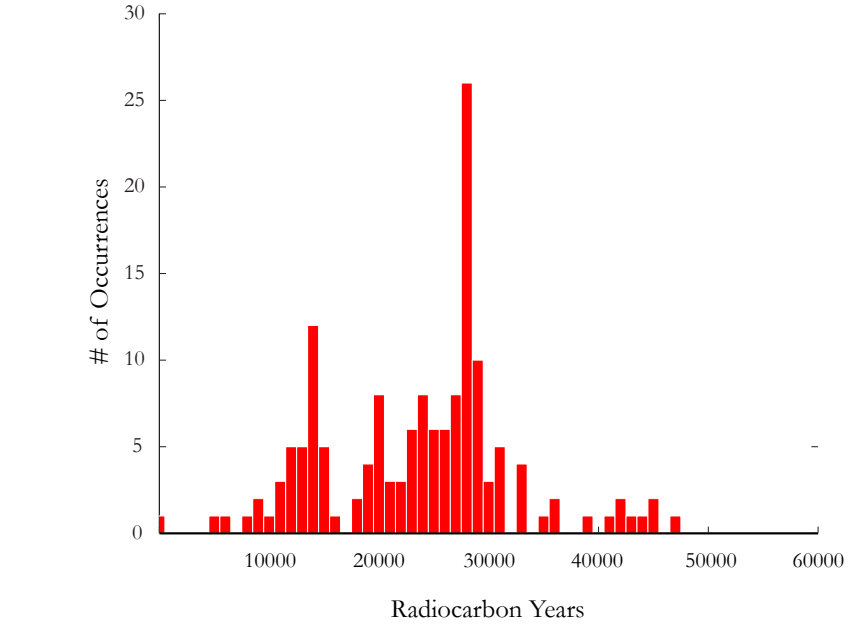

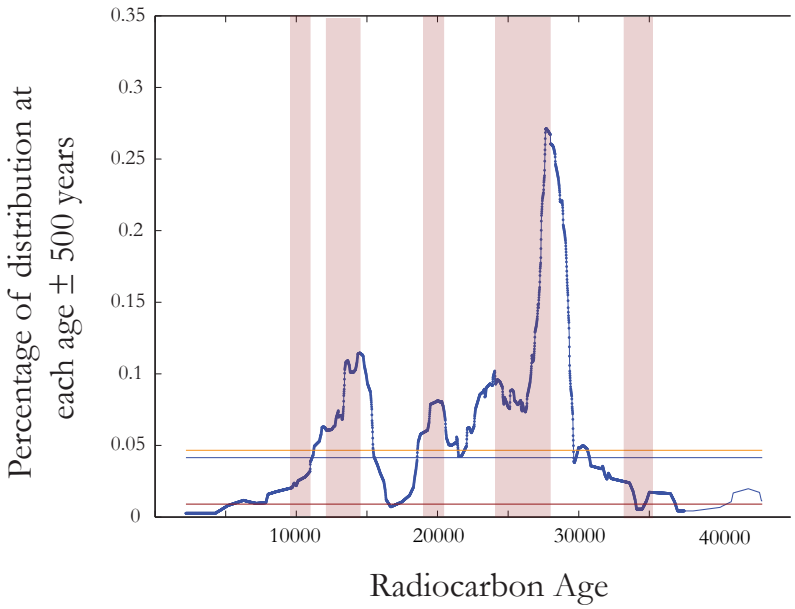

Figure 5.6a: Histogram of all radiocarbon dates made on megafauna from the La Brea Tar Pits.
Figure 5.6b: Percentage of empirical cumulative distribution at each interval +/- 500 years for all distributions studied. The shaded regions are the Younger Dryas and Heinrich Stadial (HS) 1, HS 2, HS 3, and HS 4. Horizontal lines indicate the average percentage of the distribution at Marine Isotope Stage (MIS) 1, MIS 2, and MIS 3, excluding Heinrich Events within those intervals. Note the two graphs are on different axes.

Fossils selected for radiocarbon dating can be assumed to be a random subsample of fossils in the pits as they were not biased by species or to any particular tar pit. Assuming the dates are correct, an interesting pattern unfolds. The abundance of fossils recovered from the La Brea Tar Pits is higher during the Heinrich Events than any other period of time (Figure 5.6).

The Younger Dryas (YD) and the Heinrich (H) Events (17) are seven abrupt climate change events in Earth's history that occurred during the last glacial cycle. H Events are associated with a destabilization of the Laurentide ice sheet during the last glacial period with each of the six events lasting approximately 700−1000 years. The H Events have been characterized in North Atlantic sediment cores, by an increase in abundance of lithic fragments (ice rafted debris), a paucity of polar forminifera and an increase in detrital carbonate (18). The YD occurred between 12650−11700 years BP (19) and is associated with a temporary readvancement of the Laurentide ice sheet after the last deglaciation. The YD and H Events are frequently assumed to have had the same causes and effects and YD is often called H0. However, there is growing evidence that the YD and H Events were expressed differently in various parts of the world.

H Events are difficult to precisely date. They were first identified in the North Atlantic cores as an increase in ice rafted debris (IRD). However, one characteristic of these cores is that during the peak of the IRD event, there are few foraminifera in the core. Therefore it is difficult to make an age model in these cores using radiocarbon dates of foraminifera. H Events are also subtle features of the Greenland ice cores. The Greenland ice cores display a cold interval (Heinrich Stadial) during which the IRD record occurs, and after which an abrupt warming occurs. H Events have been seen in cave records in China (20) as changes in the precipitation patterns and can be absolutely dated using U-Th systematics. However, it is not clear whether the climate signal that causes an increasing in IRD in the North Atlantic causes a change in precipitation in China at the same time. We have chosen to define the Younger Dryas and Heinrich Stadials as the cold period in Greenland during IRD events.

We examined the empirical cumulative distribution (ECD) function made from dates

made from the La Brea Tar Pits using the dates of Heinrich Events and the YD. We then investigated the percentage of the ECD at the Younger Dryas and H1–H4 (Figure 5.6b). We compared these percentages to the average percentages during the Holocene (Marine Isotope Stage (MIS) 1), the deglaciation (excluding YD and H1) and the last glacial period (excluding H2, H3 and H4). From here onwards, the deglaciation is referred to as MIS 2 while the last glacial period is referred to as MIS 3.

In the La Brea distribution, we find that during H1, H2 and H3 there is a higher percentage of animals than any other time in the distribution. There is also a factor of two more animals at H3 than H1, and a factor two more animals in H1 than H2. Interestingly, the YD and H4 show a notable depletion in fossil abundances implying that a different climate mechanism was at play during the YD and H4 than H1 and H3. There is also a depletion in megafauna abundances at the LGM.

This pattern is remarkable because the effect of rapid climate change has only previously been seen in benthic macrofauna, including ostrocods (21), foraminifera (22) deep-sea corals (23) and micromammals (24). Terrestrial megafauna have never before been shown to increase in abundances due to rapid climate change events on the millennial time scale.

It is possible that a climatic variable could be biasing the "trapping efficiency", thereby artificially increasing the abundance of animals during these time periods. One possibility is temperature. However, temperature is unlikely to control the distribution as studies at the Page Museum have indicated that there is not a preferential trapping of animals in the La Brea Tar Pits during environmentally relevant temperature ranges nor is there a change in the area of asphalt pools (personal communication, John Harris).

The most likely explanation for changes in abundances at this site due to H events is changes in moisture. The Southern California climate is Mediterranean-like and therefore moisture limited. The La Brea Tar Pits are located near the LA river, a major source of water to animals in the region. Therefore, an increase in the number of animals in the tar pits implies that there were more animals in the area, and thus that the region was likely wetter.

Interestingly, there is no “peak” in animal abundances in the tar pits during the YD. The YD is frequently referred to in the literature as similar climatically to the Heinrich Events or even as “H0”. However the lack of a peak in animal abundance suggests that perhaps the Southern California climate responded differently during the YD than during Heinrich Events, perhaps suggesting that different mechanisms were at play for transmitting the climate signal from the North Atlantic to the Southwest US during those time periods. The different climatic signatures between the YD and H1 are not only observed in the La Brea Tar Pits. Other paleoclimate records indicate that the regional signature of the American West during Heinrich events was wet (25, 26) while the YD more resembled a La Niña signal (27–29) with a wet Pacific Northwest and a dry Southwest US.

The global signature of the YD and Heinrich Events suggest that large-scale changes in the ocean-atmosphere system are involved in the transference of the abrupt climate change signal from the North Atlantic to the rest of the globe. However the exact mechanisms are not known. In the modern American Southwest, there are two modes of precipitation patterns seen in the Palmer Drought Severity Index (PDSI) and tree ring records from the US (30, 31). One pattern shows a regional drying or wettening in the western US and another pattern shows a bipolar ENSO like signature with drying (or wettening) in the Pacific NW and wettening (or drying) in the SW US (32). The regional wettening which resembles the H1 signature is associated with high latitude forcing while regional pattern of the YD resembles the ENSO pattern and could be associated with a tropical forcing. The potentially different causes of the YD vs. Heinrich Events could explain the regional patterns seen in North America during those time periods as well as the scarcity of megafauna in the La Brea Tar Pits.

This pattern of increased megafauna abundance during Heinrich Events is not only seen in the La Brea Tar Pits, but also in other megafauna distributions around the world as well as in American micromammals and Siberian humans (Figure 5.7, 5.8 and 5.9). We examine the ECD functions of these different distributions and try to correlate the increased animal abundances during Heinrich Events with changes in the climate in the regional climate.

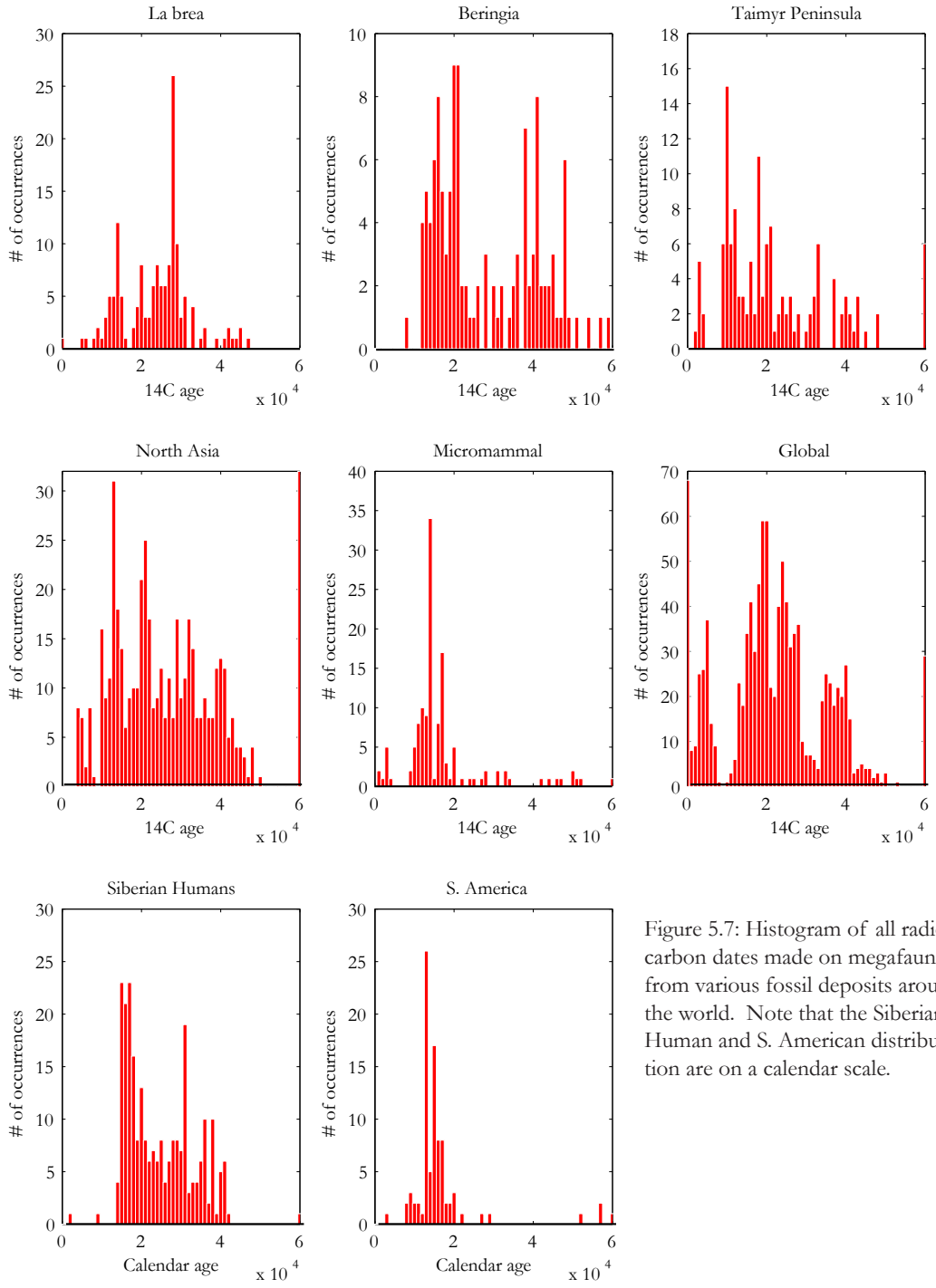

Figure 5.7: Histogram of all radiocarbon dates made on megafauna from various fossil deposits around the world. Note that the Siberian Human and S. American distribution are on a calendar scale.

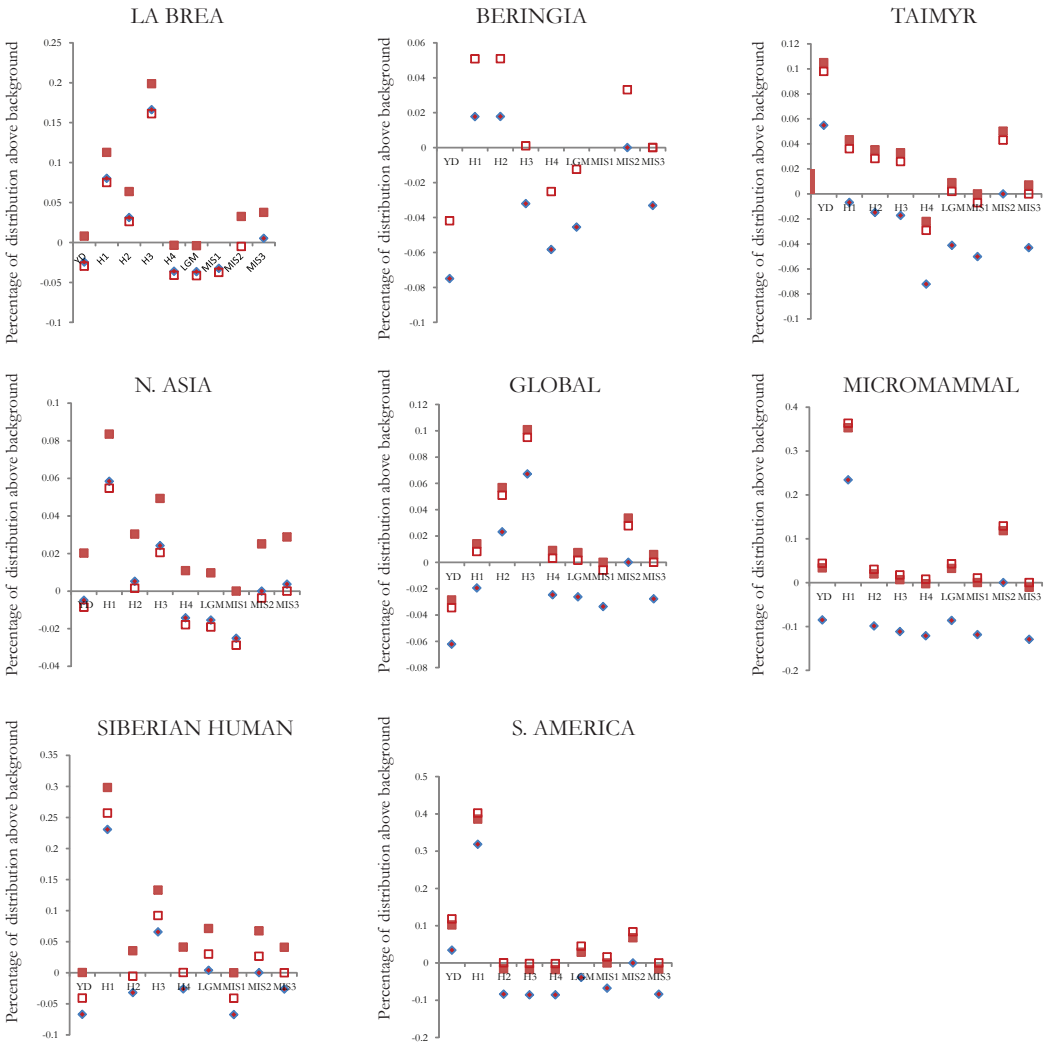

Figure 5.8: The amount of the empirical cumulative distribution (ECD) during each climatic event studied that is above the average amount of ECD during the non YD and Heinrich event times in three background intervals: marine isotope stage (MIS) 1, MIS2, and MIS3.

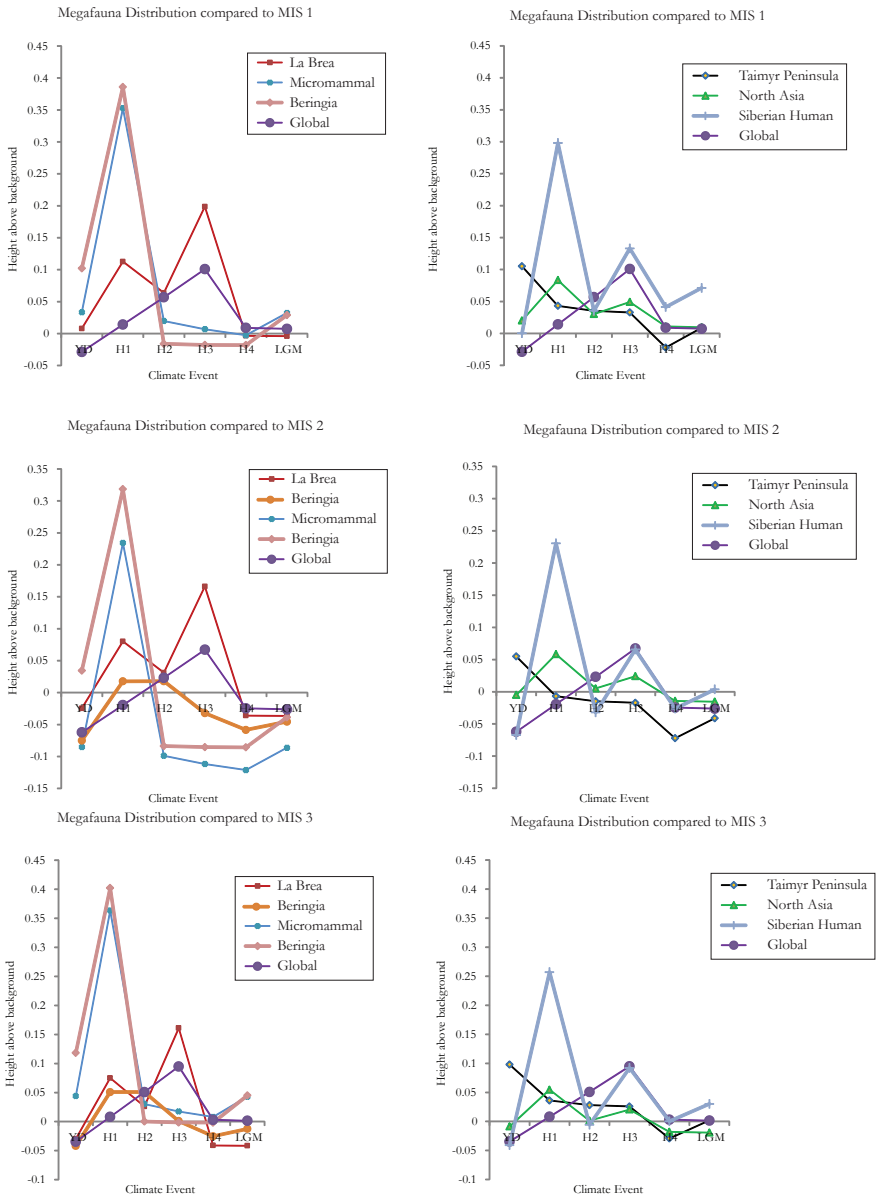

Figure 5.9: The amount of the empirical cumulative distribution function for each climate interval studied about a background. These background periods were marine isotope stage (MIS) 1, MIS 2, and MIS 3, excluding Heinrich Event intervals during these periods.

In Beringia, fossil specimens have been collected from placer mining gravel deposits from around Fairbanks, Alaska. Permafrost fossils are generally exceptional well preserved morphologically and biogeochemically however they do not have stratigraphic context when found in gravel deposits. Therefore, similarly to the La Brea Tar Pit radiocarbon age distribution, ages made from this gravel deposit can be thought to be random and not biased as no particular age is likely to be collected more than another. Fossil specimens used in this study were compiled from compiled from samples curated at the American Museum of Natural History and the Canadian Museum of Natural History. Previous work has been done on measuring these fossil specimens' $\delta^{13}C$ and $\delta^{15}N$ to reconstruct diet (33). The Beringian distribution is different from La Brea because there are no megafauna found during MIS 1. However, similarly to La Brea, the megafauna in Beringia respond to Heinrich Events. There is an increase in abundance of megafauna at H1 and H2 compared to the MIS 2 and MIS 3 and not an increase in abundance at H3 or H4. Similarly to the La Brea there is not an increase at the YD and there is a notable decline during the LGM.

Foraminfera-based sea surface temperature estimates in the NW Pacific show that warm phases parallel Greenland cold stadials and vice versa (34, 35). The antiphasing is hypothesized to stem from variations in global thermohaline circulation. The North Pacific upwelling is greatly affected by the meridional overturning circulation, so any slowdown or shutoff of North Atlantic deep water formation could have led to a turnoff or reduction of the upwelling cold Pacific deep water. A reduction in upwelling at the North Pacific would lead to an immediate short-term warming of the surface water. This antiphasing and reduction in upwelling is also consistent with global circulation model runs and simpler models (36, 37). This warming during Heinrich Events could explain the increase in megafauna abundances in the area. However, this warming is also seen during the YD and H3 and H4 when there are no corresponding increases in animal abundances. So other factors must also influence megafauna abundance in Beringia.

The Siberian arctic is highly sensitive to climate variations and is an important region for understanding climate change. Currently the high Arctic periphery supports only two

species of megafaunal mammals, reindeer and muskox. However several thousand years ago, this same zone supported half a dozen large herbivores. MacPhee et al., (38) has compiled Late Quaternary mammalian megafauna radiocarbon dates from eastern Taimyr Peninsula located in the Siberian arctic. The Taimyr peninsula is intersected by the Byrrangea mountains which form an arc from NE to SW of the peninsula. North of the mountains the landscape is rugged and hilly while southward it merges into the featureless northern Siberian lowland belt. During the last glacial period, the Taimyr Peninsula was largely unglaciated (39). Samples used in MacPhee's compilation were collected from permafrost soils along lake margins and river banks, where fossils are most frequently found. The collecting conditions are considered stochastic as virtually all finds are made at the surface and can be of any age. The frozen ground preserves remains of animals such as wooly mammoth, wooly rhinoceros, steppe bison and reindeers in excellent condition. Sometimes, skin, fur and internal organs are preserved. Dates were made on teeth and long-bone compactum.

The Taimyr Peninsula is anomalous compared to the La Brea and Beringia distribution in that the Younger Dryas has more megafauna than any other time period. However the Taimyr distribution does feel Heinrich Events. There is an increase in animal abundances at H1, H2 and H3 compared to MIS 1 and MIS 3, but not MIS 2. Also, unlike La Brea and Beringia there is a small peak in megafauna relative to MIS 1 and 3 at the LGM.

Several continuous sedimentological records from lakes have been made in the area (40−43). These studies indicate that the Pleistocene climate was generally warmer and wetter than today. Nearby in the Laptev Sea, it has been determined that during Heinrich Events there were a higher abundance of thermophilous xerophyiles, meaning the climate was cool and dry. However, the Younger Dryas corresponds to 3−4^{0}C cooler temperatures and 100 mm lower pollen, although there is an increase in abundance of animals. Similarly to Beringia, there is another unidentified variable controlling megafauna abundances during rapid climate change events.

It has been noted that there is an empirical trend towards younger mean date per latitude

interval as one moves northward in Taimyr (38). This observation implies that species managed to persist longer at higher latitudes than lower ones. One possible explanation is that large influxes of meltwater from glaciers left large parts of the northern Siberian lowlands waterlogged for a long period after end of the glaciation, causing megafauna to retreat northwards to to the northern part of the Peninsula(38). This explanation could also explain the peak in megafauna abundances at the LGM in Taimyr Peninsula. Heinrich Events correspond to colder and more arid events in Central China and Siberia (44). Perhaps megafauna were retreating northward during these events. Sr isotope analysis of these bones could clarify if any megafauna were retreating northward during these climate change events.

The distributions we analyzed for the remainder of the study are not necessarily a random subsample of the true megafauna distribution like the La Brea, Beringia and Taimyr Peninsula distributions. There are several factors that might create biases and distort this record including problems of preservation or visibility of sites, research priorities, and decomposition of organic material meaning less preserved older sites. However these records show similar patterns of increased animal abundances during Heinrich Events or other rapid climate change events.

A comprehensive review of wooly mammoth ages in Northern Russia has been made recently (45). There are two latitudinal bands with the highest concentrations of radiocarbon dates, the Arctic and southern part of Siberia. In both latitude bands there is an increase in mammoth abundances at H1, H2 and H3 compared to MIS 1. Both latitude bands also have an increase in mammoth abundances at H1 and H3 compared to MIS 2 and MIS 3. This distribution is similar to La Brea in that there is a decrease in animal abundances at the YD and H2 compared to H1 and H3, a feature not seen in Beringia or Taimyr Peninsula.

A notable feature in this record that is also seen in the Taimyr Peninsula record is that during the LGM, there is an increase in mammoths abundances in the northern latitudes without an increase in the southern latitudinal band, implying the mammoths were retreating northwards.

Another megafauna record that was analyzed was a global distribution compiled of six megafauna from Eurasia and North America (46). H2 and H3 show a higher abundance of

animals compared to all other time periods. There is a decline in the abundance of megafauna in the Heinrich Event with decreasing age. This feature is not seen in any other record and could reflect a bias in sample collection.

The effect of rapid climate change events on micromammals can also be seen in a micromammal compilation of radiocarbon dates from 21 cave deposits in southeastern North America (24). The micromammal distribution shows an increase in micromammal abundances at H1 compared to all other time periods. However, there is no increase at the YD or any other Heinrich Event that is substantially above background levels. During Heinrich 1 there is a greater abundance of 'cold intolerant' species (Beautiful Armadillo) and cold-adapted (Taiga Vole) and arid-steppe species (Plains Pocket Gopher) implying that there were reduced temperature extremes and the area resembled a boreal parkland or savanna-like environment. The increase in micromammal abundances at H1 shows that climate change during the Heinrich Events affected several trophic levels in the ecosystem.

A compilation of Siberian human paleolithic occupation sites as also been made (47). There is a higher percentage of Siberian humans in the record at H1 and H3 compared to all other time periods. Similarly to the North Asia megafauna population there is a higher abundance of humans at H1 and H3 compared to the YD and H2. Perhaps human hunters were responding to the availability of prey animals during these time periods.

A final location were radiocarbon dates were compiled is South America (48). South America is the only record examined from the Southern Hemisphere and it shows a higher abundance of megafauna at the Antarctic Cold Reversal (ACR) and H1 compared to all other time periods. The Antarctic Cold Reversal is a rapid climate change event that occurred between YD and H1 and is predominantly seen in the southern hemisphere. Records from Africa or Australia will determine whether the ACR signal in megafauna abundances is specific to South America or the Southern Hemisphere as a whole.

5.4 CONCLUSIONS

In conclusion, we have developed a new HPLC method to separate hydroxyproline from

bones. This method will potentially ameliorate the difficult of radiocarbon dating bones. We have also investigated the relationship between rapid climate change events and the abundance of megafauna in several radiocarbon chronologies around the world. We find that there is an increase in megafauna abundances during Heinrich Events compared to most other time periods. Taimyr Peninsula is unusual in that there is an increased abundance at the YD. The Taimyr and N. Asian populations also both show an increase in abundance at the LGM, possibly indicating that the megafauna were retreating northwards. The South American megafauna distribution is the only distribution to show an increase during the ACR, which is a feature of Southern Hemisphere ice and marine records. The Siberian human population showed a similar pattern of relative abundances to the mammoth distribution in North Asia, indicating that humans were responding to the availability of prey. A micromammal distribution from SE US also showed an increase in micromammal abundances at H1, indicating that Heinirch Events favorably affected several trophic levels in the food chain.

Our observations indicate that the relationship of megafauna to climate is much more complex than previously thought. Contrary to the predictions of HLH, MNH, CED and SOI, rapid climate change actually increases the abundance of megafauna. The megafauna extinctions must have been caused by human interaction or a climatic variable that did not affect them during Heinrich Events.

References

1. Barnosky AD, Koch PL, Feranec RS, Wing SL, & Shabel AB (2004) Assessing the Causes of Late Pleistocene Extinctions on the Continents. *Science* 306(5693):70-75.

2. Barnosky AD (1986) "Big game" extinction caused by late Pleistocene climatic change: Irish elk (Megaloceros giganteus) in Ireland. *Quaternary Research* 25(1):128-135.

3. Guthrie RD (1984) Mosaics, allelochemics, and nutrients: an ecological theory of Late Pleistocene megafaunal extinctions. *Quaternary Extinctions: A prehistoric Revolution*, (University of Arizona, Tucson, AZ).

4. Graham RaL, ELJ (1984) Coevolutionary disequilibrium and Pleistocene Extinction. *Quaternary Extinctions: A Prehistoric Revolution*, (University of Arizona Press, Tucson, AZ).

5. Forster MA (2003) Self-organised instability and megafaunal extinctions in Australia. *Oikos* 103(1):235-239.

6. Marcus LaB, R (1984) The significance of Radiocarbon Dates for Rancho La Brea. *Quaternary Extinctions*, ed Martin PaK, R (University of Arizona Press, Tucson, Arizona).

7. Friscia A, van Valkenburgh, B, Spencer, L, Harris, J (2008) Chronology and spatial distribution of large mammal bones in Pit 91. *Palaios* 23:35-52.

8. Richard R Burky DLK, R E Taylor, P E Hare, John R Southon (1998) (super 14) C dating of bone using gamma -carboxyglutamic acid and alpha -carboxyglycine (aminomalonate). *Radiocarbon* 40(1).

9. George D, Southon J, & Taylor RE (2005) Resolving an Anomolous Radiocarbon Determination on Mastodon Bone from Monte Verde, Chile. *American Antiquity* 70(4):766-772.

10. Hedges REM & Millard AR (1995) Bones and Groundwater: Towards the Modelling of Diagenetic Processes. *Journal of Archaeological Science* 22(2):155-164.

11. Stafford Jr TW, Hare PE, Currie L, Jull AJT, & Donahue DJ (1991) Accelerator radiocarbon dating at the molecular level. *Journal of Archaeological Science* 18(1):35-72.

12. Szajdak L. Z-BI (2002) Influence of Mid-Field Afforestation on the Changes of Organic

Nitrogen Compounds in Ground Water and Soil. *Pol. J. Environ. Stud.* 11(1):91-95.

13. Ho TY, Marcus LF, & Berger R (1969) Radiocarbon Dating of Petroleum-Impregnated Bone from Tar Pits at Rancho La Brea, California. *Science* 164(3883):1051-1052.

14. Hess S, van Beek J, & Pannell LK (2002) Acid hydrolysis of silk fibroins and determination of the enrichment of isotopically labeled amino acids using precolumn derivatization and high-performance liquid chromatography–electrospray ionization–mass spectrometry. *Anal Biochem* 311(1):19-26.

15. Komada T, Druffel ERM, & Hwang J (2005) Sedimentary rocks as sources of ancient organic carbon to the ocean: An investigation through Δ14C and δ13C signatures of organic compound classes. *Global Biogeochem. Cycles* 19(2):GB2017.

16. Tripp JA & McCullagh JS (Preparative HPLC Separation of Underivatized Amino Acids for Isotopic Analysis #. *T Amino Acid Analysis,* Methods in Molecular Biology), Vol 828, pp 339-350.

17. Heinrich H (1988) Origin and consequences of cyclic ice rafting in the northeast Atlantic Ocean during the past 130,000 years. *Quaternary Research* 29:142-152.

18. Hemming SR (2004) Heinrich events: Massive late Pleistocene detritus layers of the North Atlantic and their global climate imprint. *Reviews of Geophysics* 42:RG1005, doi:1010.1029/2003RG000128.

19. Steffensen JP*, et al.* (2008) High-Resolution Greenland Ice Core Data Show Abrupt Climate Change Happens in Few Years. *Science* 321(5889):680-684.

20. Wang YJ*, et al.* (2001) A high-resolution absolute-dated late Pleistocene monsson record from Hulu Cave, China. *Science* 294:2345-2348.

21. Cronin TM & Raymo ME (1997) Orbital forcing of deep-sea benthic species diversity. *Nature* 385(6617):624-627.

22. Streeter SS & Shackleton NJ (1979) Paleocirculation of the deep North Atlantic: 150,000-year record of benthic foraminifera and oxygen-18. *Science* 203:168-171.

23. Thiagarajan NG, D. S.; Roberts, M.; McNichol, A. P.; Thresher, R.; Adkins, J. F. (2009)

Radiocarbon Age Variability of Deep Sea Corals from the North Atlantic and the Southern Ocean. in *American Geophysical Union* (San Francisco).

24. Holmes A Semken Jr. RWG, Thomas W. Stafford Jr. (2010

) AMS 14C analysis of Late Pleistocene non-analog faunal components from 21 cave deposits in southeastern North America. *Quaternary International* 217

240-255.

25. Lin JC*, et al.* (1998) A Reassessment of U-Th and14C Ages for Late-Glacial High-Frequency Hydrological Events at Searles Lake, California. *Quaternary Research* 49(1):11-23.

26. Broecker WS*, et al.* (2009) A Great Basin-wide dry episode during the first half of the Mystery Interval? *Quaternary Sci Rev* 28(25–26):2557-2563.

27. Benson L, Burdett J, Lund S, Kashgarian M, & Mensing S (1997) Nearly synchronous climate change in the Northern Hemisphere during the last glacial termination. *Nature* 388(6639):263-265.

28. Vacco DA, Clark PU, Mix AC, Cheng H, & Edwards RL (2005) A speleothem record of Younger Dryas cooling, Klamath Mountains, Oregon, USA. *Quaternary Research* 64(2):249-256.

29. Mathewes RW, Heusser LE, & Patterson RT (1993) Evidence for a Younger Dryas-like cooling event on the British Columbia coast. *Geology* 21:101-104.

30. Cole JE & Cook ER (1998) The changing relationship between ENSO variability and moisture balance in the continental United States. *Geophys Res Lett* 25:4529-4532.

31. Cook ERS, Richard; Cane, Mark A.; Stahle, David W. (2007) North American drought: Reconstructions, causes and consequences. *Earth Science Reviews*

81(1-2):93-134.

32. Karnauskas KB, Ruiz-Barradas A, Nigam S, & Busalacchi AJ (2008) North American Droughts in ERA-40 Global and NCEP North American Regional Reanalyses: A Palmer Drought Severity Index Perspective. *Journal of Climate* 21(10):2102-2123.

33. Fox-Dobbs K, Leonard JA, & Koch PL (2008) Pleistocene megafauna from eastern Beringia: Paleoecological and paleoenvironmental interpretations of stable carbon and nitrogen isotope and radiocarbon records. *Palaeogeography, Palaeoclimatology, Palaeoecology* 261(1–2):30-46.

34. Sarnthein M, Kiefer T, Grootes PM, Elderfield H, & Erlenkeuser H (2006) Warmings in the far northwestern Pacific promoted pre-Clovis immigration to America during Heinrich event 1. *Geology* 34(3):141-144.

35. Kiefer T, Sarnthein M, Erlenkeuser H, Grootes PM, & Roberts AP (2001) North Pacific Response to Millennial-Scale Changes in Ocean Circulation Over the Last 60 kyr. *Paleoceanography* 16(2):179-189.

36. Weijer W & Dijkstra HA (2003) Multiple Oscillatory Modes of the Global Ocean Circulation. *Journal of Physical Oceanography* 33(11):2197-2213.

37. Schmittner A, Saenko OA, & Weaver AJ (2003) Coupling of the hemispheres in observations and simulations of glacial climate change. *Quaternary Sci Rev* 22(5–7):659-671.

38. MacPhee RDE*, et al.* (2002) Radiocarbon Chronologies and Extinction Dynamics of the Late Quaternary Mammalian Megafauna of the Taimyr Peninsula, Russian Federation. *Journal of Archaeological Science* 29(9):1017-1042.

39. Svendsen JI*, et al.* (1999) Maximum extent of the Eurasian ice sheets in the Barents and Kara Sea region during the Weichselian. *Boreas* 28(1):234-242.

40. Andreev AA*, et al.* (2002) Late Pleistocene and Holocene Vegetation and Climate on the Taymyr Lowland, Northern Siberia. *Quaternary Research* 57(1):138-150.

41. Lozhkin A & Anderson P (2006) A reconstruction of the climate and vegetation of northeastern Siberia based on lake sediments. *Paleontological Journal* 40(0):S622-S628.

42. Kienast F, Siegert C, Dereviagin A, & Mai DH (2001) Climatic implications of Late Quaternary plant macrofossil assemblages from the Taymyr Peninsula, Siberia. *Global and Planetary Change* 31(1–4):265-281.

43. Hubberten HW*, et al.* (2004) The periglacial climate and environment in northern Eurasia during the Last Glaciation. *Quaternary Sci Rev* 23(11–13):1333-1357.

44. Porter SC & Zhisheng A (1995) Correlation between climate events in the North Atlantic and China during the last glaciation. *Nature* 375(6529):305-308.

45. Kuzmin YV & Orlova LA (2004) Radiocarbon chronology and environment of woolly mammoth (Mammuthus primigenius Blum.) in northern Asia: results and perspectives. *Earth-Science Reviews* 68(1–2):133-169.

46. Lorenzen ED*, et al.* (2011) Species-specific responses of Late Quaternary megafauna to climate and humans. *Nature* 479(7373):359-364.

47. Fiedel SaK, Yaroslav (2007) Radiocarbon Date Frequency as an Index of Paleolithic Occupation of Siberia: Did Humans React Predictably to Climate Oscillations? *Radiocarbon* 49(2):741-756.

48. Barnosky AD & Lindsey EL (2010) Timing of Quaternary megafaunal extinction in South America in relation to human arrival and climate change. *Quaternary International* 217(1–2):10-29.